GEORG-AUGUST-UNIVERSITÄT
GÖTTINGEN

Fakultät für
Physik

Master's Thesis

Rekonstruktion von $t\bar{t}(Z)$-Ereignissen mit drei Jets mittels eines kinematischen Likelihood-Fits

Reconstruction of $t\bar{t}(Z)$ events with three jets using a kinematic likelihood fit

prepared by

David Grote

from Göttingen

at the II. Institute of Physics

Thesis number:	II.Physik-UniGö-MSc-2017/05
Thesis period:	1st April 2017 until 24th September 2017
First referee:	Prof. Dr. Arnulf Quadt
Second referee:	Prof. Dr. Stan Lai

Abstract

One of the most important properties of the top quark is the third component of its weak isospin, which can only be accessed via direct measurements. The coupling between the Z boson and the top quark, which can be measured in events with top quark pair production and an associated Z boson radiated from one of the top quarks, depends directly on the third component of its weak isospin. In several analyses, kinematic likelihood fits are used to reconstruct the $t\bar{t}Z$ final state, which is essential for the measurement of the coupling. Unfortunately, the production cross section of $t\bar{t}Z$ events is small compared to $t\bar{t}$ production or background events, so that one of the issues of this analysis is a low number of events.

Furthermore, the loss of the light down-type quark's jet in several events lowers the statistics even more, since the jet cannot pass the transverse momentum threshold applied to those events. Since the functions used in the kinematic likelihood fits require at least four jets in an event, this master's thesis introduces a method to modify those functions to reconstruct events with three jets and to increase the statistics of $t\bar{t}Z$ measurements. This method uses an artificial pseudojet based on the average kinematics of the remaining light jet to keep the mass constraints of the unmodified likelihood function. The three jet likelihoods show similar efficiencies in terms of jet-parton matching, but also lower efficiencies, if the artificial jet is used for particle reconstruction.

Zusammenfassung

Eine der wichtigsten Eigenschaften des Top-Quarks ist die dritte Komponente des schwachen Isospins, deren Messung nur auf direktem Weg möglich ist. Die Kopplung des Top-Quarks an das Z-Boson, welche in Ereignissen mit Top-Quark-Paaren und einem von ihnen abgestrahlten Z-Boson gemessen werden kann, hängt direkt von der dritten Komponente des schwachen Isospins ab. Üblicherweise werden die Endzustände der $t\bar{t}Z$-Ereignisse, die essentiell für die Messungen sind, mittels eines kinematischen Likelihood-Fits rekonstruiert. Jedoch ist der Wirkungsquerschnitt der $t\bar{t}Z$ -Ereignisse im Vergleich zu der $t\bar{t}$-Produktion oder anderen Untergrundereignissen sehr klein, was zu einer geringen Anzahl dieser Ereignisse führt.

Des Weiteren wird die Statistik durch das Fehlen des Jets des leichten Down-Type-Quarks in einigen Ereignissen weiter verringert. Dieser fehlt auf Grund der Kopplung zum W-Boson. Der Jet ist in solchen Ereignissen nicht in der Lage, die Transversalimpuls-Schwelle zu überschreiten. Diese Masterarbeit stellt eine Methode vor, um Ereignisse mit drei Jets rekonstruieren zu können. Bei dieser Methode werden die in den Fits verwendeten Likelihood-Funktionen auf entsprechende Weise modifiziert, da sie für gewöhnlich mindestens vier Jets fordern. Ein künstlicher Pseudojet, der auf der durchschnittlichen Kinematik des verbleibenden leichten Jets basiert, ersetzt dabei den fehlenden Jet. Die 3-Jet-Likelihood weist ähnliche Effizienzen bezüglich der Jet-Parton-Zuordnung auf, jedoch schlechtere, wenn der Pseudojet selbst zur Rekonstruktion von Teilchen verwendet wird.

Contents

1 Physical Foundation **3**

1.1 The Standard Model of Particle Physics . . . 3

1.1.1 Quantum Chromodynamics . . . 4

1.1.2 Electroweak Theory . . . 5

1.1.3 Limits of the Standard Model . . . 10

1.2 Top Quark Physics . . . 12

1.2.1 Top Quark Production . . . 13

1.2.2 Top Quark Decay Modes . . . 16

1.2.3 Top Quark Couplings . . . 20

1.3 Top Quark Pair Production with associated Z Boson . . . 21

2 Experimental Setup **25**

2.1 The Large Hadron Collider . . . 25

2.2 The ATLAS Detector . . . 27

2.2.1 The ATLAS TDAQ System . . . 30

2.2.2 Definition of Detector Objects at ATLAS . . . 32

2.2.3 The ATLAS Coordinate System . . . 33

3 Current $t\bar{t}Z$ Measurements **37**

3.1 The Trilepton Analysis . . . 38

3.2 Results of the Cross Section Measurements . . . 39

4 Event Reconstruction **43**

4.1 Definitions of Event Objects . . . 43

4.2 The KLFitter Framework . . . 46

4.2.1 The Operating Principle of KLFitter . . . 46

4.2.2 Particle Reconstruction using KLFitter . . . 48

4.3 Analysis of the KLFitter Performance . . . 52

4.3.1 The Monte-Carlo Samples . . . 53

4.3.2 Determination of the Likelihood Efficiencies . . . 54

5 Reconstruction of $t\bar{t}Z$ Events with three Jets in the trilepton Channel 57
5.1 Analysis of Events with three Jets 57
5.1.1 The Absence of the missing Jet 58
5.1.2 The modified Likelihood Function 59
5.2 The Ghost Jets 61
5.2.1 Ghost Jet Pseudorapidity 61
5.2.2 Ghost Jet transverse Momentum 63
5.2.3 Ghost Jet azimuthal Angle 68
5.3 Performance of the modified Likelihood 70
5.3.1 Comparison between Data and Monte Carlo 71
5.3.2 Separation Power 73
5.3.3 Reconstruction and Matching Efficiencies 75

6 Summary and Outlook 83

Bibliography 85

Introduction

In the 20th century, due to the discovery of a bunch of new particles, physicists had to face a fundamental question: they needed a theory which describes all those particles as well as their interactions. Consequently, a quantum field theory called the Standard Model of particle physics was developed to solve that issue. This theory describes all known elementary particles as well as three fundamental forces. It has been tested in several experiments with magnificent agreement with its experimental measurements and the actual theoretical prediction. Section 1.1 gives an overview over this quantum field theory including the structure of the Standard Model as well as a closer look at two interactions: the Quantum Chromodynamics and the electroweak theory, which are thematised in Section 1.1.1 and Section 1.1.2, respectively. Nevertheless, some experiments also hint at phenomena, which cannot be explained by the Standard Model. One of those phenomena is neutrino oscillation [1], where neutrinos change their flavour over time. This is only possible if neutrinos are massive particles, but the Standard Model assumes them to be massless. This as well as other phenomena are presented in Section 1.1.3.

Several high-energy experiments have operated at different particles accelerators, for instance the *Large Hadron Collider*, which is described more precisely in Section 2.1, the *Tevatron* or the *Large Electron-Positron Collider*. They tested the Standard Model during the past decades and also confirmed many of its predictions. One of those experiments is the ATLAS experiment at the LHC. Section 2.2 gets into more detail about the different detector components and their methods to measure different kinematic quantities of particles as well as its readout system and object definitions.

The discovery of the top quark in 1995 by CDF and DØ at the Tevatron [2, 3] was one big success of high-energy experiments. This particle not only completes the quark sector as the weak isospin partner of the bottom quark, but takes probably a special role within the Standard Model, since its huge mass leads to a strong Yukawa coupling. Due to this special role, different properties of the top quark are presented in Section 1.2.

Another achievement of high energy experiments is the discovery of the Higgs boson in 2012 by ATLAS [4] and CMS [5], which was predicted by the Brout-Englert-Higgs mechanism [6, 7]. This theory was first developed to explain the mass of both the W and

the Z boson in the electroweak theory and describes the mass gaining process of massive particles, which makes this theory an important part of the Standard Model.

Besides the experimental setup, tools to reconstruct final states of particle interactions are essential for advanced measurements. In top quark analyses at the ATLAS experiment, a common tool is the kinematic likelihood fitter (KLFitter) [8]. Its task is the fitting of kinematic parameters, for instance energies and momenta, as well as the right assignment of objects measured by the detector to particles on parton level. The KLFitter as well as its operating principle is described in Section 4.2.

Originally, this framework was developed to reconstruct final states of top quark pair production in the semileptonic decay channel, but it can be modified to reconstruct other final states, for instance top quark pair production with associated Z boson production. These $t\bar{t}Z$ events, which are presented in more detail by Section 1.3, are of great interest, since the coupling of the top quark to the Z boson depends directly on the third component of its weak isospin. A direct measurement of this quantity is the only way to confirm the top quark as the bottom quark's weak isospin partner. An overview over the current $t\bar{t}Z$ analysis is given by Chapter 3.

However, the cross section of the $t\bar{t}Z$ production process is very low compared to $t\bar{t}$ pair production, which leads to a low number of events in analyses. Since the KLFitter framework requires at least four jets in each event to reconstruct the final state, this tool does not give access to events, where some of the jets is missing. This master's thesis presents a possibility to increase the statistics in $t\bar{t}Z$ analyses by taking events with a missing jet into account, which is the topic of Chapter 5. Therefore, a modification of the likelihood function used in the fits is necessary, which allows the KLFitter framework to reconstruct events with three jets. To keep the mass constraints, an artificial pseudo jet, called Ghost Jet, introduced in Section 5.2 replaces the missing jet in the modified likelihood. Its kinematics depends on the correlation between both light quarks. The last chapter gives a summary of the results as well as an outlook of the Ghost Jet's usage.

1 Physical Foundation

The modern foundation of particle physics is the so-called *Standard Model of elementary particles physics*. This theory introduces 12 elementary particles, which form the visible matter in the universe. These so-called *Fermions* are partitioned in two different subgroups: leptons and quarks. The *Bosons* are also included in the Standard Model as force carrier of three of the four fundamental forces: the photon γ, the gluon g as well as the W boson and the Z boson. Gravity is not included yet, which is discussed in Section 1.1.3.

The following section gives a short introduction to two different aspects of the Standard Model. The first one is the strong interaction, which is relevant to high energy physics, since it is the interaction of the dominant production process of top quark pair production at the Large Hadron Collider. The second one is the electroweak interaction, which is the unification of the weak and the electro-magnetic interaction. The Z boson as part of this interaction is one of the main aspects of this thesis.

The last section covers the theoretical parts of top quark physics, which take a special place in the Standard Model, due to its high Yukawa coupling.

1.1 The Standard Model of Particle Physics

The Standard Model of particle physics [9–20] is a quantum field theory with an underlying $SU(3)_C \times SU(2)_L \times U(1)_Y$ gauge symmetry, which describes the known elementary particles as well as three of the four fundamental forces: the strong interaction, the weak interaction and the electromagnetic interaction.

All visible matter in the universe is composed of fermions, which are spin-1/2 particles. They are arranged in three different generations with increasing mass and also separated into quarks and leptons depending on their strong charge.

Unlike leptons, quarks carry strong charge called *colour* and their electric charge is not an integral multiple of the elementary charge e. Possible colour charges are blue, red and green for quarks and accordingly anti-blue, anti-red and anti-green for anti-quarks. Each generation contains an *up-type quark* with electric charge $Q = \frac{2}{3}e$ and weak isospin $I_3 = \frac{1}{2}$ as well as its weak isospin partner a *down-type quark* with electric charge $Q = -\frac{1}{3}e$ and

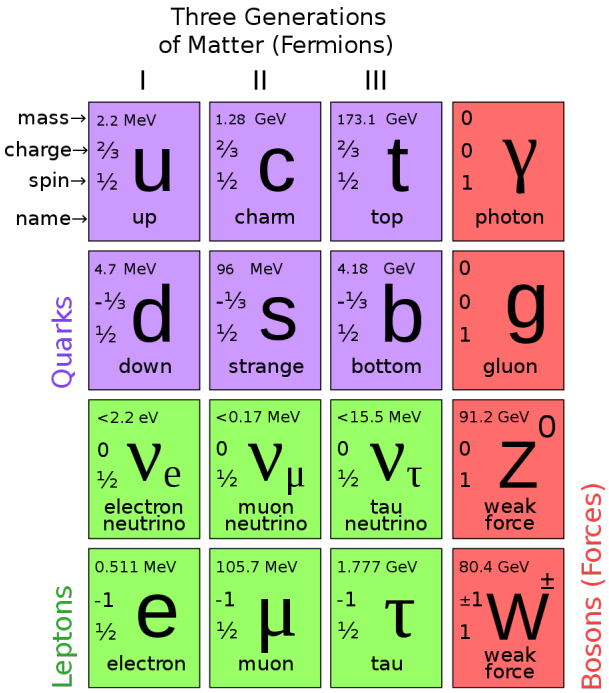

Figure 1.1: The Standard Model of particle physics. It contains 12 different fermions as well as the carrier of three of the four fundamental forces.

weak isospin $I_3 = -\frac{1}{2}$. The quark part of the first generation is made of the *up quark* u and the *down quark* d, the second generation contains the *charm quark* c and the *strange quark* s and the quark part of the third generation is formed by the *top quark* t and the *bottom quark* b.

Each generation also includes two leptons: a neutrino named after its weak isospin partner with electric charge $Q = 0$ and weak isospin $I_3 = \frac{1}{2}$ as well as its weak isospin partner with charge $Q = -1$ and weak isospin $I_3 = -\frac{1}{2}$. The first generation contains the *electron neutrino* ν_e and the *electron* e, the second one the *muon neutrino* ν_μ and the *muon* μ and the third one the *tau neutrino* ν_τ and the *tau* τ.

Each fermion except neutrinos exists in a left-handed state with $I = \frac{1}{2}$ as well as in a right-handed state with $I = 0$ and $I_3 = 0$, which corresponds to a different behaviour related to the weak interaction. Figure 1.1 shows the particles of the Standard Model.

The forces of the Standard Model are explained in the following sections.

1.1.1 Quantum Chromodynamics

Quantum Chromodynamics (QCD) is a non-Abelian quantum field theory based on a $SU(3)$ gauge symmetry group. The eight generators of this group are represented by

eight massless bosons, called *gluons*. The charge of this interaction is called *colour*, which is carried by quarks as well as by gluons. While quarks and anti-quarks only carry one of the three possible colours, named blue, red and green for quarks and anti-blue, anti-red and anti-green for anti-quarks, respectively, the charge of gluons is composed of both, a colour and an anti-colour.

Since the gauge bosons carry the charge of their force itself, the strong interaction shows extraordinary properties compared to *Quantum Electrodynamics* (QED) and *Quantum Flavourdynamics* (QFD) [15, 16, 21]. QED and QFD are described more precisely in Section 1.1.2:

- **Confinement:** Unlike the other fundamental forces, the potential energy between two quarks increases with their distance until their energy reaches a certain threshold to produce a new pair of particles. As a result, quarks are only observed in colourless bound states, called *hadrons*. Depending on their constituents, hadrons are classified as *mesons*, if they are composed of one quark and one anti-quark, or as *baryons*, if their constituents are three quarks. Bound states with five quarks are also verified. For quarks with a high kinetic energy this process recurs many times. As a consequence, quarks are not detected as single particles, but as a whole bunch called *jets*.

- **Asymptotic Freedom:** Due to the strong coupling constant $\alpha_s\left(q^2\right)$, which depends on the energy scale of the interaction q and decreases with higher energy, quarks can be described as asymptotically free particles. The strong interaction coupling is parametrised via

$$\alpha_s\left(q^2\right) = \frac{\alpha_s\left(\mu^2\right)}{1 + \frac{11N_C - 2N_f}{12n} \ln\left(\frac{q^2}{\mu^2}\right)} \tag{1.1}$$

  with a known energy scale μ, N_C the number of colour states and N_f the number of quark flavours at the given energy scale. QCD processes can be calculated using perturbation theory only at high energies.

1.1.2 Electroweak Theory

At a certain energy scale, the electromagnetic and the weak force exhibit huge differences, for instance in terms of properties or couplings, but a unified theory developed

by Glashow [9], Weinberg [10] and Salam [11], the so-called GSW theory based on a $SU(2) \times U(1)$ gauge symmetry group, shows the similarities at high energy.

The quantum field theory, which describes the electromagnetic force, is called Quantum Electrodynamics (QED) with an underlying $U(1)$ gauge symmetry. Its force carrier is the massless spin-0 photon, which arrives after the electroweak unification and couples to all electrically charged particles. It is represented by the vector field A_μ within this theory. Equation 1.2 shows the coupling term of two leptons with spinors $l = l(p)$ interacting via a photon exchange

$$j^\mu_{em} A_\mu = g_e \bar{l} \gamma^\mu l A_\mu, \tag{1.2}$$

where j^μ_{em} is the electromagnetic current, g_e the electromagnetic coupling constant and γ^μ ($\mu = 0, 1, 2, 3$) are the Dirac matrices.

Compared with QED the weak interaction, also called Quantum Flavourdynamics (QFD), is a much more complex theory. It contains three massive particles: three W bosons W_i, $i = 1, 2, 3$, or rather two charged *W bosons* $W^\pm$ and one neutral *Z boson* Z^0 after the electroweak unification. Their interactions are called charged-current interaction and neutral-current interaction, respectively.

The coupling structure of the charged-current interaction shows a vector as well as an axial vector part, where the current takes the form

$$j^-_\mu = g_W \ \overline{e} \ \gamma_\mu \frac{1 - \gamma^5}{2} \nu = g_W \ \overline{e}_L \gamma_\mu \nu_L, \tag{1.3}$$

with g_W the weak coupling constant, ν and e spinors of two isospin partners, γ_μ ($\mu = 0, 1, 2, 3$) the Dirac matrices and $\gamma^5 = i\gamma^0\gamma^1\gamma^2\gamma^3$. For two interacting quarks, an additional factor V_{ij} appears in Equation 1.3, which corresponds to the appropriate entry of the Cabibbo-Kobayashi-Maskawa matrix depending on the involved quarks. Due to the projection operator P_L within the current, the W boson only couples to left-handed particles and right-handed antiparticles. Both chiral projection operators are defined as

$$P_L = \frac{1 - \gamma^5}{2}, \qquad P_R = \frac{1 + \gamma^5}{2} \tag{1.4}$$

and fulfil the following requirements:

$$P_L \cdot P_R = 0 \tag{1.5}$$

$$P_i^2 = P_i \tag{1.6}$$

$$P_L + P_R = 1 \tag{1.7}$$

These properties lead to the orthogonality of the left-handed state $\Psi_L = P_L\Psi$ and the right-handed state $\Psi_R = P_R\Psi$. Depending on their weak isospin the fermions of the Standard Model form isospin doublets $\left(I = \frac{1}{2}\right)$ containing a pair of isospin partners or isospin singlets $(I = 0)$ as follows:

$$\begin{aligned}
Q_L &= \begin{pmatrix} u_L \\ d_L \end{pmatrix} \quad \begin{pmatrix} c_L \\ s_L \end{pmatrix} \quad \begin{pmatrix} t_L \\ b_L \end{pmatrix} \\
u_R &= \quad u_R \qquad c_R \qquad t_R \\
d_R &= \quad d_R \qquad s_R \qquad b_R \\
L_L &= \begin{pmatrix} \nu_{eL} \\ e_L \end{pmatrix} \quad \begin{pmatrix} \nu_{\mu L} \\ \mu_L \end{pmatrix} \quad \begin{pmatrix} \nu_{\tau L} \\ \tau_L \end{pmatrix} \\
\nu_R &= \quad \nu_{eR} \qquad \nu_{\mu R} \qquad \nu_{\tau R} \\
e_R &= \quad e_R \qquad \mu_R \qquad \tau_R
\end{aligned} \tag{1.8}$$

Since right-handed neutrinos are electrically neutral and also massless within the Standard Model, there are no possibilities for other particles to interact with right-handed neutrinos.

Furthermore, the coupling behaviour of the W boson causes violation of the parity symmetry, which was first observed in 1956 by Wu [22]. Additional experimental observations, like the charged Kaon decay, unfold another property of the weak interaction: this interaction couples across the quark families.

In 1963, Cabibbo [23] introduced a rotation in state space assuming that the weak eigenstates do not correspond to the mass eigenstates. At that time, only the three lightest quarks - the up quark, the down quark and the strange quark - were known. As a result, this theory predicted at least one more quark, which was discovered in 1974, the *charm quark c*. Kobayashi and Maskawa [24] extended this model by including a third quark generation to explain the observed CP violation. The quark mixing matrix within the quark sector is called Cabibbo-Kobayashi-Maskawa matrix (CKM matrix) and rotates the three down-type quark states:

$$\begin{pmatrix} d' \\ s' \\ b' \end{pmatrix} = \begin{pmatrix} V_{ud} & V_{us} & V_{ub} \\ V_{cd} & V_{cs} & V_{cb} \\ V_{td} & V_{td} & V_{tb} \end{pmatrix} \begin{pmatrix} d \\ s \\ b \end{pmatrix} \tag{1.9}$$

The following matrix shows the results of the latest measurements of the magnitudes $|V_{ij}|$ (see [25] and included references):

$$V_{CKM} = \begin{pmatrix} 0.97425 \pm 0.00022 & 0.2253 \pm 0.0008 & 0.00413 \pm 0.00049 \\ 0.225 \pm 0.008 & 0.986 \pm 0.016 & 0.0411 \pm 0.0031 \\ 0.0084 \pm 0.0006 & 0.04 \pm 0.0027 & 1.021 \pm 0.032 \end{pmatrix} \tag{1.10}$$

Precise measurements are important to verify the assumption of three generations within the Standard Model. Due to its unitarity, the CKM matrix has to fulfil conditions, which can be represented as triangles within the complex plane, the *unitariy triangles*. Since closed unitary triangles correspond to the fulfilment of the unitarity condition, measurements of their angles and side length are important. The matrix also shows the further the generations of the two interacting quark are apart from each other, the less likely that interaction is.

The second part of the weak interaction has a more complex structure in terms of the vector and axial-vector coupling, which depends on the flavour of the interacting fermions, described by the factors c_V^f and c_A^f within the neutral current

$$j_\mu^0 = \overline{f}\ \gamma_\mu \frac{c_V^f - c_A^f \gamma^5}{2}\ f, \tag{1.11}$$

where f and $\overline{f}$ are the spinors of the interacting fermions, respectively, and γ_μ ($\mu = 0, 1, 2, 3$) the Dirac matrices.

Due to those different behaviours, a unification of the charged and neutral current is not evident, but including the electromagnetic force solves this issue. In this theory, the purely left-handed part ist based on a $SU(2)_L$ gauge symmetry group, while a new charge - the hypercharge Y - has to be introduced in the vector-like part based on the gauge symmetry group $U(1)$, which is defined as

$$Y = 2\,(Q - I_3)\,, \tag{1.12}$$

where Q is the electric charge and I_3 the third component of the weak isospin. The interaction term of this electroweak theory can be written as

$$-ig_W \left(J^i\right)^\mu W_\mu^i - i\frac{g'}{2}\left(J^Y\right)^\mu B_\mu, \tag{1.13}$$

with the three bosonic fields W_μ^i $(i = 1, 2, 3)$ corresponding to the $SU(2)_L$ gauge symmetry group and the bosonic field B_μ corresponding to the $U(1)$ gauge symmetry group. The fields of the two W bosons $W_\mu^\pm$ are linear combinations of two W_μ^i fields

$$W_\mu^\pm = \sqrt{\frac{1}{2}}\left(W_\mu^1 \mp W_\mu^2\right), \tag{1.14}$$

while the fields of the Z boson Z_μ and the photon A_μ are produced by a rotation in state space:

$$\begin{pmatrix} A_\mu \\ Z_\mu \end{pmatrix} = \begin{pmatrix} \cos\left(\theta_W\right) & -\sin\left(\theta_W\right) \\ \sin\left(\theta_W\right) & \cos\left(\theta_W\right) \end{pmatrix} \begin{pmatrix} B_\mu \\ W_\mu^3 \end{pmatrix} \tag{1.15}$$

The angle θ_W is called the *Weinberg angle*. This leads to the following definition of c_V^f and c_A^f introduced in Equation 1.11:

$$\begin{aligned} c_V^f &= I_3^f - 2Q_f \sin^2\left(\theta_W\right) \\ c_A^f &= I_3^f \end{aligned} \tag{1.16}$$

In the same way, there are relations between the coupling strengths and the masses of the W and Z bosons:

$$\begin{aligned} g_W &= \frac{g_e}{\sin\left(\theta_W\right)} \\ M_Z^2 &= \frac{M_W^2}{\cos^2\left(\theta_W\right)} \end{aligned} \tag{1.17}$$

with $M_Z = (91.1876 \pm 0.0021)\,\text{GeV}$ and $M_W = (80.385 \pm 0.015)\,\text{GeV}$ [25].

Since a mass term of a gauge boson within the Lagrangian would violate the gauge symmetry of the theory, such a term cannot be introduced directly into the Lagrangian.

The solution of this problem is given by Robert Brout, Francois Englert and Peter Higgs in the 1960s. The so-called Brout-Englert-Higgs mechanism [6, 7] introduces a new scalar field, which is called the Higgs field. It applies spontaneous symmetry breaking to create new coupling terms between the already existing particles and the Higgs field. This also leads to mass terms of the gauge bosons depending on the *Yukawa coupling* of this theory.

Although this mechanism is necessary to complete the Standard Model, this thesis does not go into further detail.

1.1.3 Limits of the Standard Model

Despite the magnificent success of the Standard Model, there are still phenomena, which are not described by the current state of this theory. This section gives a short overview of the most common ones [1, 26–29].

Spontaneous Symmetry Breaking

As mentioned in Section 1.1.2 the mass gaining process of the three massive gauge bosons of the electroweak interaction is caused by the spontaneous symmetry breaking within the Brout-Englert-Higgs mechanism, but the Standard Model is not able to explain this symmetry breaking.

Neutrinos

The Standard Model of particle physics assumes massless neutrinos, which only interact via the weak interaction as left-handed particles or right-handed antiparticles. Recent neutrino experiments, e.g. neutrino oscillation, give evidence that neutrinos are in fact massive particles. Massive neutrinos lead to the question, whether these particles are Dirac or Majorana particles, which is identical to the question, whether neutrinos are their own antiparticles or not. As Dirac particles, neutrinos and antineutrinos would be different particles, while the neutrino would be its own antiparticle as a Majorana particle. Due to the observation of neutrino oscillation, the lepton sector needs also a mixing mechanism similar to the CKM matrix in the quark sector, where neutrino weak eigenstates are composed of mass eigenstates.

Dark Matter

Astronomical observations lead to the conclusion of the existence of stable matter, which primarily interacts via gravity. The particles of that matter do not couple to photons, which makes it very hard to detect them. The Standard Model does not provide candidates

for such neutral massive particles and they can only be found in extensions of this theory, for instance in supersymmetry as supersymmetric partners of the light Standard Model particles.

Gravity

Three fundamental forces are described as quantum field theories within the Standard Model: the electromagnetic, the strong as well as the weak force. Gravity more specifically general relativity is not included, since there is no known way to formulate a quantum field theory of gravity.

The Grand Unification

The Grand Unification is an idea of a theory, which describes all particles in the universe as well as their interactions. From an aesthetic point of view a unification of the gauge couplings is expected at high energy, but the Standard Model does not contain this feature. It is only covered by its extensions.

1.2 Top Quark Physics

As the heaviest particle within the Standard Model of particle physics, the role of the top quark is very important not only with regard to the Standard Model but also beyond it.

In the 1960s, Cronin et al. [30] discovered CP violation within neutral Kaon decays, which was evidenced by measuring K_S^0 decays in a region, where only K_L^0 decays were expected. In 1973, this discovery motivated Kobayashi and Maskawa to expand the quark-mixing model [24] by a third generation of quarks to explain this phenomenon. This third generation contains a new down-type quark as well as a new up-type quark, nowadays known as the *bottom quark* and the *top quark*. In the following years, discoveries of new particles supported the assumption of a third generation of particles.

In the same year of the quark-mixing model's expansion, the tau lepton was discovered at SLAC [31], which established a third generation within the lepton sector of the Standard Model. A few years later, in 1977, the discovery of the postulated third down-type quark, the bottom quark, at Fermilab [32] verified the assumption of a third quark generation. This led to the next task: the confirmation of the existence of the bottom quark's weak isospin partner - the top quark. The existence of the top quark was supported by the following two arguments:

First, in 1970, Glashow, Iliopulos and Maiani developed a theory called the GIM mechanism [10] to explain the naturally suppressed flavour-changing neutral currents (FCNC) and the different behaviour of processes involving particles with strangeness, which was introduced by Gell-Mann and Nishijima [33, 34] to explain the slow decay of particles including strange quarks. The up-type quark of the second generation, the *charm quark*, was originally postulated by this theory, but it is also possible to extent the theory to three generations. After the discovery of the bottom quark, several theories tried to describe the new physical situation without a top quark and treat the bottom quark as a SU(2) singlet [35–37]. A bottom quark singlet in such a theory would spoil the natural suppression of flavour-changing neutral currents, which would lead to observations of FCNC in the bottom quark's decays. Measurements of limits regarding the FCNC exclude the assumption of a bottom quark as a $SU(2)$ singlet [38].

The renormalization of the electroweak theory gives the second reason for the existence of the top quark as the up-type quark of the third generation. To include the electroweak theory into the context of the Standard Model, an essential precondition is to avoid anomalies within this theory. Assuming that quarks only exist in three different colour states, which is confirmed by measurements, this avoidance is only available, if the number of quarks is equal to the number of leptons. The discovery of the tau lepton in combination with the confirmation of the existence of the third generation neutrino

via precise measurements of the Z^0 resonance at LEP [39] and the necessity of renormalization leads to a strong indication of the existence of the bottom quark's weak isospin partner.

In 1995, the top quark was discovered by CDF and DØ at the TEVATRON [2, 3]. After the shutdown of the TEVATRON, the Large Hadron Collider at CERN is the only collider, which is able to produce top quarks.

The top quark owes its special role within the Standard Model to its huge mass compared to the other particles of the Standard Model. The top quark mass was measured by the CDF collaboration and the DØ collaboration at the TEVATRON as well as by the ATLAS collaboration and the CMS collaboration at LHC. A combination of the measurements yields a top quark mass [40] of

$$m_t = 174.30 \pm 0.35(stat) \pm 0.54(syst) \text{ GeV}, \tag{1.18}$$

which corresponds to a Yukawa-coupling close to 1. As a result, the top quark mass appears in many electroweak calculations, so that a precise measurement of the mass is of great interest. The high mass of the top quark also leads to a very short lifetime τ_t, which can be calculated via the decay width of the top quark's relativistic Breit-Wigner mass distribution $\Gamma_t = \hbar/\tau_t$. Jeżabek and Kühn [41] calculated the decay width of the top quark at next-to leading order with the following result:

$$\Gamma_t \overset{(@\text{NLO})}{=} \frac{G_F m_t^3}{8\pi\sqrt{2}} \left(1 - \frac{M_W^2}{m_t^2}\right) \left(1 + 2\frac{M_W^2}{m_t^2}\right) \left[1 - \frac{2\alpha_2}{3\pi} \left(\frac{2\pi^2}{3} - \frac{5}{2}\right)\right] = 1.3 \text{ GeV} \tag{1.19}$$

This decay width corresponds to a very short lifetime of $\tau_t = 5 \cdot 10^{-25}$ s, which is two orders of magnitude smaller than the hadronization time scale. Since the top quark decays before it can form bound states, it transfers its properties to its decay products. The detection of those decay products allows a direct measurement of the top quarks properties, which is a unique behaviour within the Standard Model.

1.2.1 Top Quark Production

Since gravity is negligible on particle level and the only collider, which is able to produce top quarks is the LHC at CERN, a pp collider, top quarks can only be produced via the strong interaction or the weak interaction. The production via the strong interaction is the dominant process at the LHC and produces pairs of top quarks (*pair production*),

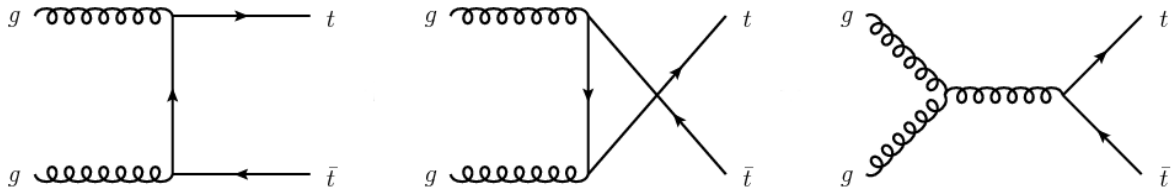

Figure 1.2: Leading-order Feynman diagrams for $t\bar{t}$ production at the LHC. Gluon-gluon fusion is the dominant part.

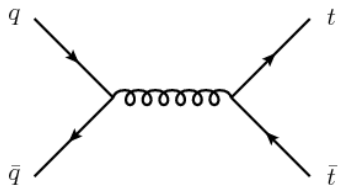

Figure 1.3: Leading-order Feynman diagram for $t\bar{t}$ production at the TEVATRON. $q\bar{q}$ annihilation is the dominant part.

while the production via the weak interaction only produces single top quarks, since the top quark pair production via the weak interaction is very unlikely.

Pair Production of Top Quarks

Since its discovery in 1995, the top quark has only been produced at hadron colliders, where the hard scattering process between the particles of each beam leads to a top quark production dominated by pair production. The leading order Feynman diagram of the dominant top quark production process at the LHC, gluon-gluon-fusion, is shown in Figure 1.2, while Figure 1.3 shows the leading order Feynman diagram of the dominant top quark production process at the TEVATRON, *quark-antiquark annihilation*. At the energy scale of both hadron colliders the interaction of the beam particles does not happen between the particles themselves, $p\bar{p}$ at the TEVATRON and pp at the LHC, but between their constituents, so-called partons , which can be either valence quarks, sea quarks or gluons. Since only the beam energy can be set, the energy of the partons, which participate in the interaction of the collision, has to be described via probability functions, the *parton distribution functions* (PDF), which give the probability to observe a parton with a certain momentum fraction. The momentum fraction carried by each parton, x, is also called the *Bjorken x*. To visualize the different parton distribution functions, Figure 1.4 shows the PDFs of different partons at the factorisation scale $\mu_f^2 = 30000\ \text{GeV}^2 \approx m_t^2$.

The PDFs also explain the different dominant production processes of top quark pair at the TEVATRON and the LHC. The effective squared centre-of-mass energy defined by

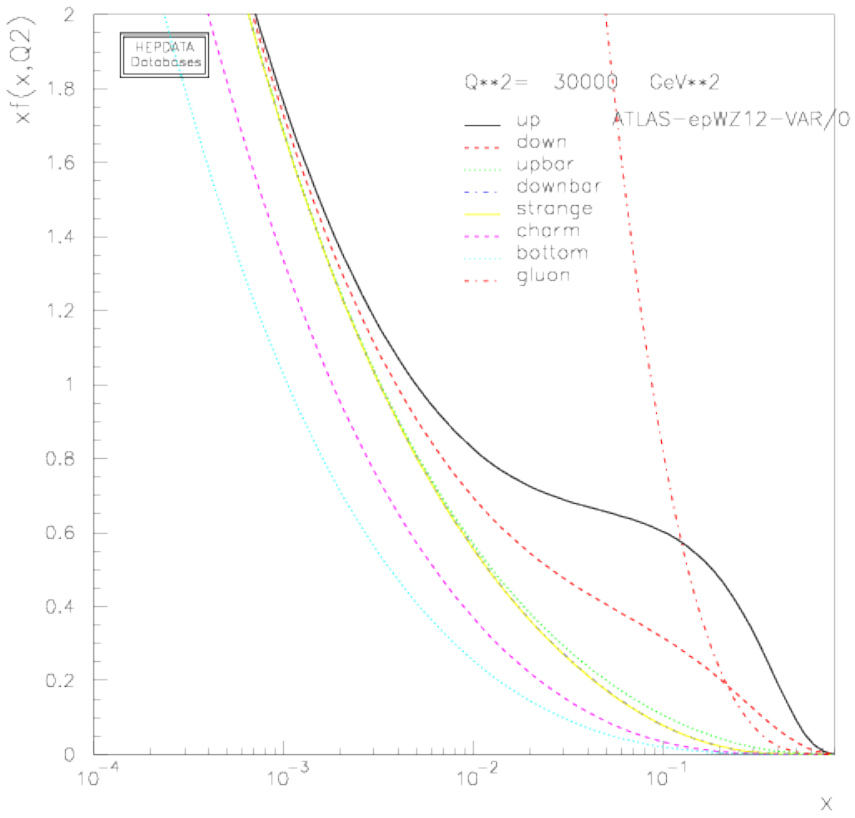

Figure 1.4: Parton density functions of the proton's constituents at the factorisation scale $\mu_f^2 = 30000\ \text{GeV}^2 \approx m_t^2$ using the ATLAS group ATLAS-epWZ12-VAR set. Created with [42].

$\hat{s} = x_i x_j s$ with the Bjorken momenta of the interacting partons x_i, x_j and the centre-of-mass energy on hadron level $\sqrt{s}$ has to fulfil the condition $\hat{s} \geq 4m_t^2$ to produce $t\bar{t}$ pairs. The TEVATRON collided protons and antiprotons at a centre-of-mass energy of $\sqrt{s} = 1.96\text{GeV}$ (Run II). Due to the mentioned condition and assuming a symmetric collision, each parton had to carry a momentum fraction of at least $x \sim 0.2$, which made the $q\bar{q}$ annihilation the dominant process with 85%.

The LHC reaches much higher centre-of-mass energies ($\sqrt{s} = 13 - 14$ TeV), so that the partons need to carry a much smaller momentum fraction to produce $t\bar{t}$ pairs. For momentum fractions below $x \sim 0.1$, the involved partons are most likely gluons. Therefore, the top quark pair production at the LHC is dominated by gluon-gluon fusion with about 90%.

To calculate the inclusive cross section of different particle production processes at hadron colliders, for instance the top quark pair production, all combinations of partons

have to be taken into account. Considering this fact, the *factorization theorem* [43] provides a formula for the cross section using the PDFs $f_i\left(x_i, \mu_f^2\right)$ and the individual partonic cross sections $\hat{\sigma}_{ij\to t\bar{t}}$:

$$\sigma_{t\bar{t}}\left(\sqrt{s}, m_t\right) = \sum_{i,j=q,\bar{q},g} \int dx_i dx_j f_i\left(x_i, \mu_f^2\right) f_j\left(x_j, \mu_f^2\right) \times \hat{\sigma}_{ij\to t\bar{t}}\left(\hat{s}, x_i, x_j, m_t, \mu_f, \alpha\left(\mu_f^2\right)\right) \tag{1.20}$$

Figure 1.5 shows the comparison of $t\bar{t}$ cross section measurements of the ATLAS collaboration at a centre-of-mass energy $\sqrt{s} = 7, 8$ and 13 TeV to the NNLO+NNLL theoretical predictions.

The result of the $t\bar{t}$ cross section measurement by the ATLAS collaboration [44] with an integrated luminosity of 3.2 fb^{-1} and a centre-of-mass energy $\sqrt{s} = 13$ TeV is

$$\sigma_{t\bar{t}} = 818 \pm 8(\text{stat}) \pm 27(\text{syst}) \pm 19(\text{lumi}) \pm 12(\text{beam}) \text{ pb}, \tag{1.21}$$

which is in agreement with the theoretical predictions.

Single Top Quark Production

Figure 1.6 shows the three different possibilities of single quark production at leading order. The first one is the *s-channel mode*, where a quark and an antiquark annihilate each other. The resulting virtual W boson decays further into a top quark and a b quark. The second mode is called *t-channel*. In this channel the top quark is produced via the exchange of a W boson. The last possibility is the *associated W production*. The final state of this production contains a single top quark as well as a W boson.

The production of single top quark can be used for precise measurements of top quark couplings, but it is hard to observe those events due to the large background of this production mode.

1.2.2 Top Quark Decay Modes

Due to its very short lifetime, the top quark decays immediately via the weak interaction. The final state contains a W boson and a down-type quark, which is mostly a b quark, since the decay into another down-type quark is strongly suppressed by much smaller CKM matrix elements. The decay of a single top quark is shown in Figure 1.7 .

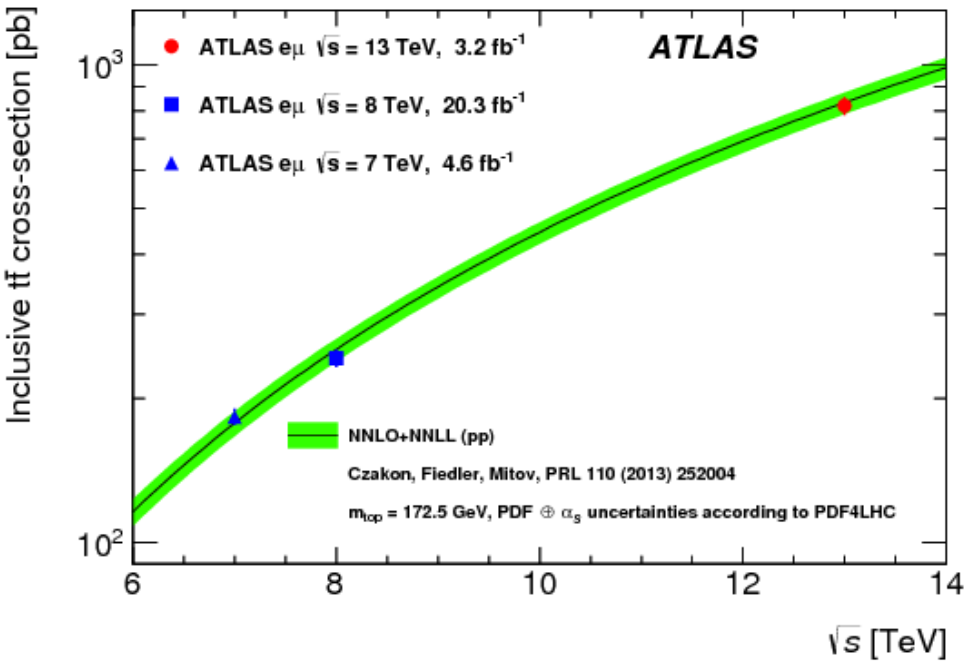

Figure 1.5: Cross-section for $t\bar{t}$ pair production in pp collisions as a function of centre-of-mass energy. ATLAS results in the dilepton $e\mu$ channel at $\sqrt{s} = 13,8$ TeV and 7 TeV are compared to the NNLO+NNLL theoretical predictions [44].

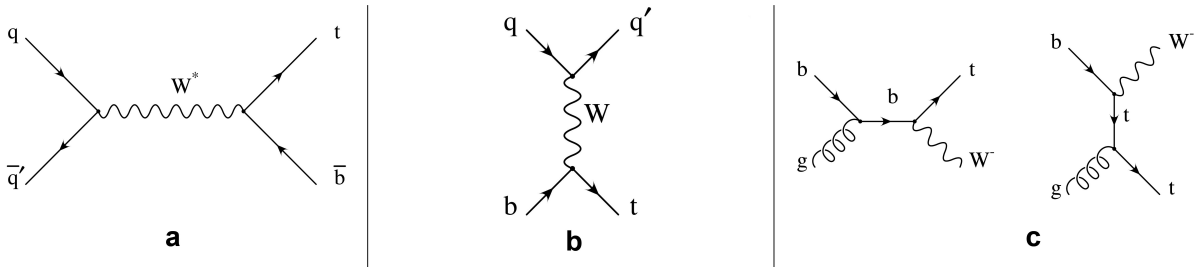

Figure 1.6: Leading-order Feynman diagrams for single top quark production via a) an s-channel production, b) a t-channel production or c) an associated W production.

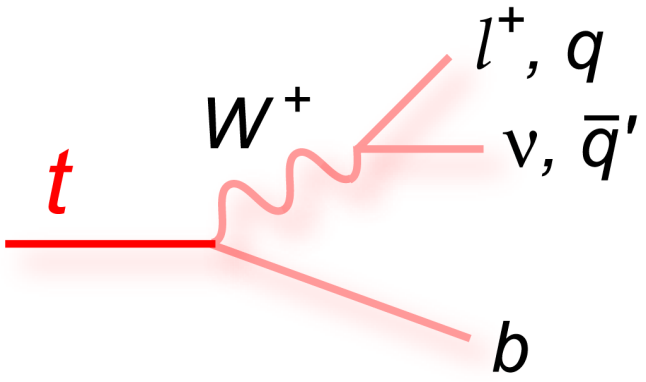

Figure 1.7: The decay mode of a single top quark. Depending on the decay of the W boson, the top quark can decay either leptonically via $t \to bl\nu_l$ or hadronically via $t \to bq\bar{q}'$

The W boson can further decay leptonically to a lepton and its corresponding neutrino $W \to l\nu_l$ or hadronically to a pair of quarks $q\bar{q}'$, which will form jets. The decay of the W boson defines the signature of the top quark decay.

Figure 1.8 shows the decay modes of a $t\bar{t}$ pair as well as the estimations of their branching fractions, which are in agreement with measurements [25]. The cross-family coupling of the W boson is assumed to be negligible. This leads to two remaining possibilities of quark families in the hadronic W boson decay. Due to energy and momentum conservation, the third quark generation is excluded, since the mass of the top quark is too high to be produced in this decay. Including the different colour states, which leads to six possible quark decays, the ratio of hadronic and leptonic decays, which contain three different leptonic final states for the W boson, is 2:1.

The three different signatures of $t\bar{t}$ pair decays contain all combinations of two single top quark decays: the *allhadronic* decay channel containing only jets in the final state, the *dileptonic* decay channel with leptons and b-jets as a final state and the *semileptonic* decay channel, which is a mixture of both.

Allhadronic

Since about 46% of all $t\bar{t}$ pairs decay allhadronically ($t\bar{t} \to bbq_1q_2q_3q_4$), this is the channel with the highest branching fraction. Its signature, which contains two b-jets and four light jets, leads to a huge background within the allhadronic channel caused by e.g. QCD multijet events. Due to this huge background, a distinction between signal and background is very hard.

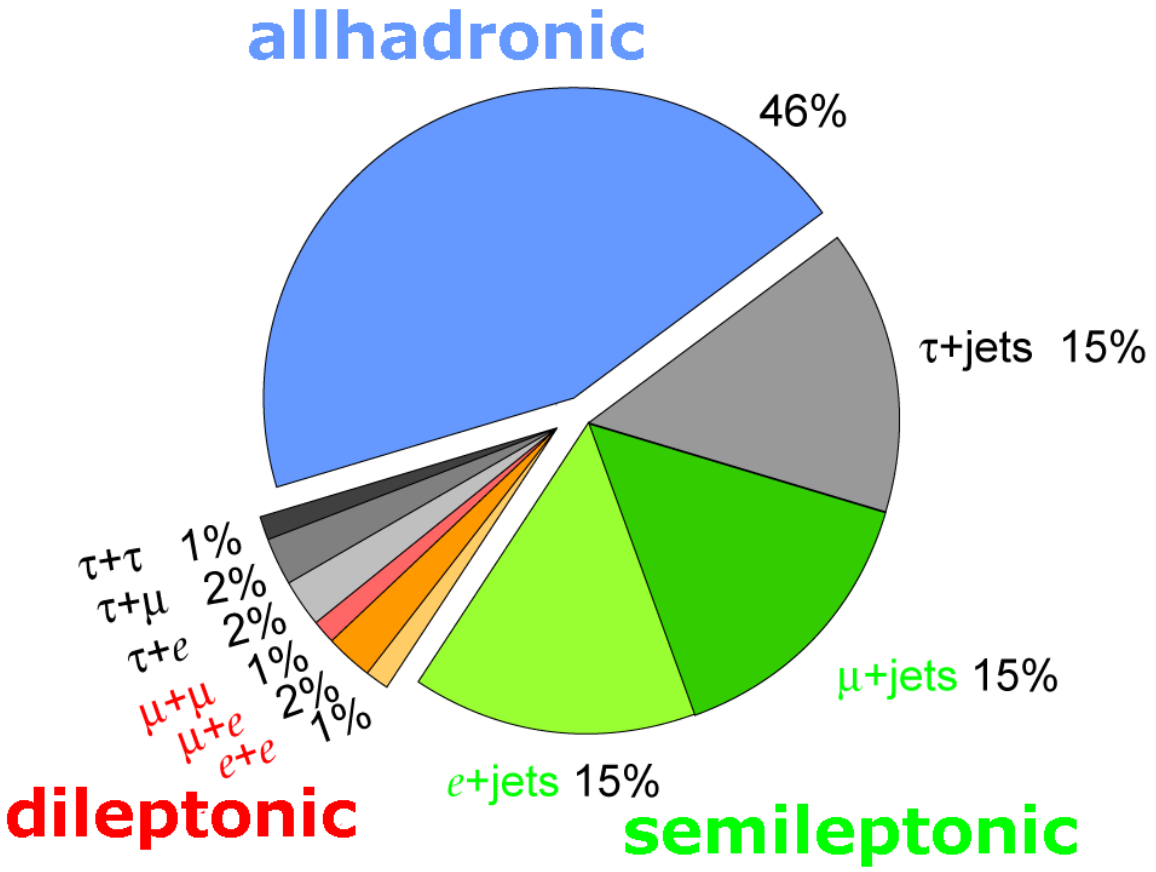

Figure 1.8: The different decay modes of a $t\bar{t}$ pair as well as the estimation of the corresponding decay rates. The modes can be partitioned in three different groups depending on the W boson's final states: allhadronic, dileptonic and semileptonic.

Dileptonic

About 4% of the $t\bar{t}$ pairs decay dileptonically ($t\bar{t} \rightarrow bbl_1\nu_{l_1}l_2\nu_{l_2}$). The leptons are either electrons or muons. Tau leptons are not observed directly and decay further into lighter particles, which can be light leptons or light quarks. The signature of this decay channel is very distinct. This leads to a low number of background events, but the dileptonic final state of a $t\bar{t}$ pair decay contains two neutrinos, which are detected as missing transverse energy applying momentum conservation. This leads to difficulties of the kinematic reconstruction of the events.

Semileptonic

The semileptonic final state of a $t\bar{t}$ pair decay contains two b-jets, two light jets as well as a lepton and its corresponding neutrino ($t\bar{t} \rightarrow bbq_1q_2l\nu_l$). In the case of a hadronically decaying tau lepton, this channel has to be distinguished from the allhadronic channel. The fraction of $t\bar{t}$ pairs decaying semileptonically (45%) is comparable to the allhadronic channel. With regard to separation power and statistics, the semileptonic channel combines the advantages of both the allhadronic and the dileptonic channel. Due to one leptonically decaying top quark, this channel has a good separation power and also good statistics compared to the other channels. The semileptonic decay channel was often called the "golden channel" and was also preferred in many different analyses.

1.2.3 Top Quark Couplings

Since the massive top quark carries electrical as well as colour charge and also acts as the bottom quark's weak isospin partner, it is influenced by all fundamental forces. Precise measurements of the top quark's couplings and properties are important to verify the prediction of the Standard Model or to discover physics beyond the SM.

Due to its huge mass, the top quark's Yukawa coupling, which describes the coupling to the Higgs boson, is close to unity. This is important with regard to the Higgs boson production at the LHC, where gluon-gluon-fusion is the dominant production process. Since the Higgs boson does not couple to the massless gluons, it can only be produced via a loop of heavy particles, which are mostly top quarks. The production rate of Higgs bosons depends directly on the tH coupling, so that this coupling can be measured directly by observing tH and $t\bar{t}H$ final sates.

Furthermore, the precise measurement of the Yukawa coupling of the top quark can help to investigate physics beyond the Standard Model. Several new theories predict a number of heavy particles, for instance in theories with an expanded Higgs sector. Since the energies of modern particle accelerators are too low to produce those new heavy particle, they would contribute to loops of the Higgs boson production. This would change the production rate compared with the Standard Model predictions and would indicate the presence of new physics.

Another important property of the top quark, which can be used not only to verify the Standard Model but also to search for new physics, is its behaviour relating to the weak interaction. On the one hand the measurement of the top quark's weak coupling is a measurement of the third component of its weak isospin, which is predicted to be $+1/2$ by the Standard Model. On the other hand the measurement of the tWb coupling

including the CKM matrix element V_{tb}, which is assumed to be $|V_{tb}| \approx 1$, can indicate the existence of a fourth generation of elementary particles. Due to the unitarity of the CKM matrix, the existence of a fourth generation would cause a smaller matrix element than predicted by the Standard Model.

There are two different possibilities to analyse the tWb vertex structure. The CKM-matrix element $|V_{tb}|$, which contains the coupling, can be extracted from the ratio of the two processes $t \to Wb$ and $t \to Wq$. Furthermore, the angular distribution of the W boson's decay products is directly influenced by the top quark's spin. Since the top quark decays before hadronization, it transfers the spin information to its decay production and further measurements of the three different polarisation states of the W boson (longitudinal, left-handed and right-handed) gives some indications of the verification of the Standard Model.

The coupling of the top quark to a photon is measured in top quark pair production with an associated photon $t\bar{t}\gamma$, which can be identified via an additional cluster in the electromagnetic calorimeter. Since a photon can be emitted by any electrically charged particle, this fact has to be taken into account when $t\bar{t}$ final states with an associated photon are analysed.

A further option to measure the weak isospin of the top quark is by measuring the tZ coupling. The only access to this coupling is given by associated Z boson production, where a top radiates a Z boson in the final state. Quark-antiquark-annihilation with a subsequent virtual Z boson decay to a pair of top quarks is highly suppressed at high energy hadron collider.

1.3 Top Quark Pair Production with associated Z Boson

The $t\bar{t}Z$ Production

Events providing direct access to the tZ coupling are top quark pair production with associated Z bosons, whose Feynman diagrams are shown in Figure 1.9 at leading order. The Z boson can be radiated either as *initial state radiation* (ISR) from initial quarks or as final state radiation from top quarks. Since the ISR case does not contain any information about the tZ coupling and is also suppressed by gluon-gluon-fusion, only events with Z bosons radiated in the final state are of interest.

The MADGRAPH5_aMC collaboration calculated the cross section of top quark pair production with associated Z boson at next-to-leading at 13 TeV with the following

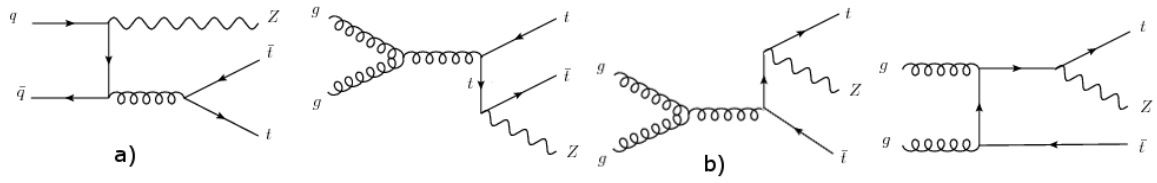

Figure 1.9: Feynman diagrams of $t\bar{t}Z$ final state production. This final state can be produced by either a) initial state radiation or b) final state ration.

result [45]:

$$\sigma_{t\bar{t}Z} = 0.76^{+9.7\%}_{-11.1\%}(\text{scale})^{+1.9\%}_{-2.2\%}(\text{PDF})\ \text{pb} \tag{1.22}$$

Compared to Equation 1.21, the cross section with associated Z boson is about three orders of magnitude smaller than the cross section without Z boson radiation. Cross section measurements of the top quark pair production with associated Z boson at 13 TeV by the ATLAS and CMS collaborations at the LHC yields the following results [46, 47]:

$$\sigma^{\text{ATLAS}}_{t\bar{t}Z} = 0.92 \pm 0.29(\text{stat.}) \pm 0.10(\text{syst.})\ \text{pb} \tag{1.23}$$

$$\sigma^{\text{CMS}}_{t\bar{t}Z} = 0.70^{+0.16}_{-0.15}(\text{stat.})^{+0.34}_{-0.32}(\text{syst.})\ \text{pb} \tag{1.24}$$

These measurements as well as the measurements at 7 TeV and 8 TeV [48–51] are in agreement with the theoretical prediction in Equation 1.22.

The $t\bar{t}Z$ Decay

The signature of the t$\bar{\text{t}}$Z final state is the same as for the pure top quark pair decay, but with additional particles originating from the associated Z boson of the event. The Z boson can decay either hadronically into a pair of quark $Z \to q\bar{q}$ or leptonically into a lepton-antilepton pair $Z \to l\bar{l}$. In the second case there is a distinction between invisible decays, where the Z boson decays into two neutrinos $Z \to \nu\bar{\nu}$, and visible decay, where $l = e, \mu, \tau$. Figure 1.10 shows the different decay mode of the Z boson.

Since the semileptonic decay of the top quark pair is preferred as described in Section 1.2.2, the Z boson decay will set the event signature for analyses. Due to the difficulties of hadronically and invisibly decaying Z bosons similar to the allhadronic and dileptonic decays of top quark pair, the trilepton channel with a visibly decaying Z boson and a top quark pair in the semileptonic channel is the common signature in analyses.

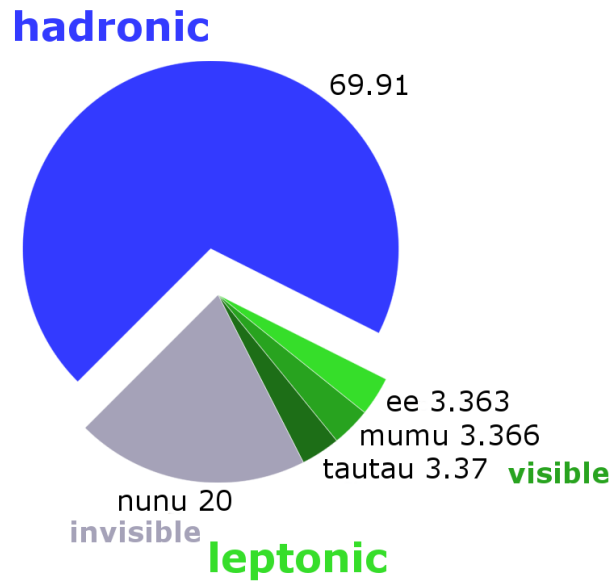

Figure 1.10: The different decay modes of a Z boson as well as the estimation of the corresponding decay rates in percent. The modes can be partitioned into two different groups depending on the type of the decay products: hadronic and leptonic. There are also two leptonic subgroups: visible and invisible [25].

The tZ Coupling

As mentioned in Section 1.2.3, the coupling of the top quark to the Z boson is one of two ways to get access to the top quark's weak isospin. Unlike $t\bar{t}W$ events, $t\bar{t}Z$ events provide a possibility to measure the weak isospin of the top quark directly, which is necessary to confirm the top quark as the bottom quark's weak isospin partner. Using Equation 1.11, the interaction term of the Lagrangian between fermions and the Z boson can be written as

$$\mathcal{L}_{int} = g_Z \ \bar{f}\gamma^\mu \frac{c_v^f - c_A^f \gamma^5}{2} f \ Z_\mu, \tag{1.25}$$

with components described in Section 1.1.2. The constants depending on the fermion of the interaction contains information about the charge of the fermion Q_f, the third component of its weak isospin I_3^f as well as the Weinberg mixing angle θ_W in the following ways:

$$\begin{aligned} c_V^f &= I_3^f - 2Q_f \sin^2(\theta_W) \\ c_A^f &= I_3^f \end{aligned} \tag{1.26}$$

To isolate the third component of the top quark's weak isospin this method requires measurements of its charge as well as the Weinberg angle. A top quark charge of $Q_t = +2/3$ is already confirmed [52] and the Weinberg angle is also known measured by the LEP collaboration [53].

A precise direct measurement of the top quark's weak isospin will either confirms the top quark as the bottom quark's weak isospin partner or indicates the existence of physics beyond the Standard Model.

2 Experimental Setup

The Standard Model of particle physics contains all elementary particles, but only the light ones are observed in nature. Heavy elementary particles have to be produced artificially to study their properties. In the past, several particle accelerators, for instance the Stanford Linear Collider (SLC), colliding electrons and positrons, the proton-antiproton accelerator Tevatron at Fermilab or the Large Hadron Collider (LHC) at Cern, which operates nowadays, have been used to study different production mechanisms and the emerging particles at different centre-of-mass energies.

To reach higher energies, the structure of modern accelerators changed compared to the older models, which were linear particle accelerators. Linear colliders would need more space to accelerate particles to higher energies. This issue can be fixed by building modern particle accelerators in a circular form, so that the particle can be accelerated several times by the same module. Due to synchrotron radiation, the colliding particles of the beams also changed from light leptons (electrons and positrons) to heavy hadrons (protons and antiprotons). This avoids the energy limits the synchrotron radiation would set for lighter particles, since the synchrotron radiation depends on the mass of the accelerated particles.

The currently operating accelerator, the Large Hadron Collider (LHC) at the European Organization for Nuclear Research Cern, is the most powerful particle accelerator in terms of centre-of-mass energy, which operates at a centre-of-mass energy of 13 TeV. Four big experiments are located at the LHC: ATLAS, CMS, ALICE and LHCb. While ATLAS and CMS are the two general purpose detectors, LHCb and ALICE are more specialized in B physics and heavy ion physics, respectively.

This chapter gives an overview over the Large Hadron Collider as well as the ATLAS experiment.

2.1 The Large Hadron Collider

The Large Hadron Collider (LHC) is a synchrotron with a radius of 26.7 km. It collides not only two proton beams, but also beams containing heavier nuclei with a centre-of-mass energy of 7 and 8 TeV during Run I and 13 TeV during Run II at four different interaction

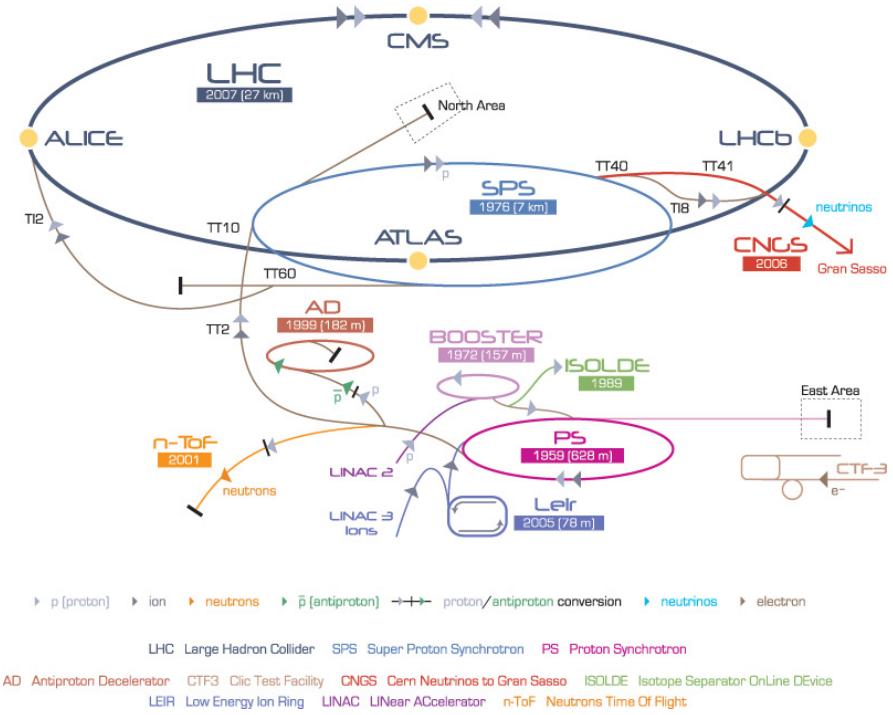

Figure 2.1: A visualization of the accelerator structure at the European Organisation of Nuclear Resarch (CERN) near Geneva, Switzerland © CERN.

points, where the four big experiments are located. Further updates like the high luminosity LHC project (HL-LHC) are supposed to increase the centre-of-mass energy to 14 TeV. The Large Hadron Collider is built in the tunnels of the Large Electron-Positron Collider, which operated until 2000 at the European Organization for Nuclear Research also called CERN (*Conseil Européen pour la Recherche Nucléaire*) near Geneva, Switzerland, which is shown by Figure 2.1.

The acceleration of the particle beams, which are actual several bunches of particles, is divided into different steps. The process starts with the linear accelerator *LINAC 2*, where the particles gain an energy of 50 MeV. Henceforth, the different steps of the particle acceleration are done by circular accelerators. The first one is the *BOOSTER* with a radius of 157 m, which prepares the particles for the injection into the *Proton Synchrotron* (PS) by accelerating them to an energy of 1.4 GeV. After leaving the Proton Synchrotron with an energy of 2 GeV, the particles reach the energy they need for the final acceleration inside the *Large Hadron Collider* of 450 GeV by passing the *Super Proton Synchrotron* (SPS). During their acceleration inside the Large Hadron Collider, each beam of particles obtains their final energy of 6.5 TeV, which corresponds to a centre-of-mass energy of 13 TeV.

Due to the structure of the LHC being a synchrotron and also the high energy of the particle beams, over 1600 dipole and quadrupole magnets are needed to keep the beams on their orbits as well as to focus the bunches of particles as precisely as possible. To fulfil these requirements, magnets with a field strength of 8 T are installed at the Large Hadron Collider. Since only superconducting magnets can produce fields with the needed strength, they have to be cooled down to -271.3°C using liquid Helium.

Furthermore, a quantity, which describes the performance of the Large Hadron Collider, is also essential. This quantity is called *luminosity* L and is defined via

$$L = \frac{n_b N_1 N_2 f}{4\pi\sigma_x\sigma_y} \tag{2.1}$$

with n_b the number of bunches, N_1 and N_2 the number of particles per bunch in beam 1 and beam 2, f the revolution frequency as well as σ_x and σ_y the horizontal and vertical beam size. Knowing the cross section σ_p of a process p, the luminosity can be used to calculate the expected event rate $\dot{N}$ using

$$\frac{dN}{dt} = \sigma_p \cdot L. \tag{2.2}$$

By integrating the luminosity over the data taking period, the resulting *integrated luminosity*, $\int L dt$, is a measurement of the amount of data taken. Figure 2.2 shows the total integrated luminosity of the LHC during the data taking period of 2017. In addition, a comparison of the luminosities of different periods is given by Figure 2.3, which visualizes the success of reaching higher luminosities after each update, except small issues during the run of 2017. Due to Equation 2.2, an increase of the luminosity is very important to achieve an acceptable rate of rare events.

The four big experiments of the LHC known as *A Toroidal LHC ApparatuS* (ATLAS), *Compact Muon Solenoid* (CMS), *A Large Ion Collider Experiment* (ALICE) and *Large Hadron Collider beauty* (LHCb) are located at the four interaction points of the Large Hadron Collider.

The following section gives a more detailed description of the ATLAS experiment.

2.2 The ATLAS Detector

The ATLAS detector [55] is one of two general purpose detectors and also the biggest experiment at the LHC in terms of size. The cylindrical shape of the detector has a length

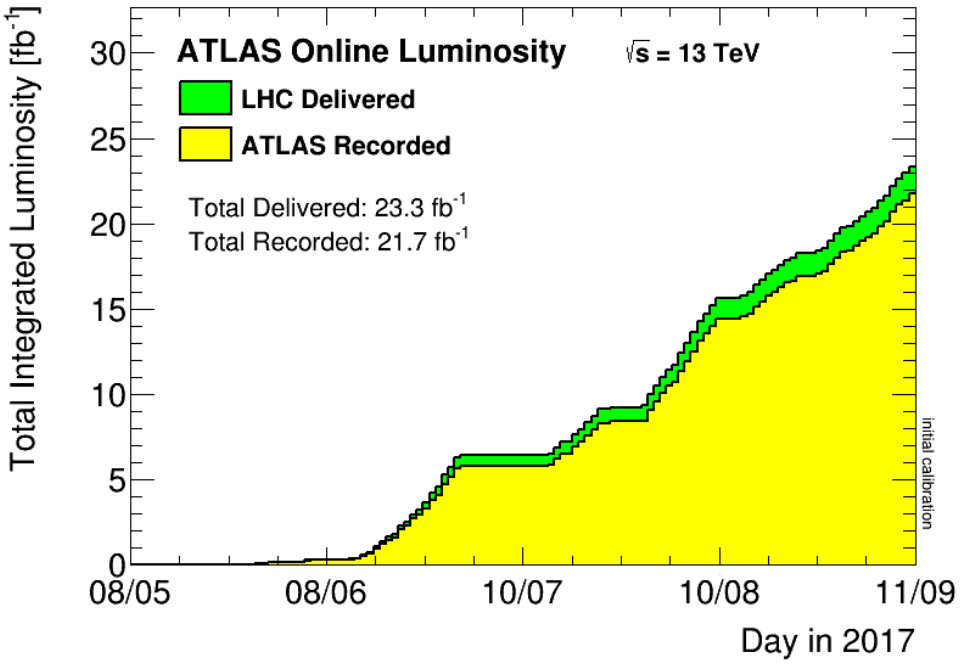

Figure 2.2: The total integrated luminosity of the LHC during the data taking period of 2017 recorded by the ATLAS detector [54].

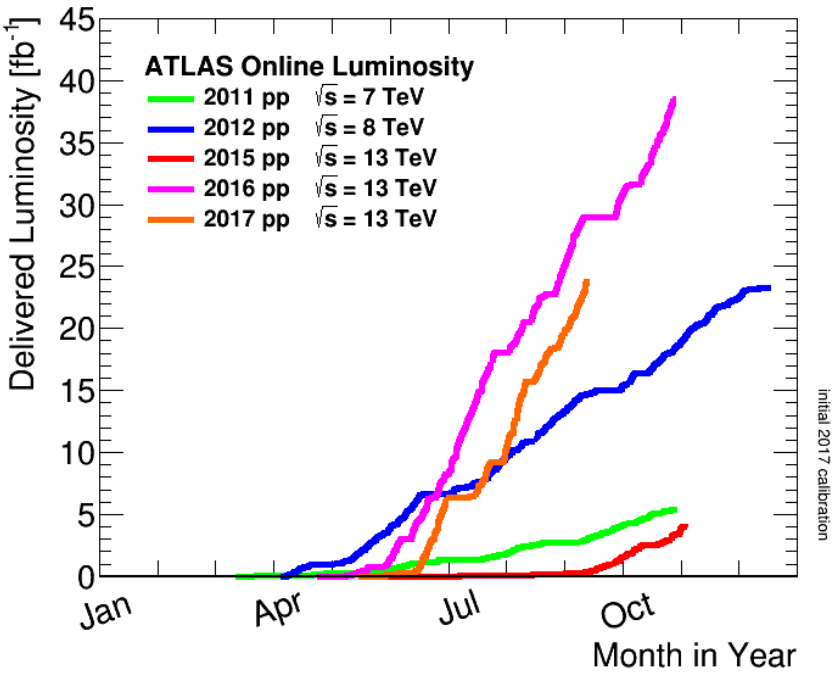

Figure 2.3: Comparison of the delivered luminosities during different data taking periods [54].

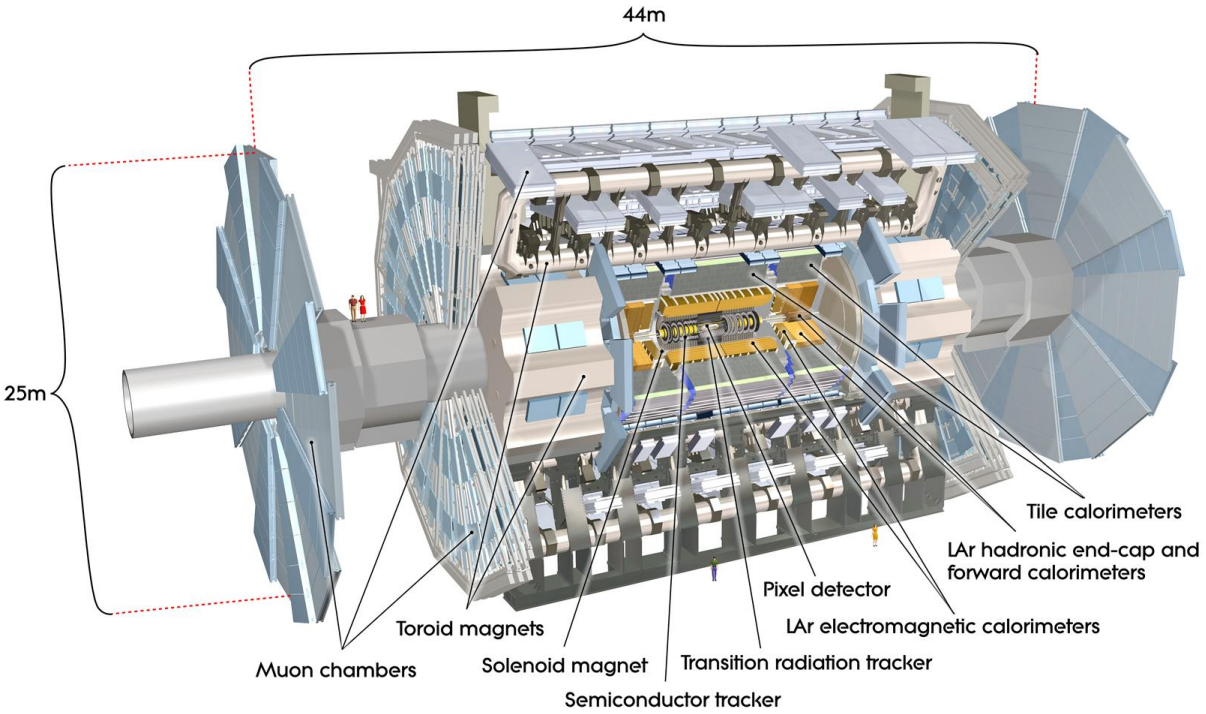

Figure 2.4: An overview of the ATLAS detector © CERN.

of 44 m and a radius of 12.5 m. The detector itself shown in Figure 2.4 is composed of several detector subsystems, which are designed to measure different properties of the final state particles, for instance the flavour, the direction, the momentum or the energy.

The Inner Detector

The most inner part of the detector is called *Inner Detector*, which starts close to the interaction point and therefore requires a radiation-hard material. Like the whole detector, the Inner Detector is composed of different layers. The innermost subcomponent is the *pixel detector* built of plenty semiconductor pixels. The middle part of the Inner Detector is called *semiconductor tracker*. The strip layers of this detector part surround the whole pixel detector and cover a larger area. It is followed by the *transition radiation tracker*, which uses transition radiation information instead of single signals from components like pixels or strips. The task of the Inner Detector is the measurement of the momenta of electrically charged particles and it is also used to apply b-tags. For this purpose, the Inner Detector is surrounded by a 2 T magnetic field of a solenoid magnet system, which bends the tracks of the electrically charged particles. Using the resulting bending radius and kinematic information, the momentum of a particle can be calculated.

The Calorimeter

The middle part of the ATLAS detector, the *calorimeter*, is divided into two different parts, where both parts are located outside the solenoid system. Each calorimeter part consists of alternating layers of high-density material to interact with the particles inside the calorimeter as well as an active material to measure the number of particles in a shower, which is related to the energy of the particles. The *electromagnetic calorimeter* is specialized in particles, which mainly interact via the electromagnetic force, for instance electrons, positrons and photons. It is made of lead (high-density material) and liquid Argon (active material), while the *hadronic calorimeter* consists of steel (high-density material) and plastic scintillator plates (active material). The hadronic calorimeter measures the energy of particles, which pass the electromagnetic calorimeter like hadrons, which are composed of quarks and gluons.

The Muon Spectrometer

The outermost part of the ATLAS detector is the *muon spectrometer*, which is especially designed to measure the kinematics of muons in addition to the previous parts. Due to their higher mass, muons mainly interact via ionisation with the calorimeters not via Bremsstrahlung. Hence, muons deposit only a small fraction of their energy inside the calorimeter and do not shower. Therefore, the task of the muon spectrometer is the measurement of the muons' transverse momentum p_T as well as a precise identification of the muons. Similar to the Inner Detector, the muon spectrometer uses a toroidal magnet system for the momentum measurements.

2.2.1 The ATLAS TDAQ System

At the Large Hadron Collider, the average time between bunch crossings is about 25 ns, which corresponds to a event rate of 40 MHz. Since storing of all that information would lead to a data storage rate of 1 PB/sec, a mechanism is needed to reduce the amount of information to an affordable rate of 450 MB/sec or about 300 Hz. This rate corresponds to 4 PB data per year, which can be used for further offline analysis. The requirements to such a mechanism are a high efficiency, a large reduction of rate and also affordability.

The *trigger and data acquisition* (TDAQ) system of the ATLAS detector shown in Figure 2.5 provides an administrative system, which interprets the signals of different regions of the ATLAS detector, receives the information of selected events and converts this information into datasets, which can be used in further offline analysis. The TDAQ system reduces the rate of data storage from 40 MHz to 1 kHz, which means about

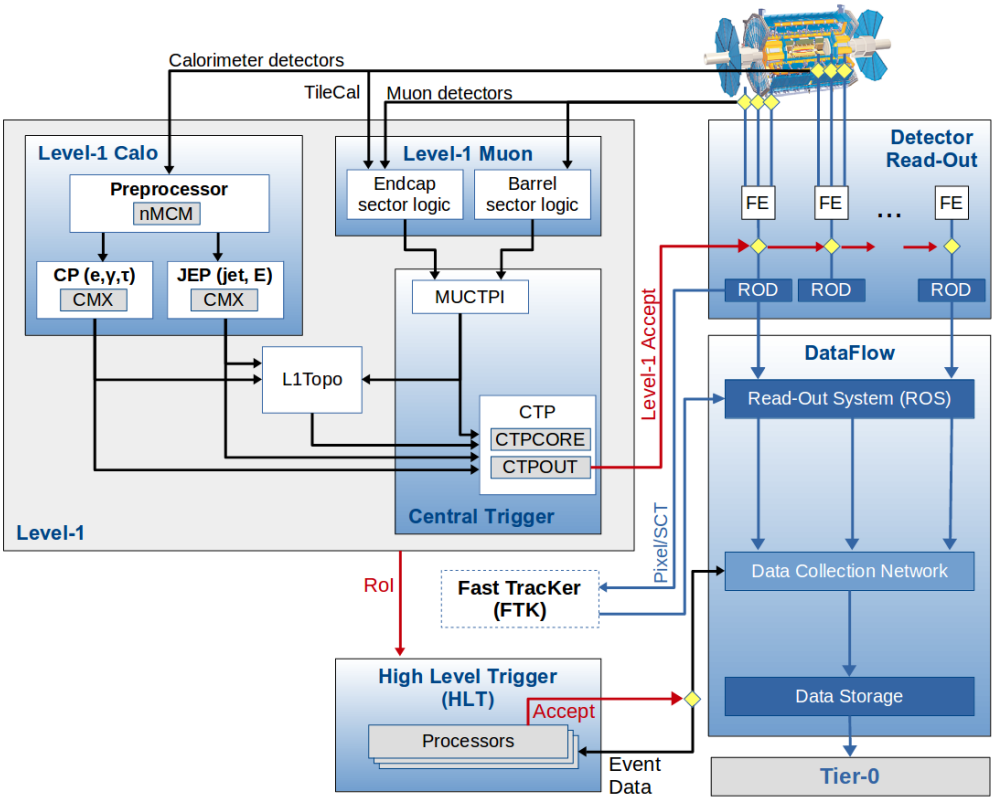

Figure 2.5: Schematic view of the ATLAS Trigger and Data Acquisition system in Run 2 with specific focus given to the components of the L1 Trigger system [56].

0.0025% of all events are stored. Different trigger levels are necessary to achieve such a large reduction of the data rate.

Level-1 Trigger

The first level of the TDAQ system is the *level-1 trigger* system [57] composed of custom electronics. This first trigger level has to make decisions for each bunch crossing based on the measurements of different detectors components. To distinguish new physics from Standard Model events and also to identify events of interest, the level-1 trigger system is looking for events with high-p_T particles like leptons (e, μ, τ), photons or jets, hadronically decaying tau leptons as well as large missing transverse energy $\not{E}_T$ and large total transverse energy E_T, which are handled by the *Calorimeter trigger*. A separate trigger system called *Muon trigger* uses information of the muon spectrometer to identify events with high-p_T muons originating from the interaction point.

Since the level-1 trigger is composed of custom electronics, there is a storage time between the event and the trigger decision of several μs, which is much longer than the bunch crossing period. To compensate this latency of the electronics, a pipelined readout

system is used. This system retains the information of events during the latency in several forms to prevent the loss of those events. After the level-1 trigger system the event rate is reduced to 100 kHz.

High Level Trigger

The software-based *High Level Trigger* system (HLT) [58] is the last part of the ATLAS trigger system. This system takes all information into account within so-called *regions of interest* (ROI), which are constructed from the level-1 trigger decisions. Further criteria like isolation and cuts as well as the consistency of energy deposition and measured tracks within the Inner Detector and the refinement of the level-1 trigger components leads to a further reduction of the events rate to 1 kHz after the HLT. Events, which pass the High Level Trigger system, are stored within the ATLAS permanent storage system.

2.2.2 Definition of Detector Objects at ATLAS

Since the detector only provides the object information as energy and track measurements, the event reconstruction system needs fixed definitions how to build a particle or a jet using the detector information. Expected objects are light leptons (electrons and muon), neutrinos and jets. The following section gives an overview over the different object definitions.

Electrons and Muons

Since electrons are charged light leptons, they leave tracks measured by the Inner Detector as well as energy deposits within the electromagnetic calorimeter observed as *clusters*. They required a transverse momentum of $p_T > 7$ GeV and a pseudorapidity of $|\eta| < 2.47$. Electrons within the range $1.37 < |\eta| < 1.52$ are rejected, due to the worse energy resolution within this range caused by the transition of the barrel and the endcap.

Muons do not deposit a significant amount of energy in the electromagnetic calorimeter, so that the combined information of the inner detector and the muon spectrometer is used to reconstruct them. Their transverse momentum and pseudorapidity requirements are $p_T > 7$ GeV and $|\eta| < 2.4$. In addition, muons also have to pass the muons identification criteria [59]. In the case an electron and a muon share the same track, the muon is rejected.

Since electrons and muons can also originate from decays of heavier particles, those fake leptons have to be distinguished from the prompt leptons of the events. In addition to the requirements above, the light leptons have to fulfil the *isolation criteria* to pass

the selection. These criteria take all tracks of transverse momentum in a cone around the particle candidate into account and check, whether the total sum of those tracks is less than 6% compared to the particle. The radius of the cone depends on the candidate's transverse momentum and a fixed radius parameter R, which is 0.2 for electrons and 0.3 for muons. Leptons, which do not pass this criteria, are rejected.

Neutrinos

Neutrinos only interact via the weak interaction and it is not possible to observe them directly in the detector. Applying energy-momentum-conservation, neutrinos cause a loss of transverse momentum, $\not{E}_T$. The magnitude of this missing transverse momentum is also called missing transverse energy, since the mass of neutrinos can be neglected on this energy scale. The missing transverse momentum is calculated as the negative sum of the transverse momenta of all reconstructed detector objects like leptons and jets and takes also soft terms into account, which correspond to the remaining tracks of transverse momenta in the Inner Detector [60].

Jets

Jets containing plenty different hadrons are results of the hadronization process of quarks or gluons in the events. To reconstruct jets, a special algorithm, the anti-k_T algorithm [61], is used to assign tracks and energy deposits to a certain jet. The radius parameter of the algorithm is $R = 0.4$. All reconstructed jets have to fulfil $p_T > 25$ GeV and $|\eta| < 2.5$.

After the reconstruction of a jet *overlap removal* is applied to prevent for instance double counting of detector objects. Overlap removal checks, whether there are leptons within a ΔR range depending on the lepton's flavour around the jet. The range is 0.2 for electrons and 0.4 for muons. Leptons in the respective range are removed. If the jet contains only a few tracks, the jet is removed instead of the muons, since the deposited energy in the calorimeter originates from the muon and not the jet.

2.2.3 The ATLAS Coordinate System

The ATLAS coordinate system based on spherical coordinates has its centre at the interaction point within the ATLAS detector. As usual for circular particle accelerators, the x-axis points in the direction of the accelerator's centre, while the y-axis points upwards to the surface. Together with the z-axis, which is parallel to the beam, this three axes build the right-handed Cartesian coordinate system of the ATLAS detector. Based on this

Cartesian system new coordinates are introduced, which are used to reconstruct particles from detector objects as well as in further data analysis.

The transverse Momentum p_T

The plane perpendicular to the beam axis formed by the x- and the y-axis of the Cartesian system of the detector is called *transverse plane*. The projection of the particle's three momentum into this plane is called *transverse momentum* and its length defined via

$$p_T = \sqrt{p_x^2 + p_y^2} \tag{2.3}$$

is the first of three quantities, which are used to describe the kinematics of particles in the ATLAS detector.

The Pseudorapidity η

The *pseudorapidity* is based on the first of two angles θ of the spherical coordinate system with $\theta \in [0, \pi]$. Using this angle, it is defined via

$$\eta = -\ln \tan\left(\frac{\theta}{2}\right), \tag{2.4}$$

but the pseudorapidity can also be parametrised by the particle's kinematics

$$\eta = \frac{1}{2} \ln\left(\frac{|\vec{p}| + p_z}{|\vec{p}| - p_z}\right) = \operatorname{arctanh}\left(\frac{p_z}{|\vec{p}|}\right), \tag{2.5}$$

with $\vec{p}$ the particle's three momentum and p_z its component in z direction.
Another very similar quantity is the *rapidity* y

$$y = \frac{1}{2} \ln\left(\frac{E + p_z}{E - p_z}\right), \tag{2.6}$$

with E the particle's energy. One important property of the rapidity is the invariance of a rapidity difference Δy under a Lorentz boost along the z direction. The high centre-of-mass energy of the accelerator allows the usage of the high energy limit in calculations,

where $p_T \gg m$. In this limit the pseudorapidity equals the rapidity and can be used to build a distance parameters, which is invariant under Lorentz boosts along the z direction.

The azimuthal Angle ϕ

The *azimuthal angle* ϕ is the second angle of the spherical coordinate system and describes the orientation of the transverse momentum in the transverse plane. This angle is defined within a range from $-\pi$ to π, where $\phi = 0$, if the transverse momentum is parallel to the x-axis.

The Cone Radius ΔR

To define differences between different detector objects a variable is needed, which is invariant under Lorentz boosts along the z direction and describes the special position of those objects. For this purpose, the difference is defined in the $\eta - \phi$ plane via

$$\Delta R = \sqrt{\Delta\eta^2 + \Delta\phi^2}, \tag{2.7}$$

with $\Delta\eta = |\eta_1 - \eta_2|$ and $\Delta\phi = |\phi_1 - \phi_2|$.

The Four-Momentum in Cartesian Space

Using the transverse momentum p_T, the pseudorapidity η and the azimuthal angle ϕ described above the kinematics of a particle in Cartesian space can be calculated via

$$E = p_T \cdot \cosh(\eta) \tag{2.8}$$
$$p_x = p_T \cdot \cos(\eta) \tag{2.9}$$
$$p_y = p_T \cdot \sin(\eta) \tag{2.10}$$
$$p_z = p_T \cdot \sinh(\eta)\,. \tag{2.11}$$

3 Current $t\bar{t}Z$ Measurements

The following chapter presents the current measurements [62] of the $t\bar{t}Z$ production cross section in the trilepton channel as well as the results of the whole analysis including also $t\bar{t}W$ measurements. The results give access to the top quark's coupling to the Z boson and, hence, it can be used to set first constraints on the third component of the top quark's weak isospin. The cross section is extracted from a data sample containing proton-proton collisions at $\sqrt{s} = 13$ TeV recorded by the ATLAS detector in 2015 by applying likelihood fits in different signal and control regions, which are introduced in Section 3.1. The number of events used in the analysis corresponds to an integrated luminosity of 3.2 fb^{-1}. The results of the cross section measurements presented in Section 3.2 show agreement with the Standard Model predictions.

Besides the trilepton channel, two more regions are defined within the current analysis. The first one targets events with a same-sign muon pair. It has the highest sensitivity to $t\bar{t}W$ events compared to other dilepton regions, due to the misidentification probability of electrons' charge. This region requires two muons with the same charge with $p_T > 25$ GeV, missing transverse momentum $\not{E}_T > 40$ GeV and a scalar sum of the selected leptons and jets $H_T > 240$ GeV as well as at least two b-tagged jets. The main background in this region arises from $t\bar{t}$ events with fake leptons. The second region targets the events from $t\bar{t}Z$ production, where both W bosons decay leptonically. A same-flavour opposite-sign lepton pair with an invariant mass close to the Z mass is required, which is assigned to the Z boson. The remaining leptons can be combined similarly. This system defines a pseudo Z boson, which is labelled as Z_2. The scalar sum of the transverse momentum of the third and the fourth lepton p_{T34} has to fulfil $p_{T34} > 25$ GeV for leptons with the same flavour and $p_{T34} > 35$ GeV for leptons with different flavours, respectively. In addition, different signal regions are defined based on the b-jet multiplicity of an event as well as a control region 4ℓ-ZZ-CR. This region contains exactly three none b-tagged jets and is used to determine the normalisation of ZZ events. The main backgrounds arises from WZ production and Z+jets events with fake leptons.

Variables	3ℓ-Z-2b3j	3ℓ-Z-1b4j	3ℓ-Z-2b4j	3ℓ-noZ-2b
Leading lepton p_T	$>$ 25 GeV	$>$ 25 GeV	$>$ 25 GeV	$>$ 25 GeV
Other leptons' p_T	$>$ 20 GeV	$>$ 20 GeV	$>$ 20 GeV	$>$ 20 GeV
Sum of leptons' charges	± 1	± 1	± 1	± 1
OSSF $\lvert m_{\ell\ell} - m_Z \rvert$	$<$ 10 GeV	$<$ 10 GeV	$<$ 10 GeV	$>$ 10 GeV
n_{jets}	3	≥ 4	≥ 4	≥ 2 and ≤ 4
$n_{b\text{-jets}}$	≥ 2	1	≥ 2	≥ 2

Table 3.1: Summary of event selections in the trilepton signal regions [62].

3.1 The Trilepton Analysis

In the trilepton analysis, three different signal regions are defined. They are sensitive to $t\bar{t}Z$ events and one region targets the $t\bar{t}W$ process, which has also a significant $t\bar{t}Z$ contribution. Each region is expected to have a different signal-to-background ratio. The label of the each region depends on both its b-jet and jet multiplicity. 3ℓ-Z-2b3j is the first region. It requires exactly three jets with at least two b-tagged jets. At least four jets are required in the 3ℓ-Z-1b4j signal region, where exactly one jet has to be b-tagged. The last $t\bar{t}Z$ sensitive region 3ℓ-Z-2b4j requires at least four jets with at least two b-tagged jets. In addition to get sensitive to $t\bar{t}Z$ events, each region requires an opposite-sign same-flavour (OSSF) lepton pair with an invariant mass within a 10 GeV range around the Z boson mass. 3ℓ-noZ-2b is the fourth region, which contains primarily $t\bar{t}W$ events. It requires at least 2 and at most 4 jets with at least 2 b-tagged jets and also excludes events with an OSSF lepton pair, whose invariant mass is within a range of 10 GeV around the Z boson mass.

Furthermore, a control region called 3ℓ-WZ-CR is used to constrain the normalization of the diboson production containing WZ events in data. The region requires exactly three jets, where none of them is b-tagged, as well as three leptons with at least one OSSF pair with an invariant mass within a range of 10 GeV around the Z boson mass. This region is also used to compare the predictions of the Standard Model with data. Figure 3.1 shows different distributions comparing SM predictions with data.

There are also regions to validate the background for the Z and the noZ case in the trilepton analysis. The first one labelled 3ℓ-Z-VR requires at most three jets with exactly one b-tagged jet or exactly two jets, which are both b-tagged, as well as one OSSF lepton pair with an invariant mass within a range of 10 GeV around the Z boson mass. The second validation region 3ℓ-noZ-VR requires at most three jets with exactly one b-tagged jet and excludes any lepton pair with the same definition as for the region 3ℓ-Z-VR. These regions are dominated by WZ as well as $Z+$jets events with fake leptons and fake

Region	Total bkg.	$t\bar{t}W$	$t\bar{t}Z$	Data
3ℓ-WZ-CR	29.5 ± 2.8	0.015 ± 0.004	0.80 ± 013	33
3ℓ-Z-2b3j	0.8 ± 0.26	0.083 ± 0.014	1.93 ± 0.28	4
3ℓ-Z-1b4j	6.7 ± 2.8	0.036 ± 0.011	4.3 ± 0.6	7
3ℓ-Z-2b4j	1.6 ± 0.6	0.065 ± 0.013	5.5 ± 0.7	8
3ℓ-noZ-2b	4.7 ± 2.2	1.59 ± 0.28	1.45 ± 0.20	10

Table 3.2: Expected event yields for signal and backgrounds, and the observed data in the WZ control region and trilepton signal regions used in the fit to extract the $t\bar{t}Z$ cross section. The quoted uncertainties in the expected event yields represent systematic uncertainties including MC statistical uncertainties [62].

leptons from top quark pair production, respectively. Figure 3.2 shows the distribution of the number of electrons for each validation region. They are in good agreement with the background and data modelling within the statistical uncertainties.

3.2 Results of the Cross Section Measurements

To extract the $t\bar{t}Z$ production cross section from the data, a binned maximum-likelihood fit based on the profile-likelihood technique is used to all signal and control regions, which are sensitive to $t\bar{t}Z$ as well as $t\bar{t}W$ events. As a result, the $t\bar{t}Z$ and $t\bar{t}W$ production cross sections are determined individually in one-dimensional fits as well as simultaneously in two-dimensional fits in the analysis. The confidence intervals as well as hypothesis testing are calculated by using a modified frequentist method, which is implemented in RooStats [63]. Figure 3.3 shows a summary of the fit to all regions, which are used in the simultaneous fit to determine the $t\bar{t}Z$ and $t\bar{t}W$ cross section. The following cross sections are the results of the one-dimensional fit:

$$\sigma_{t\bar{t}Z} = 0.92 \pm 0.29(\text{stat.}) \pm 0.10(\text{syst.}) \text{ pb} \tag{3.1}$$

$$\sigma_{t\bar{t}W} = 1.50 \pm 0.72(\text{stat.}) \pm 0.33(\text{syst.}) \text{ pb} \tag{3.2}$$

The cross section results of the two-dimensional fit are shown in Figure 3.4. The normalisation corrections for the WZ background 1.11 ± 0.30 as well as the same corrections for the ZZ background 0.94 ± 0.17 are both obtained from the fit and are compatible with unity. The leading as well as total uncertainties of the fit are shown by Table 3.3. It is also shown that the precision of both cross sections is dominated by the statistical uncertainties, due to a low number of events.

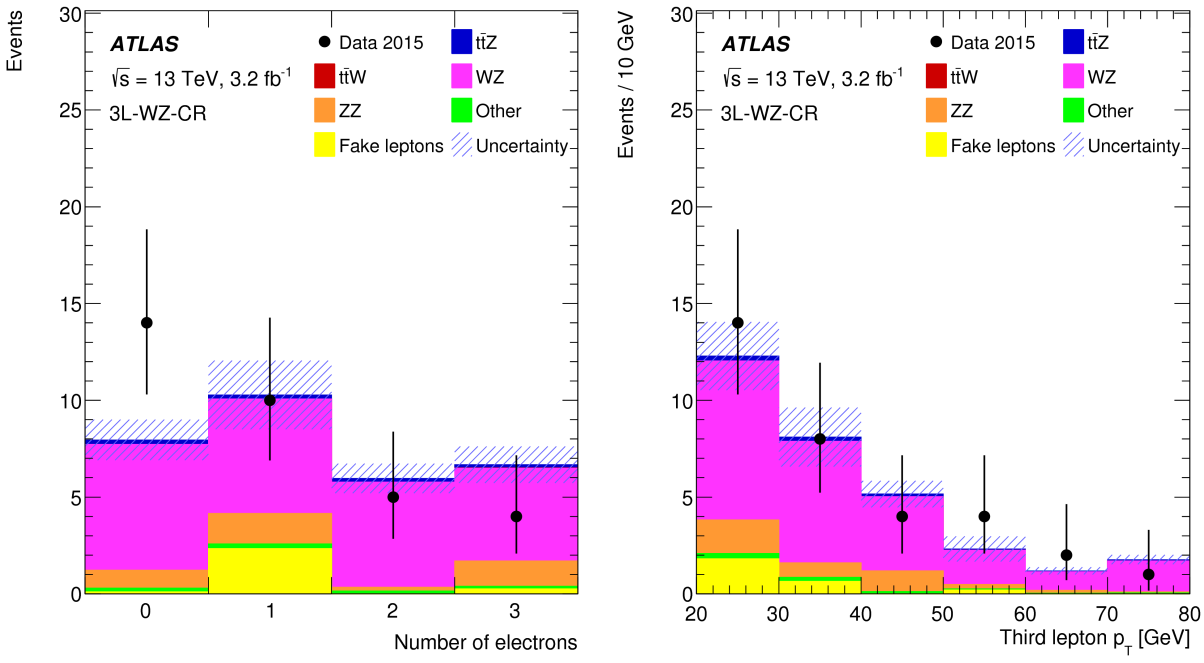

(a) (b)

Figure 3.1: Distributions of *(left)* the number of electrons and *(right)* the third-lepton p_{T} in the 3ℓ-WZ-CR control region before the fit. The background denoted 'Other' contains other SM processes producing three prompt leptons. The shaded band represents the total uncertainty. The last bin of the distribution shown in the *right panel* includes the overflow [62].

Uncertainty	$\sigma_{t\bar{t}Z}(\%)$	$\sigma_{t\bar{t}W}(\%)$
Luminosity	2.6	3.1
Reconstructed objects	8.3	0.3
Backgrounds from simulation	5.3	3.1
Fake leptons and charge missID	3.0	19
Signal modelling	2.3	4.2
Total systematic	11	22
Statistical	31	48
Total	32	53

Table 3.3: List of dominant and total uncertainties in the measured cross section of the $t\bar{t}Z$ and $t\bar{t}W$ processes from the fit. All uncertainties are symmetrised [62].

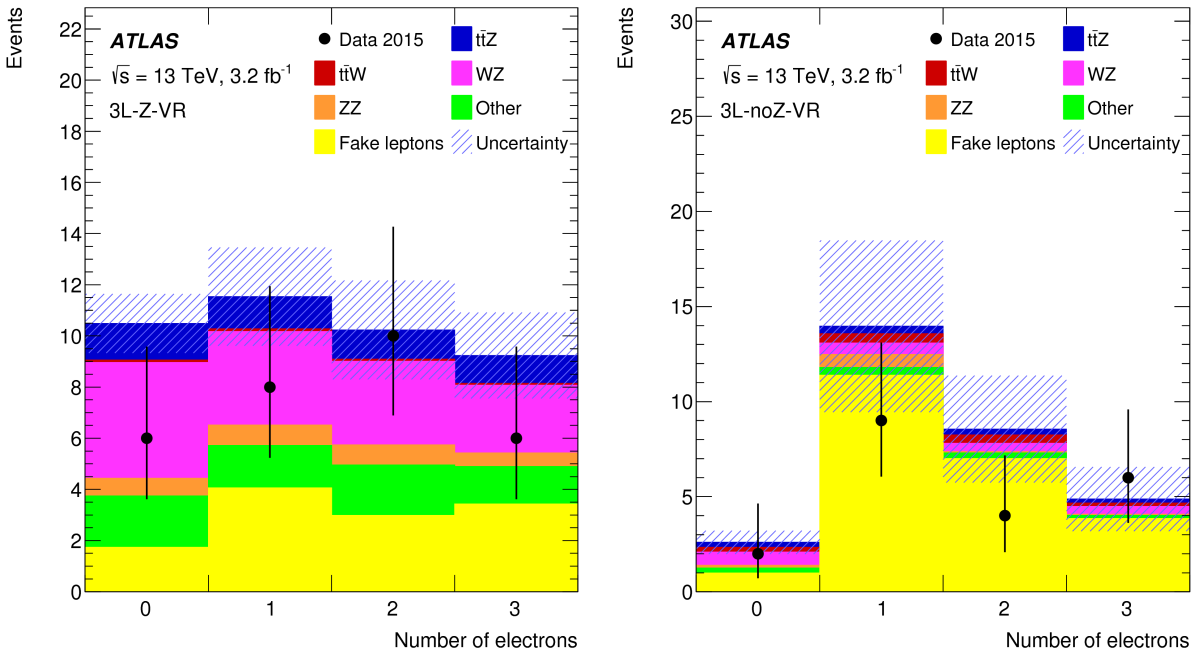

Figure 3.2: Distributions of the number of electrons in the *(left)* 3ℓ-Z-VR and *(right)* 3ℓ-noZ-VR validation regions, shown before the fit. The background denoted 'Other' contains other SM processes producing three promt leptons. The shaded band represents the total uncertainties [62].

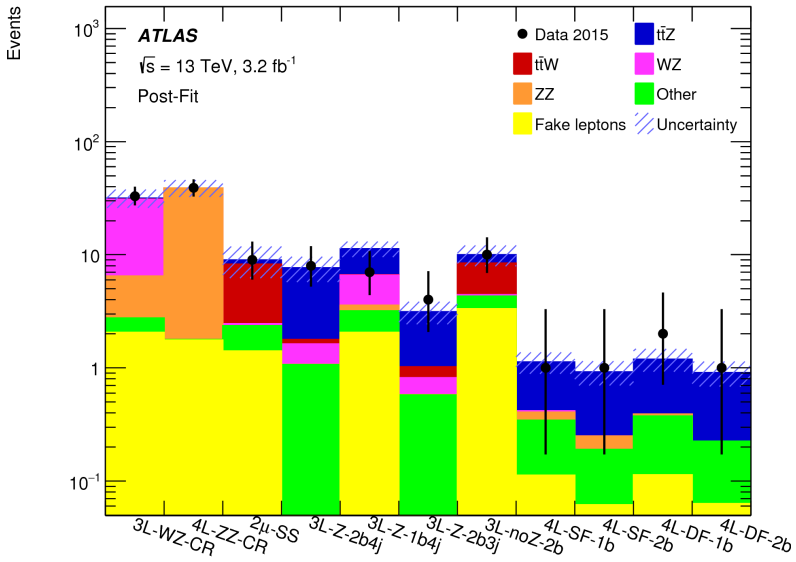

Figure 3.3: Expected yields after the fit compared to data for the fit to extract $\sigma_{t\bar{t}Z}$ and $\sigma_{t\bar{t}W}$ in the signal regions and in the control regions used to constrain the WZ and ZZ backgrounds. The 'Other' background summarises all other backgrounds. The shaded band represents the total uncertainty [62].

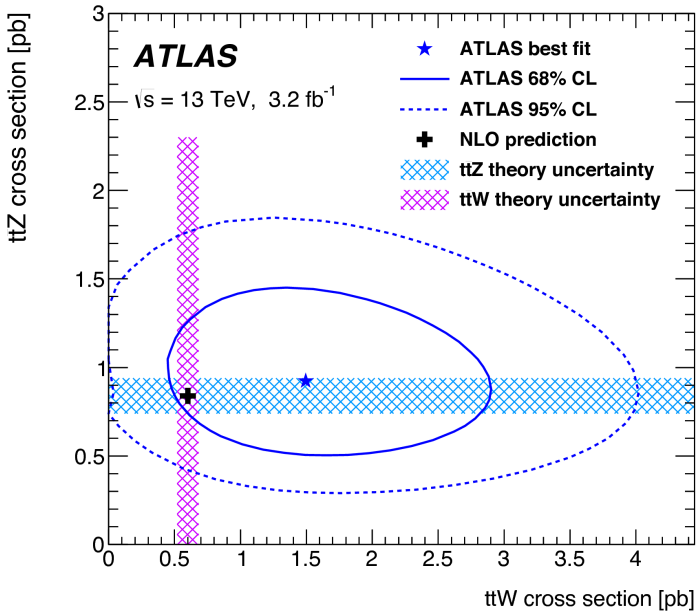

Figure 3.4: The result of the simultaneous fit to the $t\bar{t}Z$ and $t\bar{t}W$ cross section along with the 68 and 95% confidence level (CL) contours. The shaded areas correspond to the theoretical uncertainties in the Standard Model predictions, and include renormalization and factorisation scale uncertainties as well as PDF uncertainties including α_S variations [62].

4 Event Reconstruction

One of the biggest difficulties of modern particle physics experiments is the small cross section of specific processes. Due to the low statistics, even the cross section of the $t\bar{t}Z$ production is not measured precisely, shown by the results of ATLAS and CMS in 1.23 and 1.24.

Furthermore, the signal events have to be identified and distinguished from background events. Several tools based on multivariate techniques like artificial neural networks are used to increase the signal-over-background ratio, which is an indicator of the sample's purity. The input of those tools is composed of different variables, which show separation between signal and background events.

A correct identification of signal events as well as the right assignment between detector objects and partons is necessary for precise measurements. The cross section contains not only information about the probability to observe a certain final state but also information about the coupling of the involved particles.

One requirement to achieve the correct identification of signal events as well as the right assignment between detector objects and particles are clear definitions of each object. Section 4.1 shows the different object definitions, which are used in analyses. A tool which is commonly used in top quark analyses at ATLAS is the KLFitter framework. Section 4.2 describes the functionality of this tool as well as the underlying technique, which are used by the KLFitter.

4.1 Definitions of Event Objects

The main aspect of this thesis is the reconstruction of $t\bar{t}Z$ events, which are introduced in Section 1.3. The event signature of $t\bar{t}Z$ decays is the same as the signature of a decaying top-antitop quark pair with an associated Z boson, which decays either hadronically into a quark-antiquark pair $Z \to q\bar{q}$ or leptonically into a pair of electrically charged leptons $Z \to l\bar{l}$ or neutrinos $Z \to \nu\bar{\nu}$. The visible Z boson decay is preferred. Together with the decay mode of the corresponding top quark pair, it sets the $t\bar{t}Z$ event signature, so that three different $t\bar{t}Z$ signatures are used in analysis: the *tetralepton* channel with a top

quark pair decaying dileptonically, the *trilepton channel* using the semileptonic channel of top quark pair decays and the *dilepton channel* with a top quark pair in the allhadronic channel. This thesis focuses on the trilepton channel.

The trilepton $t\bar{t}Z$ channel is composed of a semileptonically decaying top quark pair and a Z boson, which decays further into a pair of visible leptons, as mentioned above. This signature contains four jets, three leptons as well as a neutrino, which is observed as missing transverse energy in the detector. Due to the large CKM-matrix element, each top quark decays into a b quark and a W boson, which decays further either into a pair of quarks $W \to q_1\bar{q}_2$ or into a lepton and a neutrino $W \to l\nu$. Two b-jets are expected to be observed in $t\bar{t}Z$ events. The label of those b-jets depends on the decay of the W boson, which is hadronical (W_{had}) or leptonical (W_{lep}) with corresponding b-jets b_{had} and b_{lep}. The two remaining jets are expected to be light jets originating from one up-type quark and one down-type quark, respectively, of the hadronically decaying W boson. The two leptons originating from the leptonic Z boson decay are expected to have the same flavour but the opposite electrical charge. In the case of three leptons with the same flavour, the analysis becomes more complex, since this increases the combinatorial background of those events. This issue also appears for jets caused by the level of observation. The process within the detector can be separated into three different levels. The first one is called *parton level*, where the interaction takes place and the particles (quarks, leptons, neutrino) are produced. The next level is the *particle level*. On this level, particles decay and quarks start to form bound states caused by hadronization and parton showering. Those bound states will form the observed jets. After these processes, the detector measures tracks and energy deposits of the jets and the remaining particles, which are arisen on the previous level. This *detector level* is the level of observations. Due to the processes on particle level as well as limitations of the detector, it is not possible to reconstruct the particles on parton level. In fact, it is also very difficult to assign the detector objects to the particles given a trilepton $t\bar{t}Z$ final state. There are four different quarks, which can be assigned by each jet: two b quarks labelled as b_{had} and b_{lep} as well as the decay products of the hadronically decaying W boson, one up-type quark q_u and one down-type quark q_d. The same situation is held for the three leptons. If all three lepton candidates have the same flavour, each of them can be assigned to each lepton of the $t\bar{t}Z$ final state. Fortunately, combinatorics can be reduced, since a distinction between the light quarks and the leptons origin from the Z boson is not necessary. Despite this reduction, there are still 12 jet permutations and 3 lepton permutations, which leads to 36 possibilities to assign the detector objects to each of the seven particles for each event. The number of permutations increases further, if other phenomena like final state radiation of gluons are

taken into account. In this case, at least one jet of the $t\bar{t}Z$ events does not correspond to one of the four highest p_T jets.

In addition to the kinematic definitions of detector objects, further variables can be used to facilitate assignment with high probability. The first possibility is called *b-tagging*. A b-tag represents an identification of a jet to be a jet originating from a b quark with a certain probability. Jets with a b-tag value can be assumed to be the b_{had} and the b_{lep} jet.

Since the $t\bar{t}Z$ final state requires an opposite-sign same-flavour (OSSF) lepton pair as the decay product of the Z boson, the invariant mass of this lepton pair m_{ll} has to be in a certain range around the Z boson mass m_Z. This mass window is defined as $|m_{ll} - m_Z| < 10$ GeV. These two conditions help to reduce the combinatorics as well as the background of events with the same final state signature as $t\bar{t}Z$ events.

Furthermore, the detector objects have to fulfil their individual requirements, which are listed below.

- **Leptons:** Three leptons are required, either two leptons of the same flavour and one of the other one or three leptons of the same flavour and non lepton of the other one. Their transverse momenta have to be above the threshold of 25 GeV for the highest p_T lepton and above 20 GeV for the two remaining leptons. They also have to be in a certain pseudorapidity range based on their flavour. For muons, this range is set to $|\eta| < 2.5$, while electrons have to be in a bit smaller range of $|\eta| < 2.47$. In addition, electrons within a range of $1.37 < |\eta| < 1.52$ are rejected as described in Section 2.2.2.

  Due to their short lifetime, tau leptons are not observed directly within the ATLAS detector but via its decay products. The decay into an electron or a muon with corresponding neutrinos $\tau \to \bar{\nu}_l l \nu_\tau$ ($l = e, \mu$) is one possibility. This has to be taken into account, when events containing electrons and muons are part of the analysis, since leptonically decaying tau leptons will fake the rate of events with electrons and muons.

  Further on, electrons and muons have to fulfil the isolation criteria also described in Section 2.2.2 as well as trigger activities have to be found for those candidates depending on the lepton flavour.

- **Neutrinos:** Since neutrinos interact only via the weak interaction, thus they are not detected within the ATLAS experiment, neutrinos are only observed as missing transverse momentum. Neutrinos are part of the main process and so a certain amount of missing transverse energy is expected, which leads to a common missing

transverse energy threshold of about 30 GeV in several top quark analyses. In this analysis, a cut on the missing transverse energy is not used.

- **Jets:** In $t\bar{t}Z$ events two b-jets and two light jets are expected. As mentioned above, different phenomena like final state radiation of gluons can change the number of jets in an event. To take them into account, at least three jets are required in the current analyses. In this thesis, events with at least three jets are used to get access to events, where one of the jets is missing, due to kinematics reasons. Chapter 5 goes into more detail regarding this topic.

The following section introduces the *Kinematic Likelihood Fitter* (KLFitter) [8]. This tool uses a kinematic likelihood fit, which will also be described in more detail, to calculate the probabilities of different assignments between detector objects and particles on parton level. The KLFitter is a common tool for top quark analyses in ATLAS and is also one of the main aspects of this thesis.

4.2 The KLFitter Framework

The kinematic variables of each particle in the final state are necessary for precise measurements of different properties of interest, for instance couplings of a certain particle like the top quark. Since several phenomena like parton showers on particle level prevent the access to that information, observations on detector level are the only way to reconstruct those particles. For this purpose, a method is needed, which is able to assign correctly objects on detector level to particles on parton level. One of those methods is the usage of kinematic likelihood fits. This method is used in this thesis and is explained in Section 4.2.1. The KLFitter framework is a common tool used in several top quark analyses in the ATLAS collaboration, which uses kinematic likelihood fits to assign detector objects to particles and to reconstruct their kinematics. The *Bayesian Analysis Toolkit* (BAT) [64] is the base of the framework. This toolkit uses Bayes' Theorem and a likelihood function to estimate the parameters of a certain model. Section 4.2.2 describes the assignment of detector objects and the reconstruction of particle kinematics using the KLFitter framework.

4.2.1 The Operating Principle of KLFitter

In statistics and probability theory, the *Bayes' Theorem* describes the probability of an event A to be true depending on the observation of a second event B. This probability called *posterior probability* $P(A|B)$ can be expressed as follows:

$$P(A|B) = \frac{P(B|A) \cdot P(A)}{P(B)} \tag{4.1}$$

Within the formula above, $P(A)$ is the *prior probability*, which describes the probability an event A occurs before the observation of the events B, while $P(B)$ gives the probability to observe the event B without further assumptions. The main part of a kinematic likelihood fit is called *likelihood function*, which is represented by $P(B|A)$ in Equation 4.1. This part contains information about the probability to observe an event B assuming a certain hypothesis A. Bayes' Theorem leads to an updated version of the probability distribution of a hypothesis A, since A and B are not independent events.

Regarding measurements of particle kinematics within the detector, this theorem can be used to estimate the right assignment between detector objects and particles as well as the kinematics on parton level, since the kinematics like transverse momenta and energies can only be measured with a certain precision. Due to different methods, which are used in the detector, the kinematic uncertainties of those variables show different behaviours. The relative energy uncertainty of the calorimeter σ_E/E decreases with higher particle energies with an $1/\sqrt{E}$ behaviour, where additional phenomena like electronic noise are not taken into account:

$$\frac{\sigma_E}{E} \sim \frac{1}{\sqrt{E}} \tag{4.2}$$

The opposite is the case for measurements of the transverse momentum. As explained in Section 2.2, the Inner Detector as well as the muon spectrometer uses magnetic fields to bend the tracks of electrically charged particles. The transverse momentum can be calculated by using the resulting bending radius. Since the bending radius increases with higher transverse momentum, the relative uncertainty of the transverse momentum gets worse shown in the following relation:

$$\frac{\sigma_{p_T}}{p_T} \sim p_T \tag{4.3}$$

To build a likelihood function, which both describes the kinematics of the final state particles and takes the detector resolution into account, functions are needed to connect the information on detector and on parton level. Those functions are called *transfer functions* $W(E^{meas}|E^{true})$. They contain information about the probability to measure

an object in the detector with an energy E^{meas} assuming the corresponding particle has an energy of E^{true}. At a centre-of-mass of $\sqrt{s} = 7$ TeV and $\sqrt{s} = 8$ TeV the transfer functions are modelled by

$$W\left(E^{\text{meas}}|E^{true}\right) = \frac{1}{\sqrt{2\pi}\left(p_2 + p_3 p_5\right)}\left[\exp\left(\frac{\left(\Delta E - p_1\right)^2}{2p_2^2}\right) + p_3 \exp\left(\frac{\left(\Delta E - p_4\right)^2}{2p_5^2}\right)\right], \tag{4.4}$$

with $\Delta E = (E^{true} - E^{meas})/E^{true}$ as well as p_1, p_2, p_3, p_4 and p_5 energy depending parameters. In case of muons, the energy is replaced by the transverse momentum $W(p_T^{meas}|p_T^{true})$. Since the LHC upgrade from a centre-of-mass energy of 8 TeV to 13 TeV, the transfer function based on the 8 TeV analyses are still in use. The modelling of new transfer function using 13 TeV samples is already in progress [65].

To improve the functionality of the likelihood function, additional constraints based on the particle variables can be used to extent the function. Since the final state particles are decay products, the mass and the decay width of their mother particles are also taken into account by the likelihood function. For a top quark final state with associated Z boson production, the mass of the top quark and its decay width as well as the mass and the width of both the W boson and the Z boson are used in the likelihood function. These additional constraints are included in the likelihood function as Breit-Wigner functions parametrised with the mass and the decay width of the three mother particles via

$$B(x|m_p, \Gamma_p) \sim \frac{1}{(x^2 - m_p^2)^2 + (m_p \Gamma_p)^2}, \tag{4.5}$$

with $p = t, W, Z$. Both the transfer function and the Breit-Wigner function as well as their parameters and physical properties are included in the KLFitter framework.

4.2.2 Particle Reconstruction using KLFitter

The KLFitter framework reconstructs final states of particle interactions by fitting kinematic variables to a likelihood function. This function is made of transfer functions $W(E^{meas}|E^{true})$ to take the detector resolutions into account as well as Breit-Wigner functions, which represent further constraints on the kinematics of the final state particles. The likelihood function has to be adapted to the signature of the final state.

Originally, the KLFitter framework was supposed to reconstruct top quark pairs in the semileptonic decay channel. For this purpose, the framework provides transfer functions

for the kinematics of each quark as well as for the lepton and the neutrino, which influence the energy variation of the particles. Furthermore, the invariant masses of the four different particle systems are calculated within the KLFitter framework, which have to follow the corresponding Breit-Wigner distributions. The first two systems result from both W boson decays, where one W boson decays hadronically into a pair of quarks and the other one decays leptonically into a lepton and its corresponding neutrino. The invariant masses of both the $q\bar{q}'$ system and the $l\nu_l$ system have to follow the $B(x|m_W, \Gamma_W)$ distribution. In the same way, the remaining $b_{lep}W_{lep}$ and $b_{had}W_{had}$ systems have to follow the $B(x|m_t, \Gamma_t)$, respectively.

These constraints of the invariant masses of the four decay systems as well as the contribution of the transfer functions are combined in the following likelihood function:

$$\begin{aligned} L_{t\bar{t}} = {} & B\left(m_{q_1q_2q_3}|m_t, \Gamma_t\right) \cdot B\left(m_{q_1q_2}|m_W, \Gamma_W\right) \cdot B\left(m_{q_4l\nu}|m_t, \Gamma_t\right) \\ & \cdot B\left(m_{l\nu}|m_W, \Gamma_W\right) \cdot \prod_{i=1}^{4} W_{\text{jet}}\left(E_{\text{jet},i}^{\text{meas}}|E_{\text{jet},i}^{true}\right) \cdot W_l\left(E_l^{\text{meas}}|E_l^{true}\right) \\ & \cdot W_{\text{miss}}\left(\not{E}_{T,x}^{\text{meas}}|p_x^{\nu}\right) \cdot W_{\text{miss}}\left(\not{E}_{T,y}^{\text{meas}}|p_y^{\nu}\right) \end{aligned} \tag{4.6}$$

The $t\bar{t}$ likelihood function is the basis for further and more complex analyses and can be modified to reconstruct other final states, for instance $t\bar{t}Z$ or $t\bar{t}H$. It is also possible to use other kinematic variables instead of energies and momenta. Moreover, the two transfer functions W_{miss} set the relation between the components of the missing transverse energy $\not{E}_{T,x/y}$ and the corresponding components of the neutrino momentum $p_{x/y}^{\nu}$, since the kinematics of the neutrino can only be calculated by applying energy and momentum conservation. Equation 4.6 shows the $t\bar{t}$ likelihood function assuming an electron as the lepton of the final state. Since energy measurements of muons are more complicated, the transfer function $W_l\left(E_l^{\text{meas}}|E_l^{true}\right)$ is replaced by $W_l\left(p_{T,l}^{\text{meas}}|p_{T,l}^{true}\right)$ for final states with a muon.

KLFitter performs a kinematic likelihood fit using a given function like Equation 4.6 by varying the used kinematic variables of the particles, when the framework is executed. This procedure stops if the likelihood function reaches its maximum using the fitted and measured parameters.

As mentioned in the introduction of Chapter 4, the right assignment between detector objects and particles on parton level is essential for advanced measurements. Assuming a $t\bar{t}$ final state and neglecting the distinction between both light quarks, there are still 12 different possible permutations. Besides the fitting of kinematic variables, KLFitter can

also be used to find the assignment between detector objects and particles with the highest probability. For a wrong permutation, either the transfer functions or the Breit-Wigner function would return a small value. A maximized Breit-Wigner function would lead to big differences between the expected particle energy and the measured value, while the invariant mass of particles within the expected energy range would be far away from the invariant mass of their mother particle in the case of a wrong permutation. Due to this fact, the value of the likelihood function can be used to distinguish between correct and wrong assignments, therefore, a kinematic likelihood fit is performed for each permutation of the final state particles.

To improve this ability of the KLFitter framework, an new quantity, the *event probability*, is introduced, which takes further information into account. For each permutation i, the event probability is defined as a weighted likelihood value normalized to all other permutations of the event as follows:

$$p_i = \frac{L_i \Pi_j \Delta p_{i,j}}{\Sigma_i L_i \Pi_j \Delta p_{i,j}}. \tag{4.7}$$

Similar to the value of the likelihood function, large values of the event probability are related to the permutation, which is very likely to be the right assignment. After the evaluation of all possible permutations of an event, the permutation with the highest event probability is assumed to be the best estimate of the right assignment between detector objects and particles. KLFitter will return this permutation as the reconstructed event.

To support this process, KLFitter provides different options, which decide the content of the weights in Equation 4.7. There are two different options for jet assignments. The first one is called *NoTag*. Using this option, KLFitter will not take any further information about the jets into account. Only the kinematic information about the jets is used to estimate the right assignment. The event probability will be calculated with weights, which equal unity. The second option for jets is called *WorkingPoint*, which uses the b-tag information of the jets to weight the likelihood value in Equation 4.7. The resulting weights of this option are defined via

$$\begin{aligned} \Delta p_{i,j} = &\begin{Bmatrix} \varepsilon_b, & b_{lep} \text{ tagged} \\ (1-\varepsilon_b), & b_{lep} \text{ not tagged} \end{Bmatrix} \cdot \begin{Bmatrix} \varepsilon_b, & b_{had} \text{ tagged} \\ (1-\varepsilon_b), & b_{had} \text{ not tagged} \end{Bmatrix} \\ &\cdot \begin{Bmatrix} \varepsilon_l, & q_u \text{ tagged} \\ (1-\varepsilon_l), & q_u \text{ not tagged} \end{Bmatrix} \cdot \begin{Bmatrix} \varepsilon_l, & q_d \text{ tagged} \\ (1-\varepsilon_l), & q_d \text{ not tagged} \end{Bmatrix}. \end{aligned} \tag{4.8}$$

with the matching efficiency ε_b and mismatching efficiency ε_l. The matching efficiency ε_b contains the probability to tag a jet, which originate from a b-quark, as a b-jet, while the mismatching efficiency ε_l represents the probability to tag a light jet as a b-jet. These efficiencies are assigned to each jet of the event by using the MV2C10 algorithm [66]. This algorithm uses a multivariate discriminant, which takes several properties of b hadrons into account. If this discriminant is above a certain threshold, the jet is tagged as a b-jet. This threshold sets the working point of this option. In the current analysis, a working point of 77% is used, which corresponds to a matching efficiency of $\varepsilon_b = 0.77$ and a mismatching efficiency of $\varepsilon_l \approx 0.0077$. These values are determined by using the MV2C10 algorithm on Monte-Carlo samples. Since it is very unlikely to assign a b-tag to a light jet, the event probability of permutations containing a b-tagged jet on a position of a light jet is much lower compared to events with b-jets on the right positions. Unfortunately the probability to miss the assignment of a b-tag to a b-jet of about 23% is still quite high.

Similar to the jet case, there are also different options to determine the lepton pair originating from the Z boson. Since it is easy to assign the right OSSF lepton pair to the Z boson in the case, where the OSSF lepton pair and the lepton of the leptonically decaying W boson do not have the same flavour, these options are only necessary for selections, where all three leptons have the same flavour. The KLFitter framework provides three different options for the lepton distinction. The first one is the *Leading* option, where the lepton with the highest transverse momentum is assigned to the leptonically decaying W boson. Only this lepton is used in the kinematic likelihood fit, while the other leptons are used to reconstruct the Z boson. The second option is called *AmongThree*. Using this option, the invariant masses of all different lepton permutations are calculated and compared to the invariant mass of the Z boson. The lepton pair with the smallest difference between their invariant mass and the Z mass is chosen to be the lepton pair originating from the Z boson. The remaining lepton is again used in the kinematic likelihood fit. The last one is the *Dedicated* option. Unlike the other two options, where only one of the three leptons is used in the kinematic likelihood fit, the dedicated option performs full fits for all lepton permutations including all leptons into the fit. This option requires an extended likelihood function, which contains transfer functions of both additional leptons $W_l\left(E_{l_2}^{\text{meas}}|E_{l_2}^{true}\right)$ and $W_l\left(E_{l_3}^{\text{meas}}|E_{l_3}^{true}\right)$ as well as a mass constraint on the Z boson mass $B\left(m_{l_2l_3}|m_Z,\Gamma_Z\right)$, since the function shown in Equation 4.6 is only able to use one lepton. The likelihood function [67], which is used by the dedicated option, is shown in Equation 4.9.

Lepton pair production via the weak interaction is not the only possibility. Since

lepton pairs can also be produced via the electromagnetic interaction, this has to be taken into account by an additional term in the likelihood, which represents that production mechanism. Besides the Breit-Wigner function of the Z mass distribution, a $1/m^2_{l_2 l_3}$ term also describes the invariant mass constraint of both leptons. The factor f_{on} representing the fraction of the so-called *on-shell* contribution of the Z boson weights both parts of the mass constraint. The normalization constant c_{norm} equals a cut-off value, which avoids the singularity for $m_{l_2 l_3} \to 0$. The on-shell fraction f_{on} as well as the normalization factor c_{norm} are determined by using mass distributions on parton level within Monte-Carlo samples.

$$
\begin{aligned}
L_{t\bar{t}Z} = {} & B\left(m_{q_1 q_2 q_3} | m_t, \Gamma_t\right) \cdot B\left(m_{q_1 q_2} | m_W, \Gamma_W\right) \cdot B\left(m_{q_4 l \nu} | m_t, \Gamma_t\right) \\
& \cdot B\left(m_{l\nu} | m_W, \Gamma_W\right) \cdot \prod_{i=1}^{4} W_{\text{jet}}\left(E^{\text{meas}}_{\text{jet},i} | E^{true}_{\text{jet},i}\right) \cdot W_l\left(E^{\text{meas}}_{l} | E^{true}_{l}\right) \\
& \cdot W_{\text{miss}}\left(\not{E}^{\text{meas}}_{T,x} | p^{\nu}_{x}\right) \cdot W_{\text{miss}}\left(\not{E}^{\text{meas}}_{T,y} | p^{\nu}_{y}\right) \\
& \cdot W_l\left(E^{\text{meas}}_{l_2} | E^{true}_{l_2}\right) \cdot W_l\left(E^{\text{meas}}_{l_3} | E^{true}_{l_3}\right) \\
& \cdot \left[f_{on} \cdot B\left(m_{l_2 l_3} | m_Z, \Gamma_Z\right) + (1 - f_{on}) \cdot \frac{c_{norm}}{m^2_{l_2 l_3}} \right]
\end{aligned}
\tag{4.9}
$$

Both likelihood functions shown by Equation 4.6 as well as by Equation 4.9 are used to reconstruct $t\bar{t}Z$ events. The first one is used by selecting the *Leading* or the *AmongThree* leptons option, while the second likelihood function is used by the dedicated option, where all leptons are included into the kinematic likelihood fit. Since both likelihood functions are needed to reconstruct all possible flavour combinations in the case of three leptons, the modified likelihood functions, which will allow the KLFitter framework to reconstruct events containing only three jets, are based on the $t\bar{t}$ likelihood function shown by Equation 4.6 as well as the dedicated $t\bar{t}Z$ likelihood function shown by Equation 4.9. Section 5.1.2 thematised the construction of the likelihood functions for events with three jets based on the analysis of events with a missing jet in Section 5.1.1.

4.3 Analysis of the KLFitter Performance

To test the performance and the efficiencies of the modified likelihood for events with three jets, the KLFitter framework was applied to Monte-Carlo samples used in the current $t\bar{t}Z$ analysis containing $t\bar{t}Z$ events as signal and diboson production as the main background of the $t\bar{t}Z$ signal, respectively, as well as to data samples taken over the years 2015 and

2016. The behaviour of the reconstruction algorithm relating to signal and background events is evaluated by determining the matching efficiencies between the reconstructed objects and the truth information, which corresponds to the kinematics of the particles on parton level. Additionally, comparisons of different variables between Monte-Carlo data and real data are used in signal and control regions of the current $t\bar{t}Z$ analysis to cross-check the functionality of the framework.

Section 4.3.1 gives an overview over the used Monte-Carlo samples and the generators, which are used to construct the file. To access the different efficiencies for the evaluation, a C++ class performs assignment tests between the reconstructed and the truth objects. This class is based on a software package [67], which was used to study the performance of the $t\bar{t}Z$ likelihood with four jets, and is introduced in Section 4.3.2.

4.3.1 The Monte-Carlo Samples

In this thesis, the Monte-Carlo samples of the current $t\bar{t}Z$ analysis are used to determine the matching efficiency between truth and reconstructed objects and evaluate the performance behaviour of the algorithm used by the KLFitter framework. These samples contain $t\bar{t}Z$ events used as signal as well as diboson production containing four leptons as well as $lll\nu$ and $ll\nu\nu$ in the final state, which represents the main background of the signal.

The $t\bar{t}Z$ signal events consisting of $t\bar{t}l^-l^+$ events with $l = e, \mu, \tau$ are generated at two different levels: Leading order with up to one additional quark in the matrix element per event as well as next-to-leading order. Since the current $t\bar{t}Z$ analysis only uses the next-to-leading order samples, these are the signal samples used in this thesis. The $t\bar{t}Z$ events are generated by MADGRAPH5_aMC@NLO [45] using a matrix-element calculation and PYTHIA8 [68], which simulates the parton showering process. Moreover, the contribution of the virtual photon γ^* as well as the interference part of the virtual photon and the Z boson γ^*/Z are included in both samples. The software A14 tune [69] and the NNPDF2.3 PDF set [70] support the generation of the events.

The diboson events are generated by SHERPA 2.1 [71] to simulate the parton shower process supported by the CT10 PDF [72] set. In addition to the generators above, further software is needed to take other phenomena as well as the detector response into account. The EVTGEN [73] software models the decay, which involves heavy quarks, while the GEANT4 [74, 75] software package simulates the response of the ATLAS detector.

4.3.2 Determination of the Likelihood Efficiencies

The NtupleReader [67] is a software package created to evaluate the performance of the $t\bar{t}Z$ likelihood function introduced in Section 4.2.2 by comparing the truth information on parton level to the reconstructed objects of the KLFitter output. Since the original likelihood functions require at least four jets, some of the variables used in the package have to be redefined for events containing only three jets. The used C++ class has the same functionality as the NtupleReader and uses the variables modified for the three jet case.

The class starts the evaluation by checking the presence of the particles. If an event contains a jet within a range of $\Delta R = 0.3$ around a quark in the $\eta - \phi$ plane, the corresponding quark is tagged as *IsPresent*. In the case more than one jet matches a quark in this analysis stage, a *MultiMatch* variable will be set. The presence status of the different quarks is summarized in further variables. *AllJetsWithinThree* indicates, whether the first three leading-p_T jets match the three quarks expected in events with a missing jet. Since KLFitter uses the four leading-p_T jets in the fit, this variable is only necessary for events including initial or final state radiation. The range in the $\eta - \phi$ plane changes to $\Delta R = 0.1$ for leptons.

In the next step, the class compares the truth particles with the reconstructed ones using the jet IDs of the KLFitter output. A quark is labelled as *IsMatched*, if the corresponding jet of the KLFitter reconstruction is in the same ΔR range as in the presence checks. Leptons have to fulfil the same matching criteria with the respective lepton range.

Since the KLFitter output only provides the kinematics of the final state particles (b_{had}, b_{lep}, uQ and dQ on parton level), the top quarks have to be reconstructed by adding the four momenta of their decay products for both the truth and the reconstructed case. Their kinematics are compared in the same way as for the other quark. The hadronically decaying top quark, t_{had}, and the leptonically decaying top quark, t_{lep}, respectively, is matched, if the distance of the quark and the corresponding reconstructed object is less than $\Delta R = 0.4$ in the $\eta - \phi$ plane. The variables *THadMatched* and *TLepMatched* will be set, if the respective top quark is matched. For the hadronically decaying W boson W_{had}, the matching of the light quark is sufficient to get the label *WHadMatched*. These matching variables can be used to select specific events with three jets to analyse each possibility separately by picking events, where one of the four expected quarks is not present. The efficiencies are calculated by measuring the fraction of events, where the respective matching tag is set.

Furthermore, the C++ class gives access to the kinematic variables of the Ghost Jet, which replaces the missing jet in the kinematic likelihood fits. The analysis of the Ghost

Jet is essential to evaluate the performance of the three jet likelihood. Its kinematics are also used in the reconstruction of the hadronically decaying top quark, since the Ghost Jets replaces the missing jet in the analysis.

Since the modified likelihood functions have less constraints compared to the case with at least four jets, an analysis of the fit performance is important for the KLFitter evaluation. For this purpose, the C++ class gives access to the variables of the error output of the KLFitter.

5 Reconstruction of $t\bar{t}Z$ Events with three Jets in the trilepton Channel

A decent number of events is necessary to measure physical quantities with a certain precision. The latest ATLAS $t\bar{t}Z$ analysis described in Chapter 3 includes events with three jets in signal regions, but kinematic likelihood fits are not used to reconstruct the final states of those events, since the KLFitter tool is not able to reconstruct $t\bar{t}Z$ final states with three jets. It is necessary to analyse events with three jets to determine possible modifications of the likelihood functions, which are used in the current $t\bar{t}Z$ reconstruction software.

Section 5.1.1 shows the analysis of events with three jets and the reason as well as the rate of the absence of each quark is discussed. The results of this analysis lead to different possible modifications of the likelihood functions. One of them is described in Section 5.1.2, where the likelihood functions for events with three jets are presented.

These likelihood functions use an artificial pseudojet called *Ghost Jet*, whose reconstruction is based on the results of the analysis of the events with three jets. Section 5.2 describes the reconstruction of the Ghost Jet's kinematic variables as well as the fit methods, which are used to obtain the reconstruction functions.

5.1 Analysis of Events with three Jets

Due to the structure of the detector and the different detector object definitions both presented in Section 2.2, the fourth jet of the top quark pair decay in $t\bar{t}Z$ final states may not be detected as a jet. In this case, a kinematic likelihood fit cannot be used to reconstruct the final state, since the likelihood functions require at least four jet, which lowers the number of events needed in the analysis. This section presents the modifications of the $t\bar{t}$ and $t\bar{t}Z$ likelihood functions as well as the analysis of events with three jets.

Number of Jets per Event	3	4	5	≥ 6
Fraction [%]	30.34	32.29	21.16	15.18

Table 5.1: The fraction of events with three jets, four jets, five jets and at least six jets normalized to the number of events with at least three jets to estimate the advantage of including events with three jets in the event reconstruction.

5.1.1 The Absence of the missing Jet

Before the analysis of events with three jets, the fraction of those events compared to the case of four or more jets is an important information. Only a decent fraction of events with three jets will increase the precision of the analysis. The fraction of events with different jet multiplicities is summarized in Table 5.1. Since about 30% of the events with at least three jets contains exactly three jets, including those events increases the total number of events by about 42 %. This fraction justifies the approach of increasing the number of events used in the analysis by including events with three jets.

The modification of the likelihood functions, which allow the reconstruction of events with three jets, need an analysis of those events in terms of absence fractions and absence reasons. For this purpose, the used tool described in Section 4.3.2 compares the angular information between truth and reconstruction level to determine the presence status of each quark in an event. To estimate the fraction of events with a certain missing quark, the events are counted, where all quarks except the selected one are labelled as present. The result is summarised in Table 5.2. In 60.95 % of all events with three jets, the missing jet is part of the hadronic W boson decay, or to be precise in 25.43 % of the events the missing jet originates from the light up-type quark and in 35.52 % from the light down-type quark. To check the reason of the jet's absence, analysis cuts as well as the limitations of the detector structure are taken into account regarding the kinematic variables of different objects. Table 5.3 shows the fraction of events, where either the transverse momentum of the missing jet is below the threshold set by the analysis selection, or the missing jet is out of the pseudorapidity range of the detector, or both. If the absence of the missing jet is not caused by one of the kinematic limitations, the event is labelled as 'Other'. The large fraction of events with a missing jet originating from the down-type quark of 54.59 % is expected, since the down-type quark is produced via the weak interaction. Due to the vector-axial-vector structure of the weak coupling, the down-type quark is produced in the direction antiparallel to the direction of motion of the W boson.

This leads to a lower transverse momentum in the detector frame and therefore the jet cannot pass the transverse momentum threshold. Furthermore, the large fractions in the 'Other' column are noticeable. They indicate reasons, which are not related to

Missing Quark	Up-type quark	Down-type quark	Lep. b-quark	Had. b-quark
Fraction [%]	25.43	35.52	17.85	21.21

Table 5.2: The fraction of events with a missing light up-type quark, a missing down-type quark, a missing leptonic b-quark and a missing hadronic b-quark, respectively, normalized to the number of events with three present quarks.

Quark\Reason of Absence	p_T threshold	η range	Both	Other
up-type quark	1.53	0.11	0.00	98.35
down-type quark	54.59	5.12	11.61	28.69
lep. b-quark	6.95	0.06	0.00	93.11
had. b-quark	2.90	0.14	0.12	97.08

Table 5.3: The fraction of different absence reasons of each quark of the $t\bar{t}Z$ final state in percent. The entries are normalised row-by-row.

the limitations of the transverse momentum and the pseudorapidity, in above 90 % of the respective events, where a jet is missing, which is not originating from the light down-type quark.

This thesis does not go into further detail about this topic. The method to modify the likelihood functions, which is presented in this thesis, focuses on the jets originating from the hadronic W decay to extract information about the missing jet from the remaining jet. The following section presents the construction of the likelihood functions using information of the hadronically decaying W boson.

5.1.2 The modified Likelihood Function

In each likelihood function shown in Equation 4.6 and Equation 4.9, one transfer function as well as two Breit-Wigner functions depend on the kinematic variables of the missing jet. The input of these three functions has to be modified for the reconstruction of events with three jets. Since the constraints of these functions influence the convergence behaviour of the kinematic fit performed by the KLFitter framework, the removal of the functions would cause significant issues during the fit process. Due to the assumption the missing jet originates from a light quark, the information of the remaining light jet can be used to keep both Breit-Wigner functions. Since both light quarks are part of the same system, a correlation between the kinematic variables of both quarks are expected. Figure 5.1 shows the correlation of the pseudorapidity, the transverse momentum and the azimuthal angle between both light quark. Due to the low number of events with three jets in the $t\bar{t}Z$ Monte-Carlo samples, $t\bar{t}$ samples are used to produce the correlation plots. Using the information of the correlation between both light quarks as well as the high

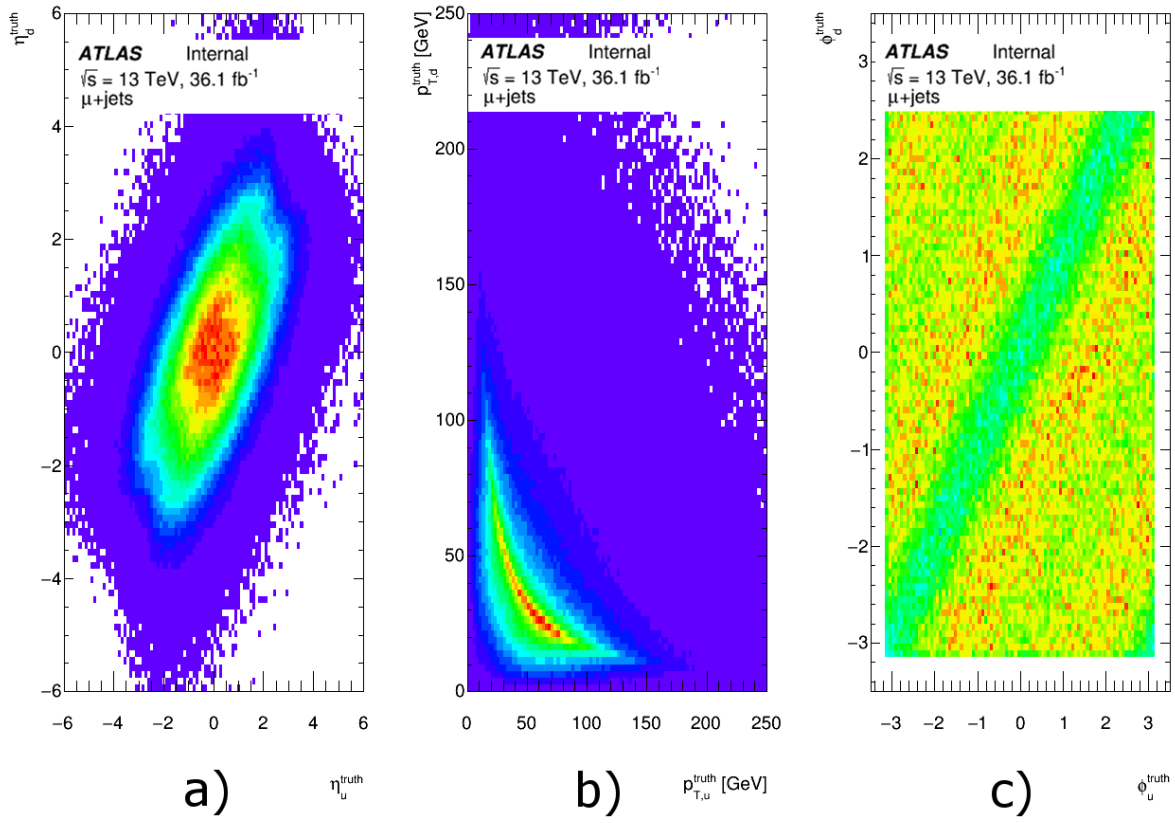

Figure 5.1: The correlation of a) the pseudorapidity, b) the transverse momentum and c) the azimuthal angle between both light quarks on truth level. Due to a lower number of events in $t\bar{t}Z$ samples, $t\bar{t}$ samples are used to visualise the correlation between the kinematic variables and to make the correlation clearly visible.

energy limit, where all light particles can be assumed to be mass less, an artificial object can be constructed, which is able to replace the missing jet in both likelihood functions. This artificial object, in the following called *Ghost Jet*, is used to reconstruct mother particles in the hadronic part of the top quark pair decay to keep the mass constraints in the likelihood functions. Due to the fit methods presented in the following section, an agreement between the kinematic variables of the Ghost Jet and the prediction of the transfer function of the missing jet is not expected, which leads to the removal of the transfer function.

The replacement of the missing light jet by the Ghost Jet leads to the modified likelihood function shown in Equation 5.1, where the missing jet originating from the light down-type quark is labelled q_2. The $t\bar{t}$ likelihood function is modified similarly. The KLFitter framework uses the measured as well as the fitted kinematic variables to calculate the

corresponding value of the likelihood function. Since the kinematic variables of the Ghost Jet are not part of the fit parameters, they have to be calculated twice to get a Ghost Jet for the measured and for the fitted reconstructions. The measured and the fitted light jet are used for the Ghost Jet calculations, respectively.

$$
\begin{aligned}
L_{t\bar{t}Z,3Jets} = {} & B\left(m_{q_1 q_{GJ} q_3} | m_t, \Gamma_t\right) \cdot B\left(m_{q_1 q_{GJ}} | m_W, \Gamma_W\right) \cdot B\left(m_{q_4 l\nu} | m_t, \Gamma_t\right) \\
& \cdot B\left(m_{l\nu} | m_W, \Gamma_W\right) \cdot \prod_{i=1, i\neq 2}^{4} W_{\text{jet}}\left(E_{\text{jet},i}^{\text{meas}} | E_{\text{jet},i}^{true}\right) \cdot W_l\left(E_l^{\text{meas}} | E_l^{true}\right) \\
& \cdot W_{\text{miss}}\left(\not{E}_{T,x}^{\text{meas}} | p_x^{\nu}\right) \cdot W_{\text{miss}}\left(\not{E}_{T,y}^{\text{meas}} | p_y^{\nu}\right) \\
& \cdot W_l\left(E_{l_2}^{\text{meas}} | E_{l_2}^{true}\right) \cdot W_l\left(E_{l_3}^{\text{meas}} | E_{l_3}^{true}\right) \\
& \cdot \left[f_{on} \cdot B\left(m_{l_2 l_3} | m_Z, \Gamma_Z\right) + (1 - f_{on}) \cdot \frac{c_{norm}}{m_{l_2 l_3}^2}\right]
\end{aligned}
\tag{5.1}
$$

5.2 The Ghost Jets

The Ghost Jet is an artificial object based on the kinematic correlation between both light quarks of the W boson's decay. As described in the previous section, the Ghost Jet replaces the missing jet in the likelihood functions to keep the mass constraints represented by Breit-Wigner functions. This chapter discusses the different fit and calculation methods of each kinematic variable of the Ghost Jet and discusses the different behaviour, due to the used methods.

5.2.1 Ghost Jet Pseudorapidity

The pseudorapidity of the Ghost Jet η_{GJ} is calculated by using only information about the light jet's pseudorapidity η_{jet}. Due to the visualisation of the correlation between both light quarks in Figure 5.1, a linear function without a shift in the y-direction is used in the fit. The assumed relation is shown in Equation 5.2.

$$
\eta_{GJ} = A_\eta \cdot \eta_{jet} \tag{5.2}
$$

A Pearson's χ^2-test [76] is used to estimate the parameter A_η by comparing different correlation plots of the light quark and the Ghost Jet, where different values of A_η are used to produce the plots, with the correlation plot of both light quarks. This test is explained in the following.

A comparison of two histograms tests the hypothesis, that both histograms are produced by the same distribution. Originally, the χ^2-test uses unweighted histograms with the same number of bins, which is labelled as r in the following. The total number of events in each histogram is calculated via

$$N = \sum_{i=1}^{r} n_i, \tag{5.3}$$

$$M = \sum_{i=1}^{r} m_i, \tag{5.4}$$

where n_i and m_i describe the number of events in the i-th bin, respectively. The hypothesis, that a values p_i for each of the r bins exist, which represents the probability of a value being measured in the i-th bin in two different experiments represented by the two histograms and also fulfils

$$\sum_{i=1}^{r} p_i = 1, \tag{5.5}$$

equals the hypothesis of identity. This makes the number in each bin a random variable with a distribution approximated by a Poisson distribution

$$f(k) = \frac{\exp\left(-X \cdot p_i\right) \cdot \left(X \cdot p_i\right)^k}{k!}, \tag{5.6}$$

with $X = N$ and $k = n_i$ for the first histogram and $X = M$ and $k = m_i$ for the second histogram. The maximum likelihood estimator for each of the parameters p_i is

$$\hat{p}_i = \frac{n_i + m_i}{N + M}, \tag{5.7}$$

if the hypothesis of identity is valid. Using this estimator, the variable

$$X^2 = \sum_{i=1}^{r} \frac{\left(n_i - N \cdot \hat{p}_i\right)^2}{N \cdot \hat{p}_i} + \sum_{i=1}^{r} \frac{\left(m_i - M \cdot \hat{p}_i\right)^2}{M \cdot \hat{p}_i} = \frac{1}{N \cdot M} \sum_{i=1}^{r} \frac{\left(M \cdot n_i - N \cdot m_i\right)^2}{n_i + m_i} \tag{5.8}$$

has approximately a $\chi^2_{(r-1)}$ distribution [77]. Since the histograms used in the fit are produced by using Monte-Carlo events, the χ^2-test has to take the weights of the events

into account [78]. The weights of the i-th bin $w_{1,i}$ and $w_{2,i}$, where 1 labels the first histogram and 2 the second one, are random variables with an approximated normal probability distribution $N\left(W_1 \cdot p_i, \sigma^2_{1,i}\right)$ and $N\left(W_2 \cdot p_i, \sigma^2_{2,i}\right)$, respectively, with $W_1 = \sum_{i=1}^{r} w_{1,i}$ the total weight of the first histogram and $W_2 = \sum_{i=1}^{r} w_{2,i}$ the total weight of the second one. $\sigma^2_{k,i}$ with $k = 1, 2$ is the corresponding variance. Using the estimators of the variance of each histogram $s^2_{1,i}$ and $s^2_{2,i}$, the maximum likelihood estimator $\hat{p}_i$ can be written as

$$\hat{p}_i = \frac{w_{1,i} \cdot W_1/s^2_{1,i} + w_{2,i} \cdot W_2/s^2_{2,i}}{W_1/s^2_{1,i} + W_2/s^2_{2,i}}. \tag{5.9}$$

The corresponding X^2 variable is still $\chi^2_{(r-1)}$ distributed and is defined via

$$X^2 = \sum_{i=1}^{r} \frac{\left(w_{1,i} - W_1 \cdot \hat{p}_i\right)^2}{s^2_{1,i}} + \sum_{i=1}^{r} \frac{\left(w_{2,i} - W_2 \cdot \hat{p}_i\right)^2}{s^2_{2,i}} = \sum_{i=1}^{r} \frac{\left(W_1 \cdot w_{2,i} - W_2 \cdot w_{1,i}\right)^2}{W_1^2 \cdot s^2_{2,i} + W_2^2 \cdot s^2_{1,i}}. \tag{5.10}$$

This χ^2-test was performed several times comparing the correlation plot of both light quarks with correlation plots of the light quark and the Ghost Jets using values A_η from 1.0 to 1.9 in 0.1 steps to calculate the pseudorapidity of the Ghost Jet. The minimum of a quadratic fit applied to the χ^2/NDF values gives the best estimation of the parameter in Equation 5.2. Figure 5.2 shows the results of the χ^2-tests as well as the quadratic function, which is fitted to the results. The quadratic fit leads to the following value of the parameter A_η:

$$A_\eta = 1.553 \pm 0.129 \tag{5.11}$$

To compare the reconstruction of Ghost Jet's pseudorapidity, Figure 5.3 shows the correlation plots of both light quark as well as the correlation plot of the light quarks and the Ghost Jet. The distribution shown in Figure 5.3 b) follows the shape of the correlation of both light quarks. It contains the most likely values as expected.

5.2.2 Ghost Jet transverse Momentum

The transverse momentum of the Ghost Jet $p_{T,GJ}$ is calculated by using only information about the light jet's transverse momentum $p_{T,jet}$. Due to the complex structure compared to the other kinematic variables, two different models are tested to fit the distribution of

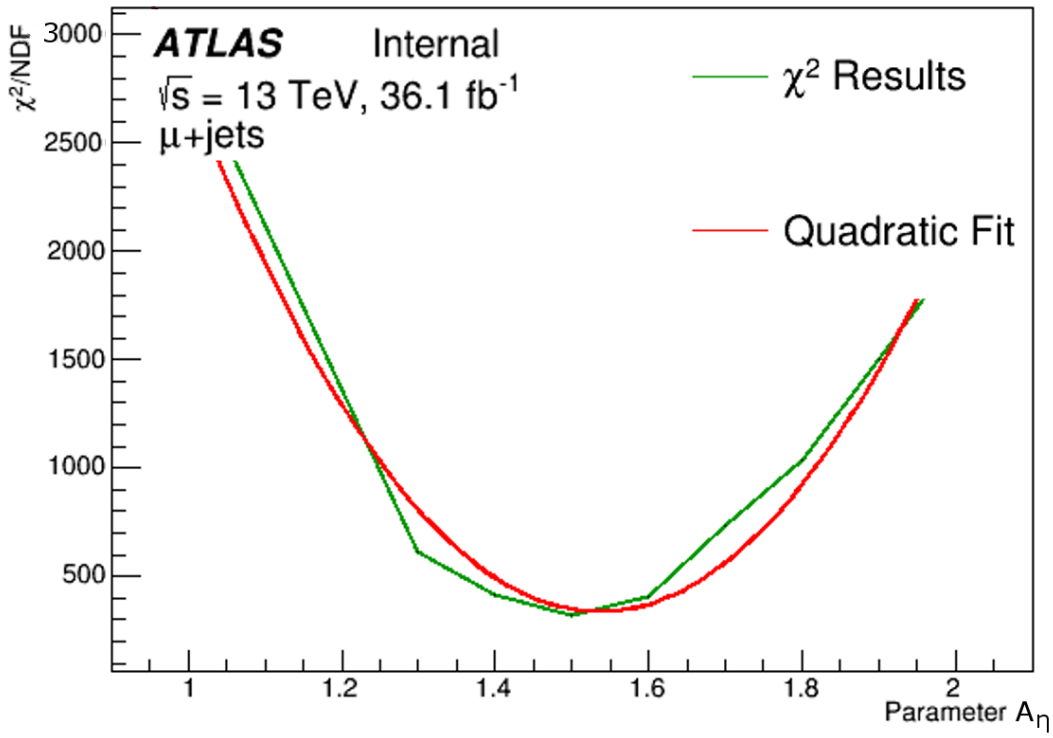

Figure 5.2: The quadratic fit used to estimate the parameter A_η of the Ghost Jet's pseudorapidity calculation. Due to a low number of events in $t\bar{t}Z$ Monte-Carlo samples, $t\bar{t}$ events are used in this fit.

the transverse momentum. The first model contains a polynomial function of the n-th order

$$p_{T,GJ} = \sum_{i=0}^{n} p_i \cdot p_{T,jet}^{i}, \tag{5.12}$$

where the p_is are the different fit parameters. The parameter n depends on the quality of the fit as well as on the order of magnitude of the parameters p_i. The second model includes an exponential function

$$p_{T,GJ} = A_{p_T} \cdot \exp\left(-B_{p_T} \cdot (p_{T,jet} - C_{p_T})\right) + D_{p_T}, \tag{5.13}$$

where A_{p_T}, B_{p_T}, C_{p_T} and D_{p_T} are the fit parameters.

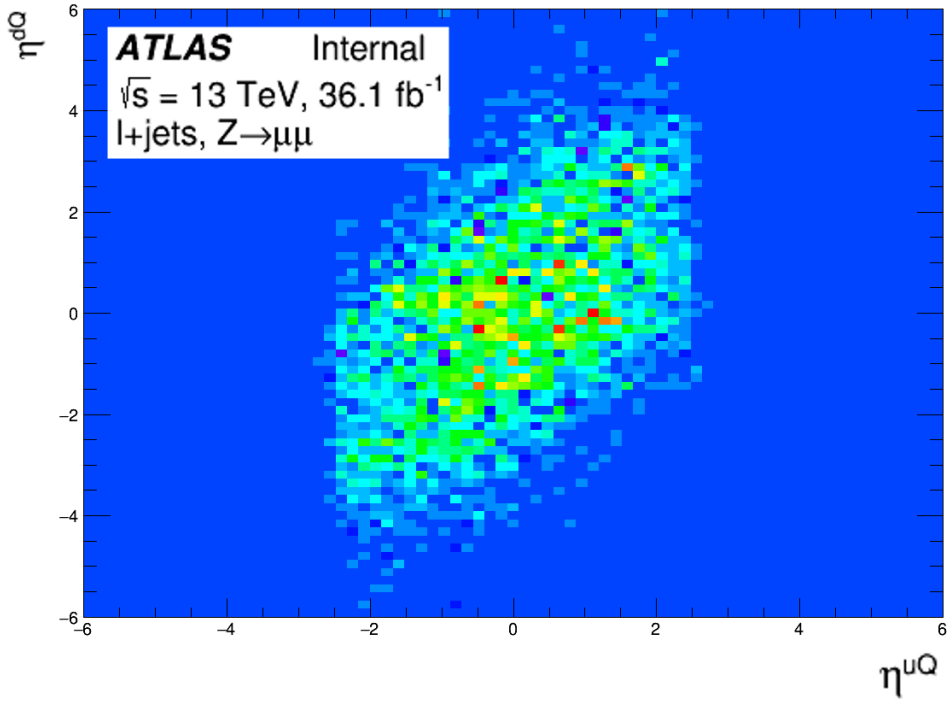

(a)

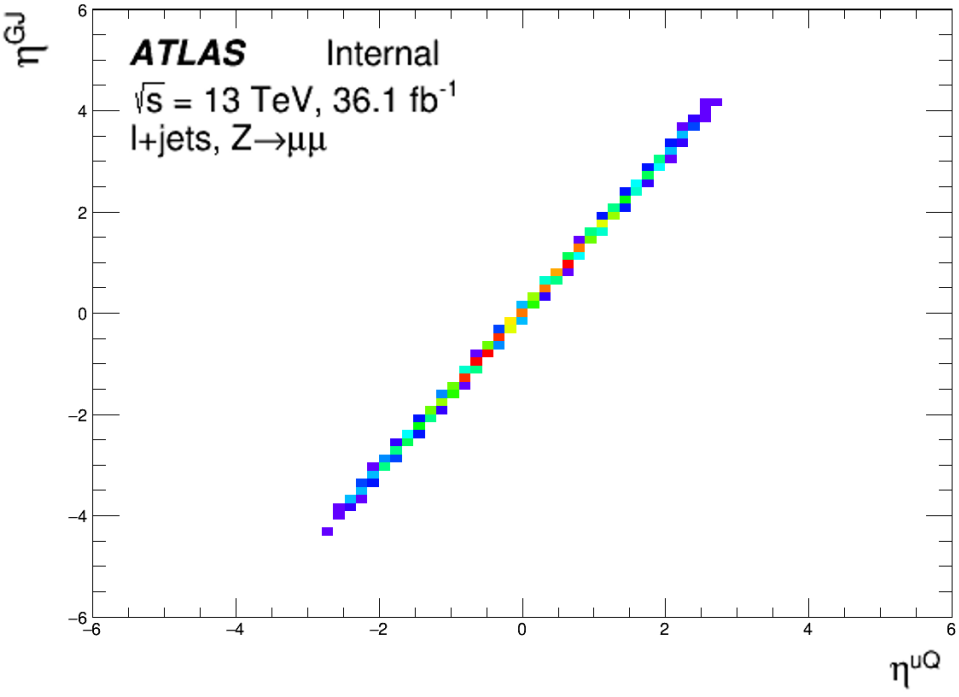

(b)

Figure 5.3: The pseudorapidity correlation plots of a) both light quarks and of the Ghost Jet and b) the present up-type quark quark in events, where the jet of the light down-type quark is missing.

Parameter	p_0 [GeV]	p_1	$p_2 \left[10^{-3}\ \text{GeV}^{-1}\right]$	$p_3 \left[10^{-6}\ \text{GeV}^{-2}\right]$
Value	40.753 ± 0.330	-0.394 ± 0.013	2.209 ± 0.161	-3.410 ± 0.618

Table 5.4: The parameters of the polynomial fit. Due to the extremely small parameters for higher orders and the behaviour of the function for a higher transverse momentum of the light quark, the parameter n is set to 3.

Parameter	A_{p_T} [GeV]	$B_{p_T} \left[\ \text{GeV}^{-1}\right]$	C_{p_T} [GeV]	D_{p_T} [GeV]
Value	22.079 ± 0.443	0.021 ± 0.001	11.443 ± 0.949	16.257 ± 0.069

Table 5.5: The parameters of the exponential fit.

To extract the information about the correlation between the transverse momenta of both light quarks, the profile of the correlation distribution is used, which reduces a two-dimensional histogram to a one-dimensional histogram containing the average transverse momentum of the light down-type quark for each p_T bin of the light up-type quark. The profile allows a simple fit of a function to a one-dimensional distribution. The fit results of the polynomial model are shown in Table 5.4 and the parameters of the exponential fit are shown in Table 5.5, respectively.

As shown in the table above, the parameters of the polynomial fit gets very small for higher order corrections. Due to this fact as well as the behaviour of the fitted function for a higher transverse momentum of the light quark, the parameter n is set to 3. The parameters would get too small for higher orders and the function would not describe the distribution well enough for lower orders. Nevertheless, the polynomial model would cause a very low and even negative Ghost Jet transverse momentum for a very high light jet p_T. Consequently, the polynomial model is excluded and the Ghost Jet transverse momentum is calculated via an exponential function using the parameters in Table 5.5. Figure 5.4 shows the profile of the correlation plot of both light quark as well as the fitted exponential function, which is in good agreement with the plot.

A closer look on the transverse momentum of the Ghost Jet is given by Figure 5.5, which shows the Ghost Jet p_T distribution for events with three jets. Unlike usual transverse momentum distributions, the distribution of the Ghost Jet's transverse momentum is flat, which is caused by the fitted function and the distribution of the light jet shown in Figure 5.6. The distribution of the light jet's transverse momentum follows an exponential-like function, which approximately leads to the same number of events in the bins of the Ghost Jet's transverse momentum distribution. Despite this flat distribution, the Ghost Jet is able to support the fit process of the KLFitter framework.

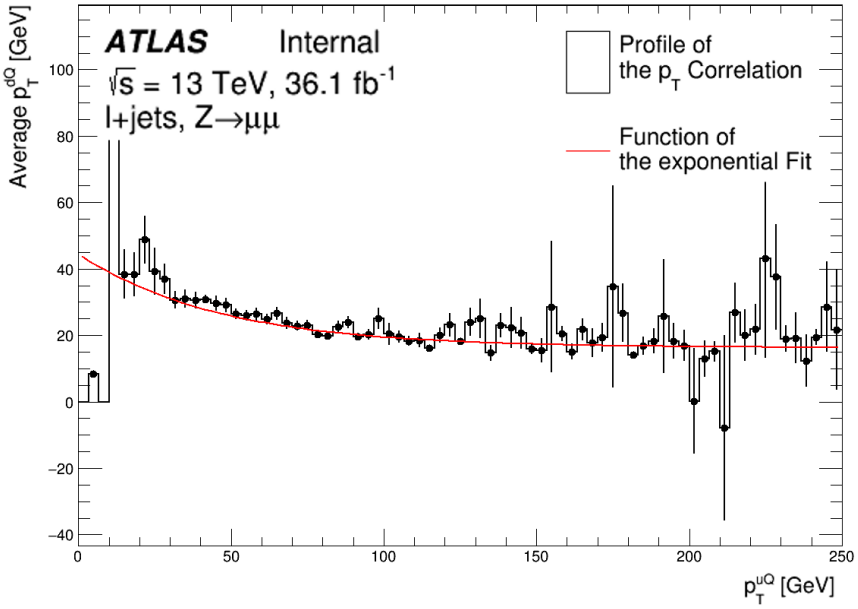

Figure 5.4: A comparison between the exponential function, which is used to calculate the transverse momentum of the Ghost Jet, and the profile of the correlation plot of both light quarks. The function shows good agreement with the plot.

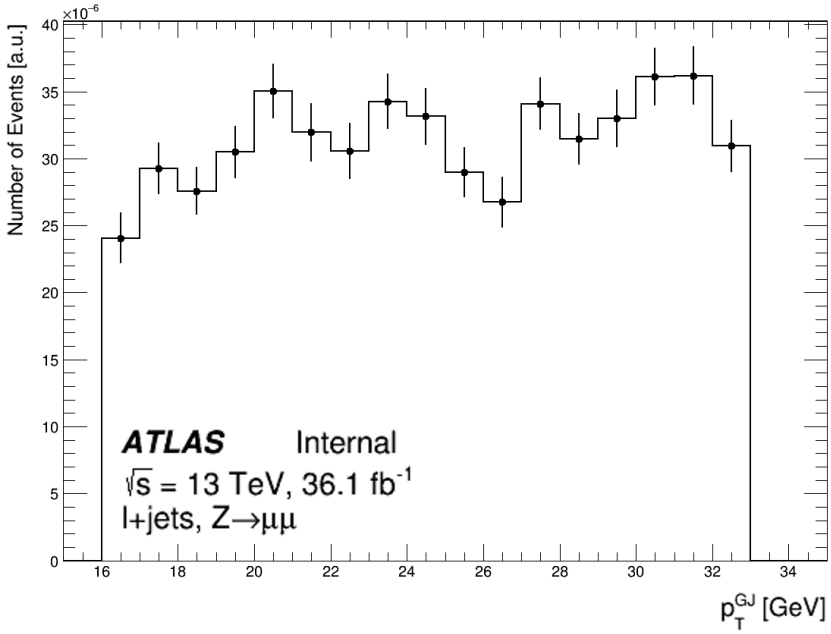

Figure 5.5: The transverse momentum distribution of the Ghost Jet for events with three jets.

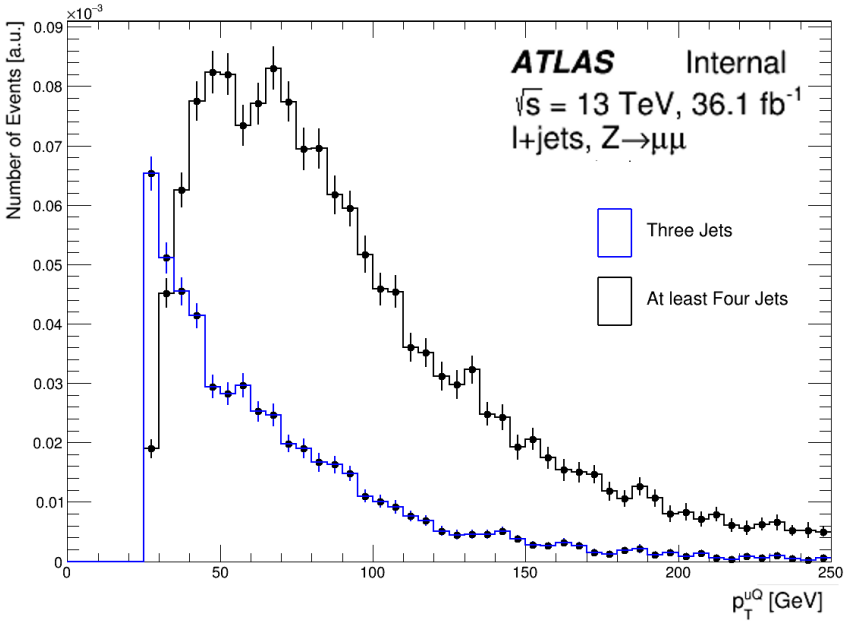

Figure 5.6: The distribution of the transverse momentum of the light jet for events with three jets and events with at least four jets, respectively.

To compare the reconstruction of Ghost Jet's transverse momentum, Figure 5.7 shows the correlation plots of both light quarks as well as the correlation plot of the light quark and the Ghost Jet. The distribution shown in Figure 5.7 b) follows the shape of the correlation of both light quarks. It contains the most likely values as expected.

5.2.3 Ghost Jet azimuthal Angle

The azimuthal angle of the Ghost Jet ϕ_{GJ} is calculated by using all information about the kinematic variables of the light jet as well as the Ghost Jet's pseudorapidity and the Ghost Jet's transverse momentum. Due to the structure of the azimuthal angle correlation, the distribution of the down-type quark's azimuthal angle contains two maxima for each ϕ_{uQ} bin. This makes a fit, which follows the shape of most likely values, impossible. Instead, the invariant mass constraint of both quarks is used for the calculation of the Ghost Jet's azimuthal angle. Since both light quarks originate from the W boson, the invariant mass of the quark system has to equal the mass of the W boson. To calculate the azimuthal angle of the Ghost Jet, the four-momentum of the light jet as well as the four-momentum of the Ghost Jet with $\phi_{GJ} = \phi_{jet} + \Delta\phi$ and $\phi_{GJ} = \phi_{jet} - \Delta\phi$, respectively, are calculated. They are labelled as q_{jet} as well as q^{+}_{GJ} and q^{-}_{GJ} depending on the sign in the calculation. $\Delta\phi$ is the maximum of the distribution shown in Figure 5.8. The maximum of the distribution

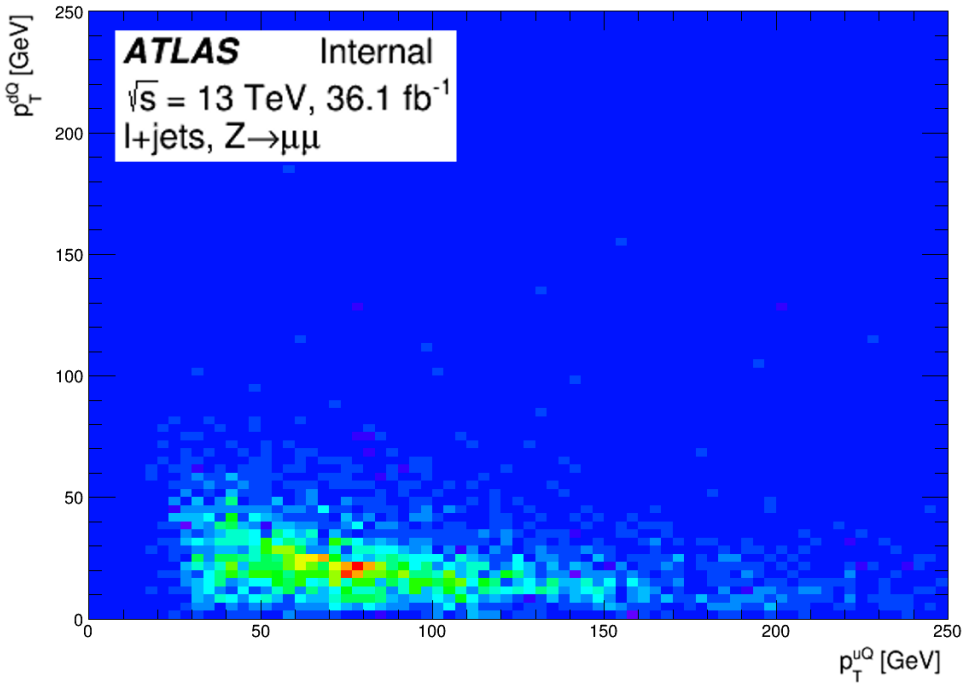

(a)

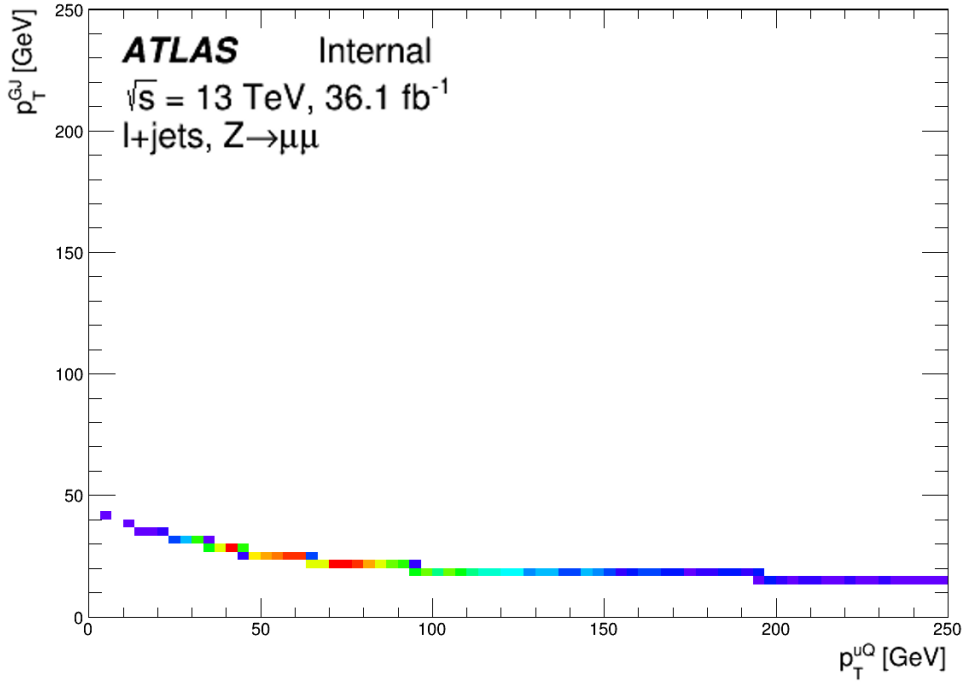

(b)

Figure 5.7: The transverse momentum correlation plots of a) both light quarks and of the Ghost Jet and b) the present up-type quark quark in events, where the jet of the light down-type quark is missing.

is the parameter of the calculation of the Ghost Jet's azimuthal angle with the following value:

$$\Delta\phi = 2.51 \pm 0.50 \tag{5.14}$$

The invariant mass of the $q_{jet} - q^{+}_{GJ}$ and the $q_{jet} - q^{-}_{GJ}$ system is calculated, where the system with an invariant mass closer to the W mass sets the sign of the azimuthal angle calculation. Equation 5.15 summarises the calculation rule of the Ghost Jet's azimuthal angle.

$$\phi_{GJ} = \begin{cases} \phi_{jet} + \Delta\phi, & \text{if } \left|m_{q_{jet}q^{+}_{GJ}} - m_W\right| < \left|m_{q_{jet}q^{-}_{GJ}} - m_W\right| \\ \phi_{jet} - \Delta\phi, & \text{else} \end{cases} \tag{5.15}$$

Due to the low number of selected $t\bar{t}Z$ events, which are used to check the behaviour of the reconstructed kinematic variable, a final comparison between the correlation of both quarks and the correlation of the Ghost Jet and the light quark is not possible, since the structure of the correlation is not visible with that number of events.

5.3 Performance of the modified Likelihood

After the construction of the modified likelihood functions and the description of the calculation of the kinematic Ghost Jet variables, the evaluation of the KLFitter performance using this modified likelihood functions is important to complete this analysis. This section discusses different topics, which are used to evaluate the performance of the modified likelihood functions. Like in the current $t\bar{t}Z$ analysis described in Chapter 3, Section 5.3.1 presents a comparison between the reconstruction of data and Monte Carlo events to determine the behaviour of the modified likelihood functions on data samples. The possible separation power of different variables used in the kinematic fit of the KLFitter framework is discussed in Section 5.3.2, which is important if the likelihood functions are supposed to be used in multivariate analyses. Section 5.3.3 describes the different reconstruction and matching efficiencies of the KLFitter framework using the modified likelihood functions.

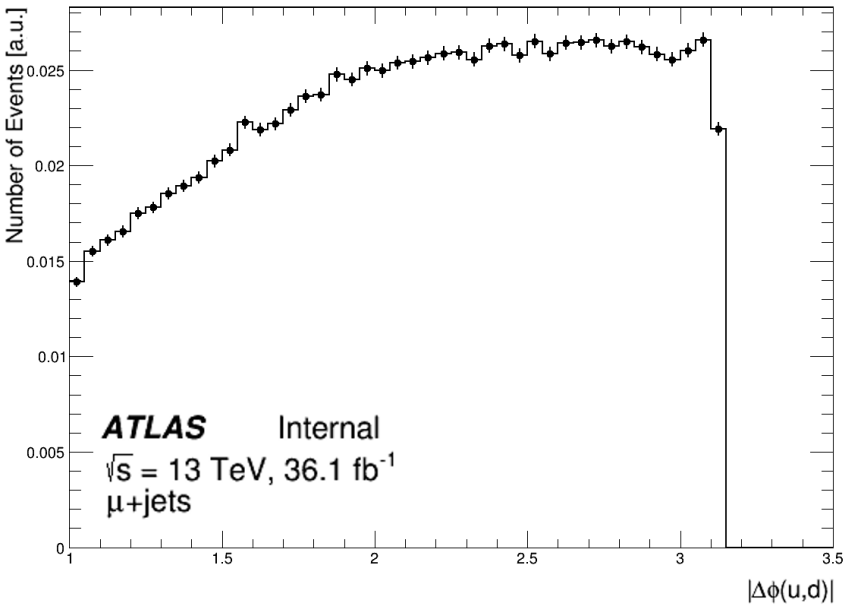

Figure 5.8: The distribution of the absolute value of the difference in the azimuthal angle between both light quarks. Due to a low number of events using $t\bar{t}Z$ samples, $t\bar{t}$ events are used to estimate the maximum of this distribution.

5.3.1 Comparison between Data and Monte Carlo

To check the performance of the modified likelihood functions in an analysis using real data, the reconstruction of Monte Carlo events is compared to the reconstruction of data corresponding to an integrated luminosity of 36.1 fb^{-1} [79]. Figure 5.9 shows the comparison of the number of electrons and the transverse momentum of all three leptons in the WZ control region between data and Monte Carlo events with a KLFitter output. The data is in good agreement with the prediction of the Monte Carlo events, which leads to the result that the modified likelihood is able to reconstruct events using data samples with the right behaviour. Furthermore, the logarithmic likelihood output (logLikelihood) shown in Figure 5.9(a) is shifted to lower values, due to the modifications of the likelihood functions. The kinematic variables of the Ghost Jet presented in Section 5.2, which are used in the fit to reconstruct the mother particles, are based on approximations, which are supposed to follow the distribution of the most likely values in the correlation between both light quarks. Due to the usage of the Ghost Jet in the reconstruction, the resulting distributions of the mother particles' invariant mass are slightly shifted to lower values. This shift leads to a lower logLikelihood values for the modified likelihood functions, which has to be taken into account in analyses, where a cut on the logLikelihood is set.

	Yields (Analysis)	Yields (modified LH)
3ℓ-WZ-CR	5.70/211.8/12.93/213	4.4/165.1/11.2/170
3ℓ-Z-2b3j	17.73/3.32/0.80	15.1/2.8/0.8
3ℓ-Z-1b4j	31.36/18.11/1.91	27.6/14.8/1.8
3ℓ-Z-2b4j	58.28/7.05/0.66	49.1/ 5.0/0.6
3ℓ-noZ-2b	13.29/1.05/0.36	11.1/0.8/0.3

Table 5.6: The event yields of the current $t\bar{t}Z$ analysis [79] as well as the event yields produced by using the modified likelihood functions. Each column shows the yields of the $t\bar{t}Z$, $\ell\ell\ell\nu$, $\ell\ell\nu\nu$ and data reconstruction in this order. Data yields are only available for the control region.

Region	Events with KLFitter Output	Events without KLFitter Output
Fraction [%]	83.14	16.86

Table 5.7: The fraction of events with and without a KLFitter Output.

Furthermore, the event yields in the different regions of the current analysis described in Chapter 3 are of interest, which corresponds to the total number of reconstructed events. A comparison between the yields of the ongoing $t\bar{t}Z$ analysis and the yields produced by the modified likelihood functions exposes possible problems of the fit performance during the run of the reconstruction framework. Table 5.6 shows the different event yields for the signal and the WZ control region of the current $t\bar{t}Z$ analysis as well as the yields produced by using the modified likelihood functions.

The differences between the yields indicates issues during the kinematic fit, since the modified likelihood functions do not produce the same number of reconstructed events. To check this assumption, the number of events are counted, which do not have a KLFitter output, thus, have issues during the kinematic fit. About 16.86 % of all events are not reconstructed by the modified likelihood functions, which is shown in Table 5.7. Despite this loss of events, the modified likelihood functions can still be used for events reconstruction, since the fraction of lost events is relatively small. Nevertheless, it is important to know the reason, which prevents the reconstruction of those events.

For this purpose, the KLFitter framework provides four different warning/error messages, which are stored in the output of the framework:

Error Message	Fraction [%]
1.	99,97
2.	0.00
3.	0.00
4.	0.03

Table 5.8: The fraction of different warning/error messages of events without fit results in the output of the KLFitter framework

1. **MinuitDidNotConverge:** Minuit fit did not converge
2. **FitAbortedDueToNan:** The fit was aborted due to a not-a-number value during the fit
3. **AtLeastOneFitParameterAtItsLimit:** The fit converged, but at least one parameter is at its allowed limit
4. **InvalidTransferFunctionAtConvergence:** Invalid use of the transfer functions at the convergence point

Table 5.8 shows the fraction of the different warning/error messages of events without fit results. The fit of those events does not converge as expected, since the modified likelihood functions presented in Section 5.1.2 have weaker constraints than the version for events with at least four jets, due to the removal of the transfer function of the missing jet as well as the replacement of the missing jet with the Ghost Jet.

5.3.2 Separation Power

A systematic event reconstruction method like the KLFitter framework contains different variables, which can be used to quantify the performance of the reconstruction. One of those variables, which are provided by the framework, is the likelihood output of the fit. If the likelihood output follows a different distribution for background events compared to signal events, this variable can be used as a separation variable in other analyses. To determine the separation power of the likelihood output, the modified likelihood functions are applied to both $t\bar{t}Z$ events representing the signal and to diboson events representing the background including 4ℓ, $\ell\ell\ell\nu$ and $\ell\ell\nu\nu$ production, which fake the $t\bar{t}Z$ final states with additional jet radiation and misidentification. Figure 5.10 visualises the separation power of the logLikelihood variable in the different signal regions and the WZ control region. The modified likelihood functions were applied to both the signal and the background using the *WorkingPoint* method for jet assignment at a working point of $\varepsilon_b = 0.77$. The

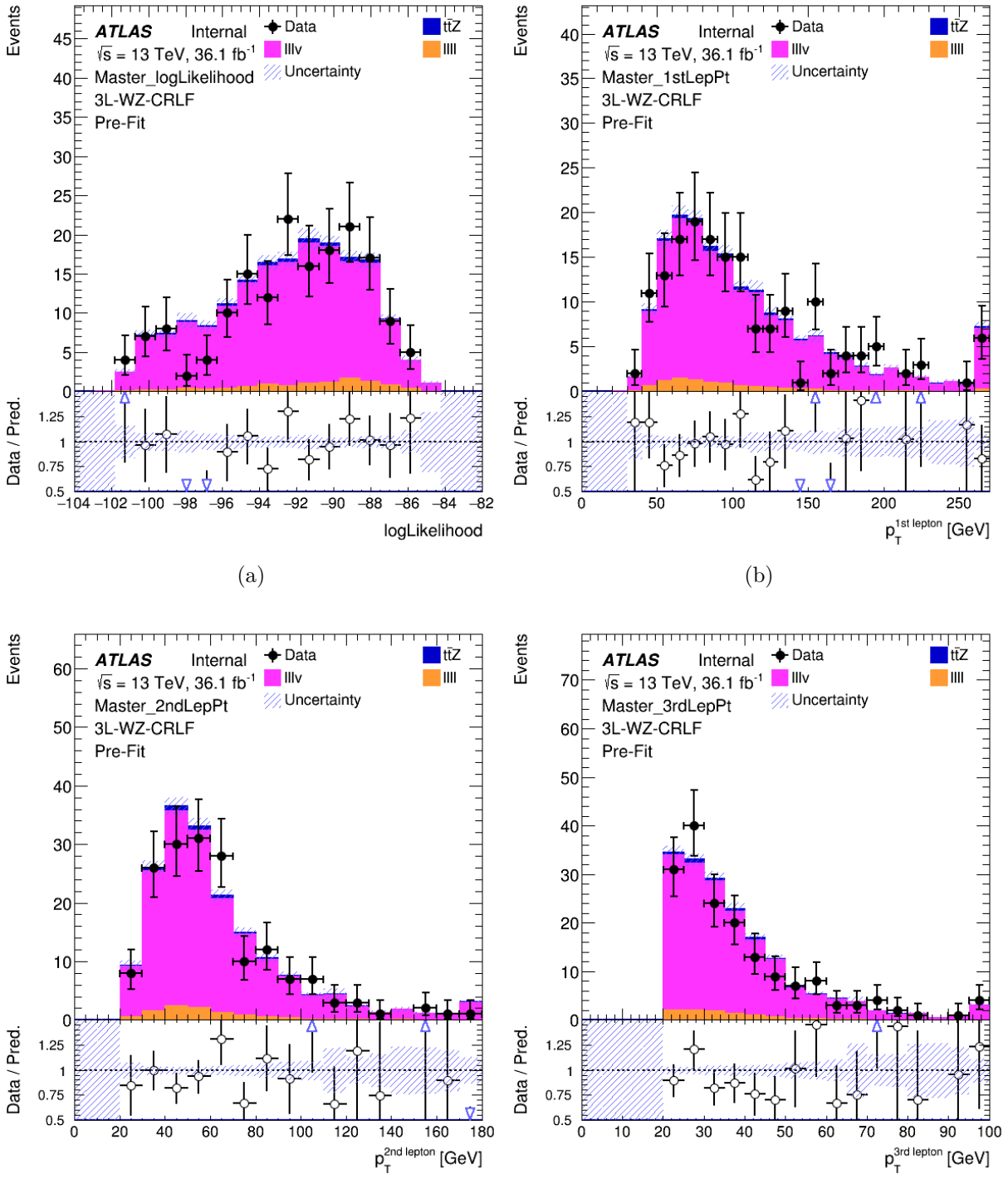

Figure 5.9: The comparison of a) the number of electrons, b) the transverse momentum of the leading-p_T lepton, c) the transverse momentum of the second leading-p_T lepton and d) the transverse momentum of the third leading-p_T lepton in the WZ control region between data and Monte Carlo events with a KLFitter output.

logarithmic likelihood value does not show any separation in the different regions, thus, the variable is not directly suitable to distinguish between signal and background events. Since the kinematic variables of the Ghost Jet are introduced with the modification of the likelihood functions, which are used in the $t\bar{t}Z$ analysis, the separation power of these variables also have to be checked. This analysis includes the pseudorapidity, the transverse momentum and the energy of the Ghost Jet.

Like the logarithmic likelihood values, the kinematic variables of the Ghost, which are shown in Figure 5.11, 5.12 and 5.13, do not contain any separation power to distinguish signal and background events. A possibility to improve the separation power of the variables is described in the following section.

5.3.3 Reconstruction and Matching Efficiencies

This section discusses the different reconstruction and matching efficiencies of the modified likelihood functions. For this purpose, the KLFitter framework is applied to simulated $t\bar{t}Z$ events using the modified likelihood functions as well as the *WorkingPoint* option for jet assignment. The different efficiencies are determined by counting the events, where a certain particle is labelled as matched by the used C++ class described in Section 4.3.2.

Figure 5.14 shows the different reconstruction efficiencies of the particles in the $t\bar{t}Z$ production. Compared with the efficiencies of the original likelihood functions for events with at least four jets, the modification of the likelihood functions lower the reconstruction efficiencies significantly. This is a result of using the kinematic variables of the Ghost Jet in the reconstruction of the mother particles, which follow the distribution of the most likely values within the correlation plot of both light quarks described in Section 5.2. This leads to valid overall kinematic distributions but also to differences between the Ghost Jet's and the missing jet's kinematic variables in individual events, where the differences gain more significance the further the values are away from the distribution of the most likely values. As a result, the reconstructed mother particles do not fulfil the expected ΔR criterion, which leads to a lower reconstruction efficiency even in events with the right assignment of the detector objects to the particles on parton level.

Despite this behaviour of the reconstructed mother particles, the performance of the modified likelihood functions shows excellent efficiencies in terms of jet assignment. Figure 5.15 shows the matching matrix, where the entries correspond to the fraction of events, where a jet matches a certain quark. The large diagonal entries correspond to a large number of events, where the jets are assigned to the correct parton. Compared to the original likelihood functions, the efficiencies of right matchings are distinctly improved.

To use the Ghost Jet directly in the reconstruction of mother particles, the calculation

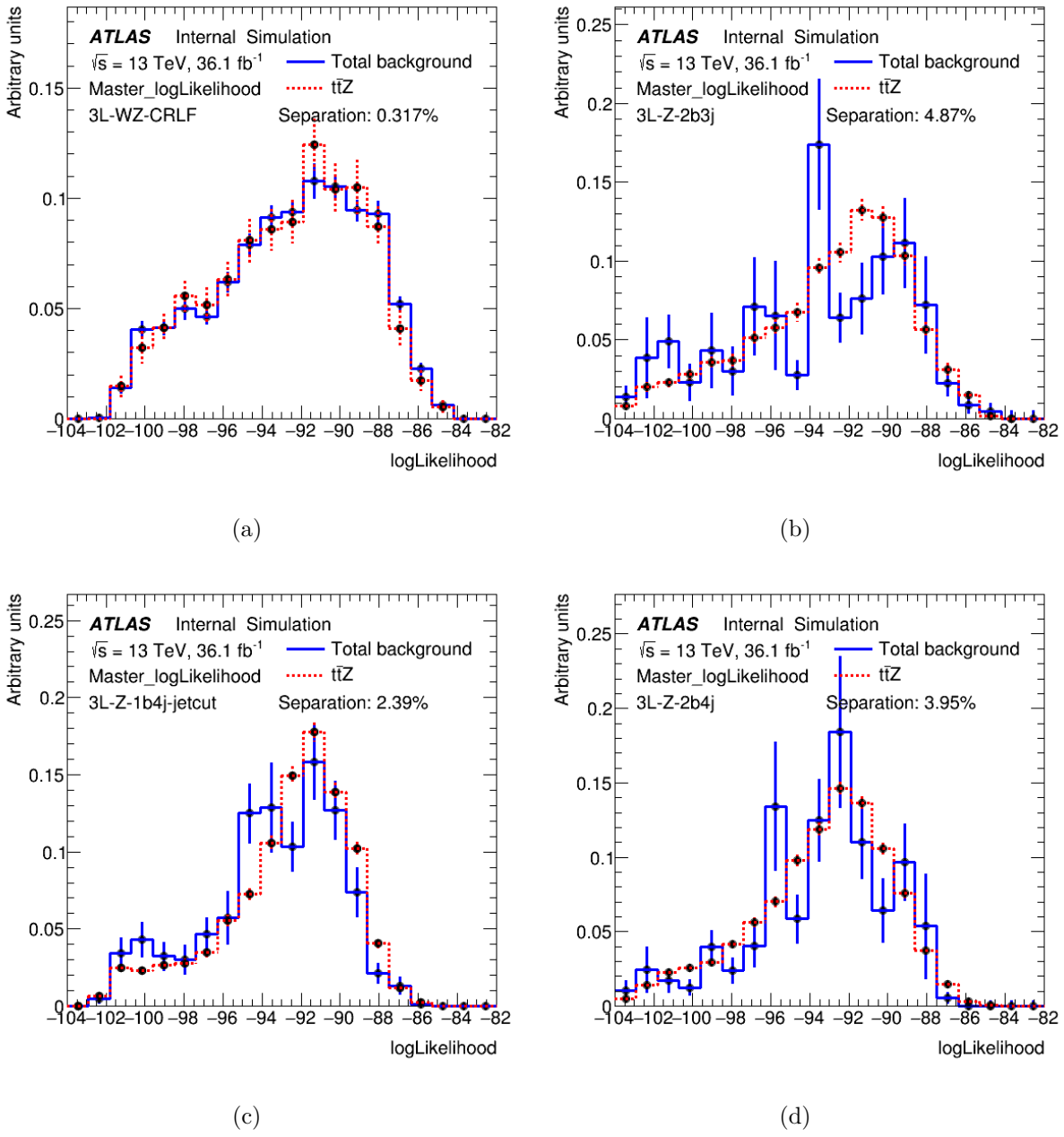

Figure 5.10: The visualisation of the separation power of the logarithmic likelihood value in the different signal regions and the WZ control region of the current $t\bar{t}Z$ analysis using $t\bar{t}Z$ final states as signal events and diboson production with 4ℓ, $\ell\ell\ell\nu$ and $\ell\ell\nu\nu$ in the final state as the corresponding background.

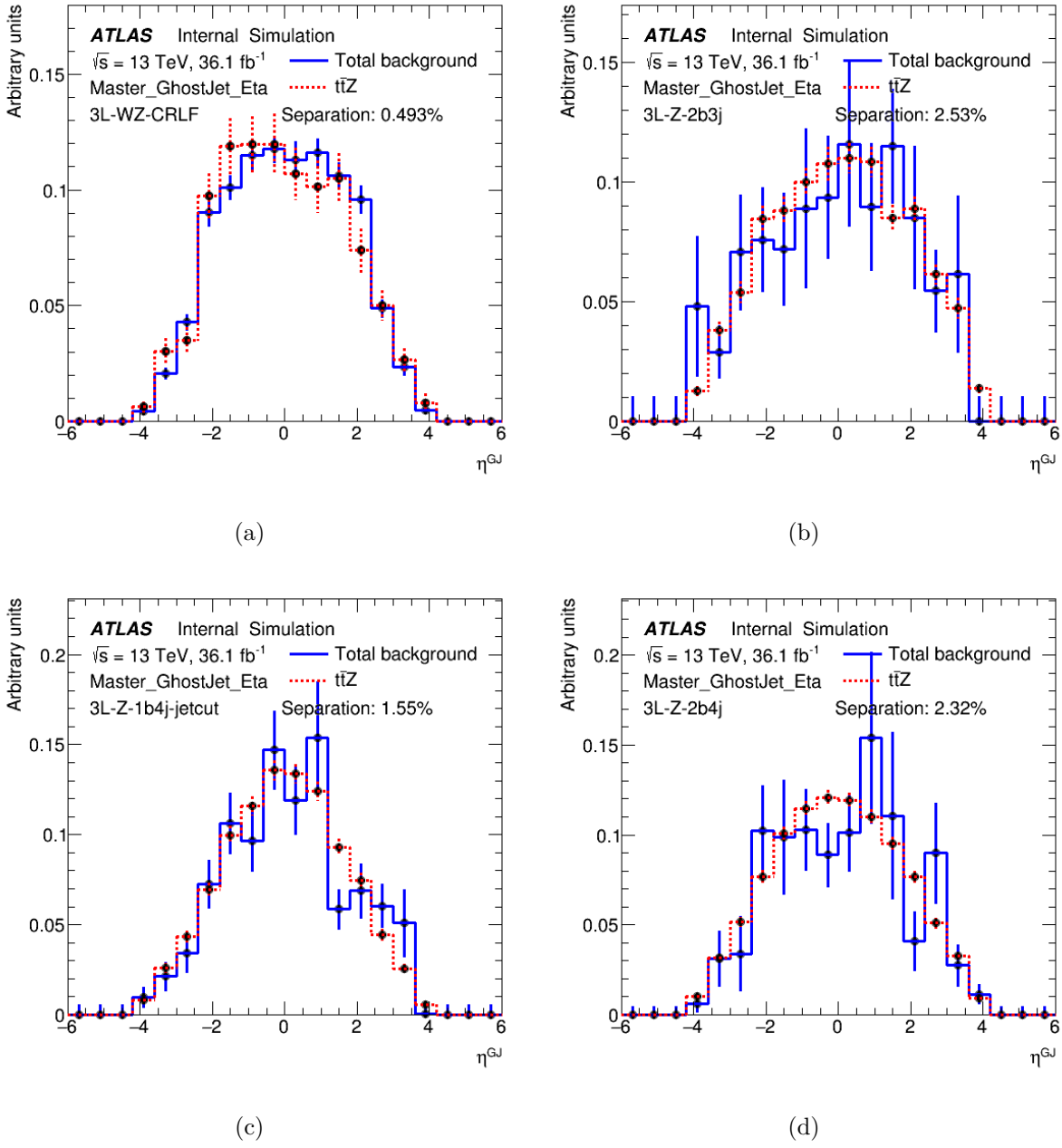

Figure 5.11: The visualisation of the separation power of the Ghost Jet's pseudorapidity in the different signal regions and the WZ control region of the current $t\bar{t}Z$ analysis using $t\bar{t}Z$ final states as signal events and diboson production with 4ℓ, $\ell\ell\ell\nu$ and $\ell\ell\nu\nu$ in the final state as the corresponding background.

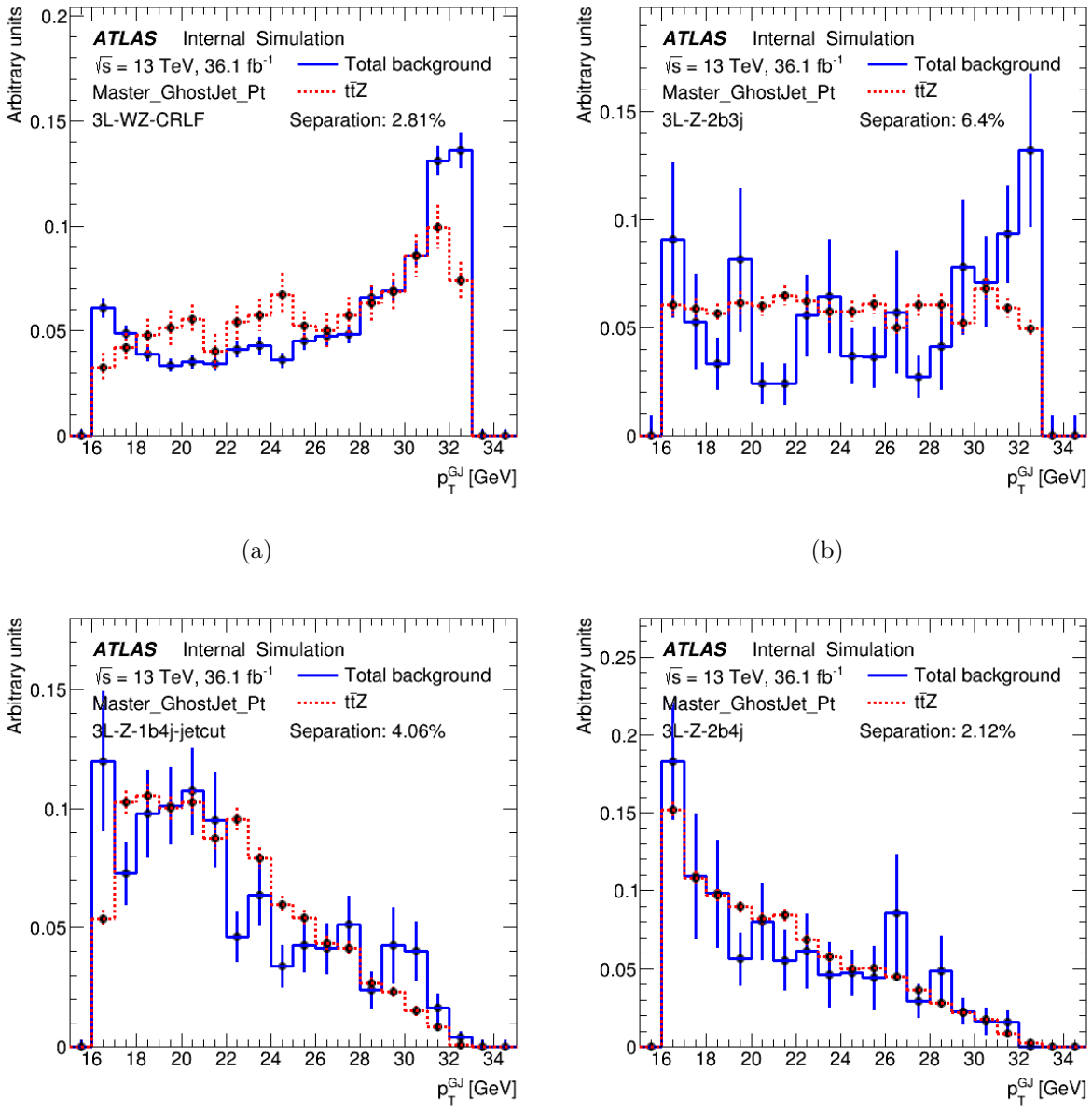

(a) (b)

(c) (d)

Figure 5.12: The visualisation of the separation power of the Ghost Jet's transverse momentum in the different signal regions and the WZ control region of the current $t\bar{t}Z$ analysis using $t\bar{t}Z$ final states as signal events and diboson production with 4ℓ, $\ell\ell\ell\nu$ and $\ell\ell\nu\nu$ in the final state as the corresponding background.

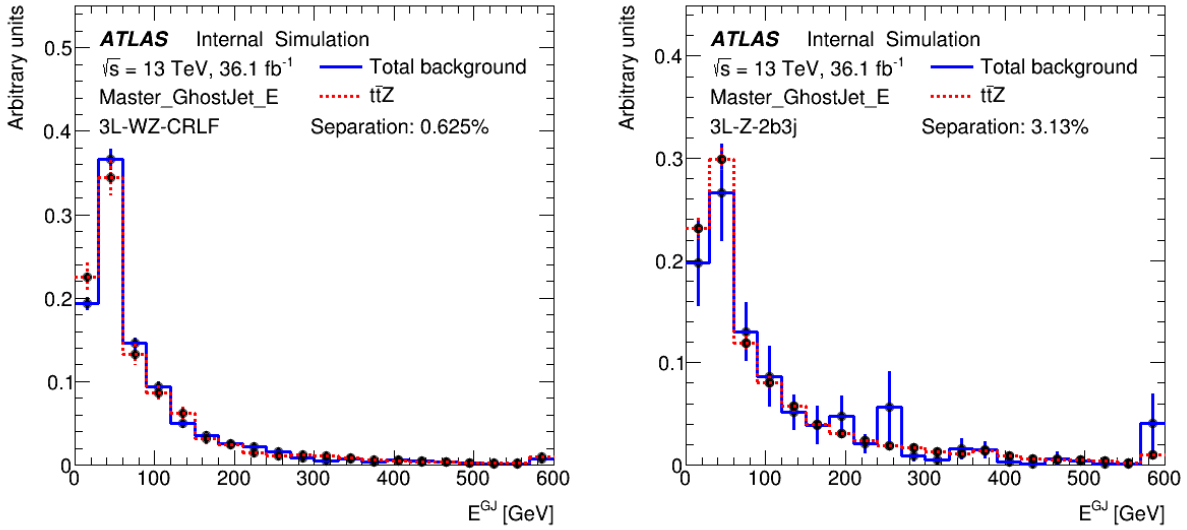

(a)

(b)

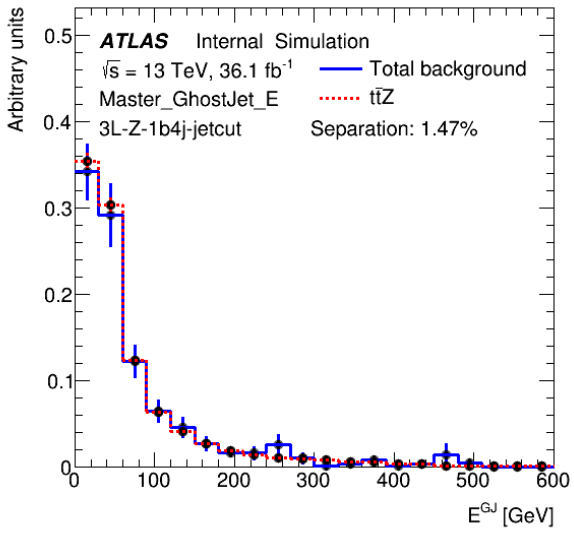

(c)

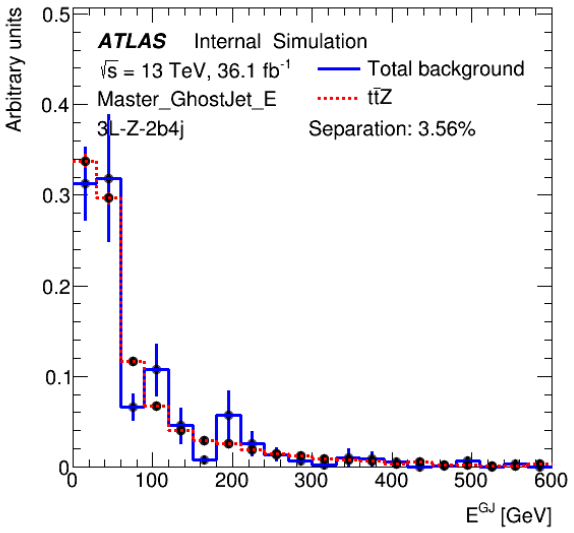

(d)

Figure 5.13: The visualisation of the separation power of the Ghost Jet's energy in the different signal regions and the WZ control region of the current $t\bar{t}Z$ analysis using $t\bar{t}Z$ final states as signal events and diboson production with 4ℓ, $\ell\ell\ell\nu$ and $\ell\ell\nu\nu$ in the final state as the corresponding background.

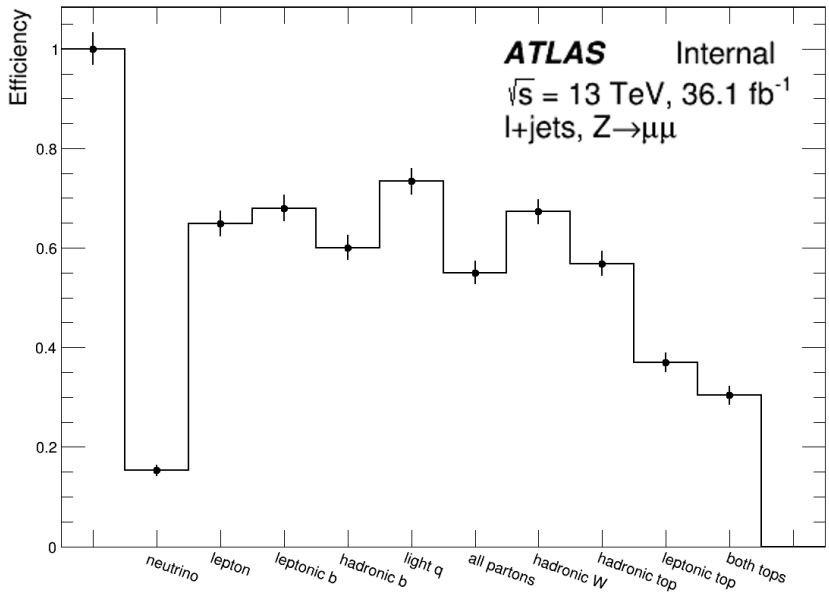

Figure 5.14: The reconstruction efficiencies of the different particles, which are part of the $t\bar{t}Z$ production, normalised to the total number of events.

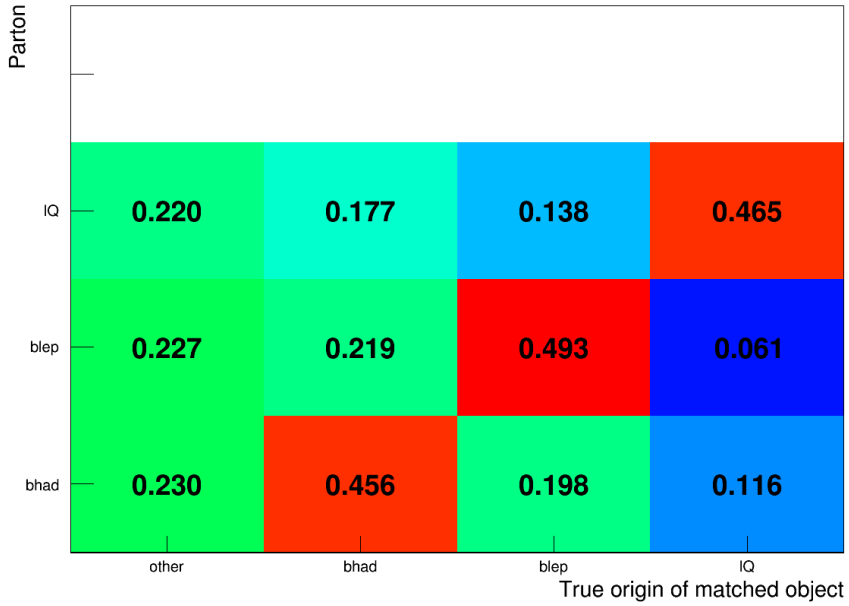

Figure 5.15: The matching matrix containing the fraction of the different matching possibilities between the jets and the partons in $t\bar{t}Z$ events with three jets. The entries are normalised row-by-row. 'Other' labels jets, which do not originate from one of the quarks in the $t\bar{t}Z$ final state.

methods of the Ghost Jet's kinematic variables have to be extended. The correlation plots contain complete kinematic distributions of the missing jet for each bin of the present light jet. New model functions, which describe the distributions in the different bins of the present light jet, would decrease the deviations in individual events, due to a much better Ghost Jet reconstruction, since the whole distributions and not only the most likely values are used for the Ghost Jet calculations. Using parameters, which depend on the kinematic variables of the present light jet, these new model functions can be included into the kinematic fit as new constraints. Due to the common origin of both light quarks, differences in the reconstruction including Ghost Jets calculated from different jets are expected using this new model functions. Furthermore, differences of the kinematic variables between the present light jet of $t\bar{t}Z$ events and a jet of background events are also expected, which leads to a possible higher separation power of signal and background events.

6 Summary and Outlook

In the past decades, several high energy physics experiments have tested the prediction of the Standard Model of particle physics. One of its most interesting parts is the physics of the top quark. Due to its large Yukawa coupling close to unity, it is expected to play a special role within the Standard Model. Precise measurements of the top quark's quantities, particularly of the third component of its weak isospin, are of great interest. The Standard Model assumes the top quark to be the weak isospin partner of the bottom quark but only a direct measurement can confirm this assumption. One possibility to access this quantity is via the coupling of the top quark to the Z boson measured in the $t\bar{t}Z$ production cross section. This cross section depends on the third component of the top quark's weak isospin. However, the precision of the $t\bar{t}Z$ production measurements is dominated by statistical uncertainties. The current analysis of $t\bar{t}Z$ events includes events with at least three jets, but the analysis tool used in this analysis is not able to reconstruct final states of events with exactly three jets. A correct final state reconstruction for instance in terms of assignment between detector objects and particles on parton level is also essential for measurements of the tZ coupling. The fraction of events with three jets is about 42 % of the number of events. Since the KLFitter framework cannot reconstruct those events in the current analysis, a correct final state reconstruction would increase the precision significantly.

This thesis describes a method to modify the likelihood functions used by the KLFitter framework. This allows the reconstruction of the final state of events with three jets and increases the number of events available in the analysis of the tZ coupling. The jet with the highest probability to get lost in an event originates from either the light up-type quark (25.43 %) or the light down-type quark (35.52 %). Due to their common origin, this method uses the correlation between the kinematic variables of both light quarks. Different functions are fitted to the correlation distributions of the kinematic variables of both light quarks. These functions as well as the invariant mass constraint of the light quark system allow the construction of an artificial jet, the Ghost Jet. The artificial jet replaces the missing jet during the kinematic likelihood fit performed by the KLFitter framework to keep the mass constraints of the hadronic mother particles. The Ghost Jet's

p_T reconstruction function and the shape of the distribution of the light jet's transverse momentum lead to a flat distribution of the transverse momentum of the Ghost Jet. Due to the supportive role of the Ghost Jet, this does not prevent the reconstruction of final states. Furthermore, the fits of the different reconstruction functions reduce the different complex kinematic distributions of the missing jet to much simpler ones. They follow the shape of the most likely values, which leads to possible deviations between the kinematic variables of the Ghost Jet and the missing jet in individual events. These deviations become noticeable by using the Ghost Jet in particle reconstructions. The kinematic variables of the reconstructed mother particles slightly differ from the expected ones. This phenomenon is shown by the reconstruction efficiencies of the different particles in the previous chapter, where the mother particles do not fulfil the ΔR criterion to be labelled as matched. The shift of the logLikelihood distribution to lower values is also caused by these deviations, since the invariant mass distribution of the reconstructed mother particles does not exactly match the expected one. Nevertheless, the efficiencies of the correct assignment between the jets and the partons are distinctly improved.

Furthermore, the modified likelihood can be used in the ongoing as well as in the upcoming analyses of the current data taking period, where $80-100$ fb^{-1} are expected. It will help to reduce the statistical uncertainties distinctly. Together with the huge amount of data of the current period, the precision of the measurements will be increased. There is also potential to improve the quality of the Ghost Jet's reconstruction behaviour. This thesis discusses a possibility to extent the calculation methods of the kinematic variables of the Ghost Jet. The kinematic variables of the Ghost Jet can be included into the kinematic fit by using the whole correlation distributions of both light quarks. In this case, the parameters of the functions depend on the kinematic variables of the present light jet. This will lead to better reconstruction results in individual events and thus to better reconstruction efficiencies of the mother particles. The usage of the Ghost Jet method to reconstruct final states of certain events is also not restricted to the $t\bar{t}$ or $t\bar{t}Z$ production. Since this method is based on the correlation between both light quarks of the hadronically decaying W boson, this method can easily be modified to reconstruct the final states of other events. The requirement is a final state based on top quark pair production for instance $t\bar{t}H$. Further studies of the Ghost Jet reconstruction model will give the possibility to increase the precision of several analyses.

Bibliography

[1] Y. Fukuda et al. (Super-Kamiokande Collaboration), *Evidence for Oscillation of Atmospheric Neutrinos*, Phys. Rev. Lett. **81**, 1562 (1998)

[2] F. Abe, et al. (CDF Collaboration), *Observation of Top Quark Production in $p\overline{p}$ Collisions with the Collider Detector at Fermilab*, Phys. Rev. Lett. **74**, 2626 (1995)

[3] S. Abachi, et al. (DØ Collaboration), *Observation of the Top Quark*, Phys. Rev. Lett. **74**, 2632 (1995)

[4] ATLAS Collaboration, *Observation of a new particle in the search for the Standard Model Higgs boson with the ATLAS detector at the LHC*, Phys. Lett. **B 716**, 1 (2012)

[5] CMS Collaboration, *Observation of a new boson at a mass of 125 GeV with the CMS experiment at the LHC*, Phys. Lett. **B 716**, 30 (2012)

[6] P. W. Higgs, *Broken Symmetries, Massless Particles and Gauge Fields*, Phys. Lett. **12**, 132 (1964)

[7] F. Englert, R. Brout, *Broken Symmetry and the Mass of Gauge Vector Mesons*, Phys. Rev. Lett. **13**, 321 (1964)

[8] J. Erdmann, et al., *A likelihood-based reconstruction algorithm for top-quark pairs and KLFitter framework*, Nucl. Instrum. Meth. **A 748**, 18 (2014)

[9] S. L. Glashow, *Partial Symmetries of Weak Interactions*, Nucl. Phys. **22**, 579 (1961)

[10] S. Weinberg, *A Model of Leptons*, Phys. Rev. Lett. **19**, 1264 (1967)

[11] A. Salam, *Weak and Electromagnetic Interactions*, ed. Nobel Symposium No. 8 (Almqvist & Wiksell, Stockholm, 1968)

[12] S. L. Glashow, J. Iliopoulos, L. Maiani, *Weak Interactions with Lepton-Hadron Symmetry*, Phys. Rev. **D 2**, 1285 (1970)

[13] H. Georgi, S. L. Glashow, *Unified Weak and Electromagnetic Interactions without Neutral Currents*, Phys. Rev. Lett. **28**, 1494 (1972)

[14] H. D. Politzer, *Reliable Perturbative Results for Strong Interactions*, Phys. Rev. Lett. **30**, 1346 (1973)

[15] H. D. Politzer, *Asymptotic Freedom: An Approach to Strong Interactions*, Phys. Rept. **14**, 129 (1974)

[16] D. J. Gross, F. Wilczek, *Asymptotically Free Gauge Theories*, Phys. Rev. **D 8**, 3633 (1973)

[17] S. Weinberg, *The Making of the Standard Model*, Eur. Phys. J. **C 34**, 5 (2004)

[18] G. 't Hooft, *Renormalizable Lagrangians For Massive Yang-Mills Fields*, Nucl. Phys. **B 35**, 167 (1971)

[19] G. 't Hooft, M. Veltmann, *Regularization And Renormalization Of Gauge Fields*, Nucl. Phys. **B 44**, 189 (1972)

[20] G. 't Hooft, M. Veltmann, *Combinatorics of gauge fields*, Nucl. Phys. **B 50**, 318 (1972)

[21] D. J. Gross, F. Wilczek, *Ultraviolet Behavior of Non-Abelian Gauge Theories*, Phys. Rev. Lett. **30**, 1343 (1973)

[22] C. S. Wu, et al., *Experimental Test of Parity Conservation in Beta Decay*, Phys. Rev. **105**, 1413 (1957)

[23] N. Cabibbo, *Unitary Symmetry and Leptonic Decays*, Phys. Rev. Lett. **10**, 531 (1963)

[24] M. Kobayashi, T. Maskawa, *CP Violation in the Renormalizable Theory of Weak Interaction*, Prog. Theor. Phys. **49**, 652 (1973)

[25] C. Patrignani et al. Particle Data Group, *Review of Particle Physics*, Chin. Phys. **C 40(10)**, 100001 (2016)

[26] D. Griffiths, *Introduction to Elementary Particles*, Wiley (2008)

[27] V. C. Rubin, N. Thonnard, W. K. Ford Jr., *Rotational properties of 21 SC galaxies with a large range of luminosities and radii, from NGC 4605 R = 4kpc to UGC 2885 R = 122 kpc*, Astrophys. J. **238**, 471 (1980)

[28] H. P. Nilles, *Supersymmetry, supergravity and particle physics*, Phys. Rep. **110**, 1 (1984)

[29] H. E. Haber, G. L. Kane, *The search for supersymmetry: Probing physics beyond the standard model*, Phys. Rep. **117**, 75 (1985)

[30] J. W. Cronin et al., *Evidence for the* 2π *Decay of the* K_2^0 *Meson*, Phys. Rev. Lett. **13**, 138 (1964)

[31] M. I. Perl et al., *Evidence for Anomalous Lepton Production in* $e^+ - e^-$ *Annihilation*, Phys. Rev. Lett. **35**, 1489 (1975)

[32] S. W. Herb, et al., *Observation of a Dimuon Resonance at* 9.5 GeV *in* 400 GeV *Proton-Nucleus Collisions*, Phys. Rev. Lett. **39**, 252 (1977)

[33] G. Gell-Mann, *The interpretation of the new particles as displaced charge multiplets*, Nuovo Cim. **4**, 848 (1980)

[34] T. Nakano, K. Nishijima, *Charge Independence for V-particles*, Prog. Theor. Phys. **10**, 581 (1953)

[35] G. L. Kane, M. E. Peskin, *A Constraint from B Decay on Models with no t Quark*, Nucl. Phys. **B 195**, 29 (1982)

[36] S. L. Glashow, H. Georgi, *Making DØ Without the T Quark*, Nucl. Phys. **B 167**, 173 (1980)

[37] G. L. Kane, A. Pais, *Generalization of Gim: Horizontal and Vertical Flavour Mixing*, Phys. Rev. **D 19**, 2746 (1979)

[38] A. Bean, et al. (CLEO), *Improved Upper Limit on Flavor Changing Neutral-Current Decays of the b Quark*, Phys. Rev. **D 35**, 3533 (1987)

[39] LEP-Electroweak Working Group and the LEP Collaborations: ALEPH, DELPHI, L3 and OPAL, *Electroweak Parameters of the* Z^0 *Resonance and the Standard Model*, Phys. Lett. **B 276**, 247 (1992)

[40] Tevatron Electroweak Working Group, *Combination of CDF and DØ results on the mass of the top quark using* $9.7fb^{-1}$ *at the Tevatron*, arXiv: 1608.01881 (2016)

[41] M. Jeżabek, J. H. Kühn, *QCD Corrections to Semileptonic Decays of Heavy Quarks*, Nucl. Phys. **B 314**, 1 (1989)

[42] The Durham HepData Project, *Online PDF plotting and calculation*, [accessed 14.03.2017] `http://hepdata.cedar.ac.uk/pdf/pdf3.html`

[43] J. C. Collins, D. E. Soper, *The Theorems of Perturbative QCD*, Ann. Rev. Nucl. Part. Sci. **37**, 383 (1987)

[44] ATLAS Collaboration, *Measurement of the $t\bar{t}$ production cross-section using $e\mu$ events with b-tagged jets in pp collisions at $\sqrt{s} = 13$ TeV with the ATLAS detector*, Phys. Lett. **B 761**, 136 (2016)

[45] J. Alwall et al., *The automated computation of tree-level and next-to-leading order differential cross sections, and their matching of parton shower simulations*, JHEP **079**, 1407 (2014)

[46] ATLAS Collaboration, *Measurement of the $t\bar{t}Z$ and $t\bar{t}W$ production cross section in multilepton final states using 3.2 fb^{-1} of pp collisions at $\sqrt{s} = 13$ TeV with the ATLAS detector*, Eur. Phys. J. **C 77**, 40 (2016)

[47] CMS Collaboration, *Measurement of the top pair-production in association with a W or Z boson in pp collisions at 13 TeV*, CMS-PAS-TOP-16-017 (2016)

[48] ATLAS Collaboration, *Search for $t\bar{t}Z$ production in the three lepton final state with 4.7 fb^{-1} of $\sqrt{s} = 7$ TeV pp collisions data collected by the ATLAS detector*, ATLAS-CONF-2012-126 (2012)

[49] ATLAS Collaboration, *Measurement of the $t\bar{t}W$ and $t\bar{t}Z$ production cross sections in pp collisions at $\sqrt{s} = 8$ TeV with the ATLAS detector*, JHEP **172**, 1511 (2015)

[50] CMS Collaboration, *Measurement of associated production of vector bosons and top quark-antiquark pairs at $\sqrt{s} = 7$ TeV*, Phys. Rev. Lett **110**, 172002 (2013)

[51] CMS Collaboration, *Observation of top quark pairs produced in association with a vector boson in pp collisions at $\sqrt{s} = 8$ TeV*, JHEP **096**, 1601 (2016)

[52] U. Baur, M. Buice, L. H. Orr, *Direct measurement of the top quark charge at hadron colliders*, Phys. Rev. **D 64**, 094019 (2001)

[53] S. Schael et al. (SLD Electroweak, DELPHI, ALEPH, SLD, SLD Heavy Flavour Group, OPAL, LEP Electroweak Working Group, L_3), *Precision electroweak measurements on the Z resonance*, Phys. Rept. **257**, 427 (2006)

[54] ATLAS Collaboration, *Luminosity Public Result*, [accessed 21.03.2017] `https://twiki.cern.ch/twiki/bin/view/AtlasPublic/LuminosityPublicResultsRun2`

[55] ATLAS Collaboration, *ATLAS Detector and Physics Performance TDR, Volume I+II*, CERN/LHCC 99-14/15, 1999

[56] ATLAS Collaboration, *ATLAS Experiment - Public Results*, [accessed 03.09.2017] `https://twiki.cern.ch/twiki/bin/view/AtlasPublic/ApprovedPlotsDAQ`

[57] ATLAS Collaboration, *ATLAS level-1 trigger: Technical Design Report*, CERN-LHCC-98-014 (1999)

[58] W. Panduro Vazquez (on behalf of the ATLAS Collaboration), *The ATLAS Data Acquisition System: from Run 1 to Run 2*, Nucl. Part. Phys. **273-275**, 939 (2016)

[59] ATLAS Collaboration, *Muon reconstruction performance in early* $\sqrt{s} = 13$ *TeV data*, ATL-PHYS-PUB-2015-037 (2015)

[60] ATLAS Collaboration, *Performance of Missing Transverse Momentum Reconstruction in Proton-Proton Collisions at 7 TeV with ATLAS*, Eur. Phys. J. **C 72**, 1844 (2012)

[61] M. Cacciari, G. P. Salam, S. G., *The Anti-k(t) jet clustering algorithm*, JHEP **063**, 804 (2008)

[62] ATLAS Collaboration, *Measurement of the* $t\bar{t}Z$ *and* $t\bar{t}W$ *production cross section in multilepton final states using* 3.2 fb^{-1} *of pp collisions at* $\sqrt{s} = 13$ *TeV with the ATlAS detector*, Eur. Phys. J. **C 77**, 40 (2017)

[63] W. Verkerke, D. Kirkby, *The RooFit toolkit for data modeling*, arXiv:physics/0306116 (2003)

[64] A. C. Caldwell, D. Kollár, K. Kröniger, *BAT: The Bayesian Analysis Toolkit*, Comput. Phys. Commun. **180**, 2197 (2009)

[65] F. Sohns, *Studies on physical aspects related to the performance of the Kinematic Likelihood Fitter for the ATLAS collaboration including the development of new transfer functions for the 13 TeV run of the Large Hadron Collider*, Master's thesis, II. Institute of Physics, Georg-August-University of Göttingen (2017), II.Physik-UniGö-MSc-2017/03

[66] ATLAS Collaboration, *Performance of b-Jet Identification in the ATLAS Experiment*, JINST **P04008**, 11 (2016)

[67] K. Zoch, *Reconstruction of $t\bar{t}Z$ Events using Kinematic Likelihood Fits at the ATLAS Detector*, Master's thesis, II. Institute of Physics, Georg-August-University of Göttingen (2016), II.Physik-UniGö-MSc-2016/10

[68] T. Sjöstrand et al., *An Introduction to PYTHIA 8.2*, Comput. Phys. Commun. **191**, 159 (2015)

[69] ATLAS Collaboration, *ATLAS Run 1 Pythia8 tunes*, ATL-PHYS-PUB-2014-023 (2014)

[70] R. D. Ball et al., *Parton distributions with LHC data*, Nucl. Phys. **B 867**, 244 (2013)

[71] T. Gleisberg et al., *Event generation with SHERPA 1.1*, JHEP **2009**, 007 (2009)

[72] H.-L. Lai et al., *New parton distributions for collider physics*, Phys. Rev. **D 82**, 074024 (2010)

[73] D. J. Lange, *The EvtGen particle decay simulation package*, Nucl. Instrum. Math. **A 462**, 152 (2001)

[74] ATLAS Collaboration, *The ATLAS Simulation Infrastructure*, Eur. Phys. J. **C 70**, 823 (2010)

[75] S. Agostinelli et al., *Geant4 - a simulation toolkit*, Nucl. Instrum. Meth. **A 506**, 250 (2003)

[76] K. Pearson, *On the Theory of Contingency and its Relation to Association and Normal Correlation*, Draper's Co. Memoirs, Biometric Series No. **1** (1904)

[77] H. Cramer, *Mathematical methods of statistics*, Princeton University Press (1946)

[78] N. D. Gagunashvili, *Comparison of weighted and unweighted histograms*, arXiv:physics/0605123 (2006)

[79] ATLAS Collaboration, *Measurement of the $t\bar{t}Z$ and $t\bar{t}W$ production cross section in two, three and four lepton final states using 36.1 fb^{-1} of pp collisions at 13 TeV at the LHC*, ALT-COM-PHYS-2016-1730 (2017)

Danksagung

Zunächst möchte ich mich bei Prof. Dr. Arnulf Quadt für die Möglichkeit bedanken, meine Masterarbeit bei ihm verfassen zu können. Das Jahr, welches ich in seiner Arbeitsgruppe verbringen durfte, gab mir einen guten Einblick in das wissenschaftliche Arbeiten und brachte einige besondere Erfahrungen mit sich, die ich nicht missen möchte. Ebenso möchte ich mich bei Prof. Dr. Stan Lai für seine Zustimmung mein Zweitgutachter zu sein bedanken.

Wesentlich für das Voranschreiten meiner Arbeit im ersten halben Jahr waren die Gespräche mit Dr. Boris Lemmer. Seine sympathische Art und die vielen guten Tipps brachen immer wieder neue Inspiration und Motivation in die Arbeit und unterstrichen das gute Arbeitsklima, welches in der Arbeitsgruppe herrscht.

Bedanken möchte ich mich auch sowohl bei Knut Zoch für die technische Unterstützung während meines ersten halben Jahres, die mir sehr bei der Auswertung der Ergebnisse half, also auch bei Nils-Arne Rosien für seine Einführung in die aktuelle Analyse und seine Ratschläge während der zweiten Hälfte meiner Arbeitszeit. Auch die Tipps und Ratschläge von Dr. Elizaveta Shabalina und den anderen Anwesenden während der Meetings waren sehr von Vorteil für meine Arbeit.

Vielen Dank an alle Beteiligten.

Erklärung nach §17(9) der Prüfungsordnung für den Bachelor-Studiengang Physik und den Master-Studiengang Physik an der Universität Göttingen:

Hiermit erkläre ich, dass ich diese Abschlussarbeit selbständig verfasst habe, keine anderen als die angegebenen Quellen und Hilfsmittel benutzt habe und alle Stellen, die wörtlich oder sinngemäß aus veröffentlichten Schriften entnommen wurden, als solche kenntlich gemacht habe.
Darüberhinaus erkläre ich, dass diese Abschlussarbeit nicht, auch nicht auszugsweise, im Rahmen einer nichtbestandenen Prüfung an dieser oder einer anderen Hochschule eingereicht wurde.

Göttingen, den 21. Dezember 2017

(David Grote)